University of Nevada, Reno

Capture and Transport of Laser Accelerated Protons by Pulsed Magnetic Fields: Advancements Toward Laser-Based Proton Therapy

A dissertation submitted in partial fulfillment
of the requirements for the degree of
Doctor of Philosophy in Physics

by

Trevor J. Burris-Mog

Dr. Thomas E. Cowan / Thesis Advisor

and

Dr. Yasuhiko Sentoku / Thesis Advisor

May, 2012

University of Nevada, Reno
Statewide • Worldwide

THE GRADUATE SCHOOL

We recommend that the dissertation
prepared under our supervision by

TREVOR JOHN BURRIS-MOG

entitled

Capture And Transport Of Laser Accelerated Protons By Pulsed Magnetic Fields: Advancements Toward Laser-Based Proton Therapy

be accepted in partial fulfillment of the
requirements for the degree of

DOCTOR OF PHILOSOPHY

Yasuhiko Sentoku, Advisor

Thomas Cowan, Committee Member

Radu Presura, Committee Member

David Bennum, Committee Member

Jeff Mortensen, Graduate School Representative

Marsha H. Read, Ph. D., Associate Dean, Graduate School

May,

Abstract

The interaction of intense laser light ($I > 10^{18}$ W/cm^2) with a thin target foil leads to the Target Normal Sheath Acceleration mechanism (TNSA). TNSA is responsible for the generation of high current, ultra-low emittance proton beams, which may allow for the development of a compact and cost effective proton therapy system for the treatment of cancer. Before this application can be realized, control is needed over the large divergence and the 100% kinetic energy spread that are characteristic of TNSA proton beams.

The work presented here demonstrates control over the divergence and energy spread using strong magnetic fields generated by a pulse power solenoid. The solenoidal field results in a parallel proton beam with a kinetic energy spread of $\Delta E/E = 10\%$. Assuming that next generation lasers will be able to operate at 10 Hz, the 10% spread in the kinetic energy along with the 23% capture efficiency of the solenoid yield enough protons per laser pulse to, for the first time, consider applications in Radiation Oncology.

Current lasers can generate proton beams with kinetic energies up to 67.5 MeV, but for therapy applications, the proton kinetic energy must reach 250 MeV. Since the maximum kinetic energy E_{max} of the proton scales with laser light intensity as

$E_{max} \propto I^{0.5}$, next generation lasers may very well accelerate 250 MeV protons. As the kinetic energy of the protons is increased, the magnetic field strength of the solenoid will need to increase. The scaling of the magnetic field B with the kinetic energy of the protons follows $B \propto E^{1/2}$. Therefor, the field strength of the solenoid presented in this work will need to be increased by a factor of 2.4 in order to accommodate 250 MeV protons. This scaling factor seems reasonable, even with present technology.

This work not only demonstrates control over beam divergence and energy spread, it also allows for us to now perform feasibility studies to further research what a laser-based proton therapy system might look like. A theoretical beam transport system is presented at the end of this dissertation. It shows us that pulse power magnetic optics generating reasonable field strengths can transport a large bandwidth, high kinetic energy proton beam around and into a patient. This gives us insight into the spectrum available per laser pulse at the exit-port of the gantry as well as what types of dose deposition routines and spectral shaping techniques will need to be developed to contour a given dose to a given tumor volume.

Acknowledgements

I have a sincere appreciation for my advisor, Dr. Thomas E. Cowan. He has not only dedicated his life to pushing the boundaries of exploration, but he has bettered my life both professionally and personally. I greatly admire his ability to use the scientific method in all aspect of life. I am also grateful to Mary Lou Cowan for allowing me to frequently intrude into her life to steal her husband's time and for the nearly five years of her fabulous cooking.

I have a very strong appreciation for the PHELIX laser team and the GSI Plasma Physics Group. Pulse power technology has had its challenging moments, and with their help and patients, this project has accomplished a great deal. A special appreciation goes to Vincent Bagnoud, Momme Kreutz, Andreal Tauschwitz and Stefan Göthe.

I am grateful to the faculty and staff of the Department of Physics at the University of Nevada, Reno. My research overseas was somewhat of a special situation, and the support from the department has been fully felt. A special appreciation goes to Dr. Ronald Phaneuf, Dr. Aaron Covington and Dr. Yasuhiko Sentoku.

I want to express greatful appreciation to Dr. Thomas Herrmannsdörfer and Dr. Sergei Zherlitsyn of the Dresden High Magnetic Field Laboratory for their expertise

in pulse power technology and for allowing me to drop in unexpectedly time and time again. Additionally, I have a huge gratitude toward the following people that have also affected me in a positive light: Martin Joost for his dedication, long and late hours working on the pulse power project and skill with pulse power technology; Michael Bussmann for his guidance, support and always keeping life full of humor and jest; and finally, Thomas Kluge for his masterly explanations of laser proton acceleration.

Work accomplished during graduate studies is never done alone. The support and collaborative efforts from all involved in this project is greatly appreciated.

Contents

List of Figures

"When proton therapy facilities become available it will become malpractice not to use them for children."

-Herman Suit, M.D., Ph.D.

Chapter 1

Introduction

This thesis work demonstrates the efficient capture of laser accelerated proton beams and the ability to control their large divergence angles and broad energy range with high-field pulse power solenoids [1]. A coupled system like this brings laser proton acceleration closer to many applications such as novel, compact and cost effective proton therapy systems for the treatment of cancer. Many groups worldwide are studing the feasibility of such a system [2, 3, 4, 5, 6]. The Japan Atomic Energy Agency (JAEA) demonstrated the capture and focusing of laser accelerated protons with Permanent Magnet Quadrupoles (PMQs) [7] and then demonstrated a spot scanning technique with very low energy protons using a prototype laser driven proton medical accelerator beam line coupled to a conventional accelerator [8]. The Radiation Oncology Department of Fox Chase Cancer Center in Philadelphia, United States, have performed Particle In Cell (PIC) simulations for dosimetric studies of Intensity Modulated Radiation Therapy (IMRT) using laser accelerated protons [9] and have generated novel ideas for a light guided beam transport system and energy selector [10]. Promising research towards higher energy protons, collimated laser-driven beams and/or dosi-

metric evaluations is also being performed by the Ecole Polytechnique in Palaiseau, France; the University of Strathclyde in Glasgow, Scotland; The Technische Universitat Munchen in Munich, Germany; the Helmholtz-Zentrum Dresden-Rossendorf in association with OncoRay in Dresden, Germany; Los Alamos National Laboratories in Los Alamos, United States; and others.

The motivation driving this research is large. A 2003 Royal College of Radiologists report shows that 49% of cancer patients are cured by surgery, 40% by radiation therapy and 11% by chemotherapy [11]. Even though surgery results in the highest survival rates, it is only an option if the surgeon has full access to the tumor. Cancers such as chordomas (located in the skull and spine) and optical pathway gliomas (near or around the optical nerves) may be only partially operable and additionally require radiation therapy, or they may be inoperable by a surgeon all together leaving radiation therapy as the only treatment option.

To date, the most common radiation therapy is External Beam Radiation Therapy (EBRT). The history of EBRT is filled with advancements towards perfecting the dose deposition in radiation based treatments, and technology has come a long way since the first radiation therapy treatment using Crooke's tubes in 1896 [12]. Gamma radiation treatments from cobalt and cesium units followed but then gave way to x-rays from linear accelerators. In the last two decades, the LINACS have advanced from conventional radiation therapies to the more precise Stereotactic Radiation Therapies and Intensity Modulated Radiation Therapies (IMRT). Today, the affordable and compact x-ray producing LINACS are the mainstay of Radiation Oncology, in spite of their inferiority to proton therapy (Table 1.1, [13]).

Therapeutic x-ray machines offer an affordable and effective treatment for most can-

cers, but due to the interactive nature of x-rays with matter, the dose is distributed longitudinally through the entire body of the patient. This lack of longitudinal dose control can put sensitive anatomy at risk thus limiting the entrance and exit angles of the therapeutic beam. Figure 1.1 illustrates the dose deposition characteristics of 6 MeV x-rays and 200 MeV protons and shows that the protons are more ideal. Not only do protons provide a rapid distal dose fall-off (behind the tumor), the largest dose is deposited at the tumor site. For X-rays, the dose deposited at the depth where the tumor exists is significantly less than the dose deposited near the skin, and there is no rapid distal fall-off. Both of these X-ray characteristics provide a less than ideal dose contouring ability and can lead to complications that range anywhere from skin burns to nerve destruction (e.g. paralysis, loss of sight) to increased dose and tissue damage in organs at risk.

Proton therapy not only reduces the integrated dose within a patient and reduces the dose delivered to nearby organs at risk but it also lowers the risk of inducing secondary cancers. Ions are an improvement over x-rays, although they too deposit a dose in the healthy tissue, however, as seen in Figures 1.1 and 1.2, they provide a reduced dose deposition in the healthy tissue before the tumor site, a large dose at the tumor site and a rapid distal dose fall-off directly after the tumor site. The distal dose fall-off is a major factor driving ion therapy. The anatomy of the human body is composed of tightly packed organs, nerves and tissues. Irradiating one site within

Costs in Euros	Protons	X-rays
Construction	62,500,000	16,800,000
Operation	15,300,000	6,400,000
Per Treatment	25,600	10,600

Table 1.1: Results from a 2003 cost comparison survey of X-ray and proton Oncology clinics [13]. All values are in Euros.

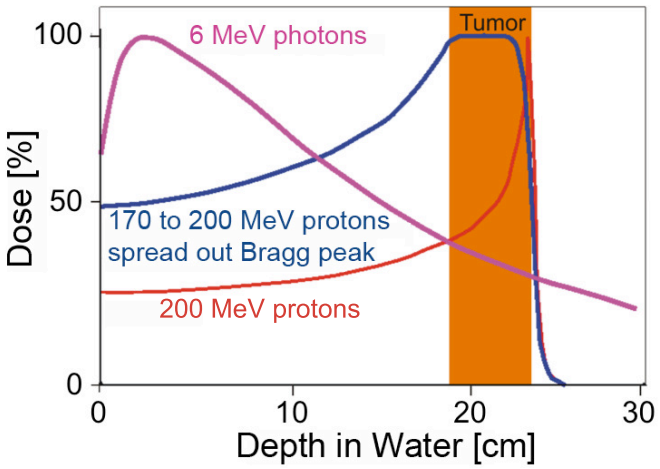

Figure 1.1: Image courtesy of Wikimedia Commons. Comparison of dose deposition in water for 6 MeV x-rays and 200 MeV protons. Protons have a rapid distal fall off and have the highest dose deposition rate at the tumor site, while x-rays have a sluggish distal fall off and have the highest dose deposition rate at shallow depths. Using multiple protons energies, one can generate a spread out bragg peak to deposit a uniform longitudinal dose.

the body will undoubtedly irradiate other sights, but by reducing or eliminating the dose behind the tumor, other anatomies within the body can be spared dose and dose related complications. It should be noted here that, if the dose is low enough, cancer cells can not repair themselves while healthy cells can. For this reason, the resulting damage from the dose deposited in the healthy tissues is mostly repaired, however, the repair process can lead to secondary cancers later in life. This is a major concern for pediatric therapy which is another major driving force behind ion therapy.

Unfortunately, ion (both proton and carbon) therapy facilities operate at high costs and within large real-estate footprints. Proton and ion therapy is presently confined to 38 facilities around the world, and these facilities are generally associated with research institutes as this expensive therapy is still in the experimental phase. Advances in accelerator technology are yielding compact and cost effective proton sources, such as the 3 m diameter, 250 MeV superconducting cyclotron at the Paul Scherrer Institute (PSI) in Switzerland, however the size and cost of the beam transport system

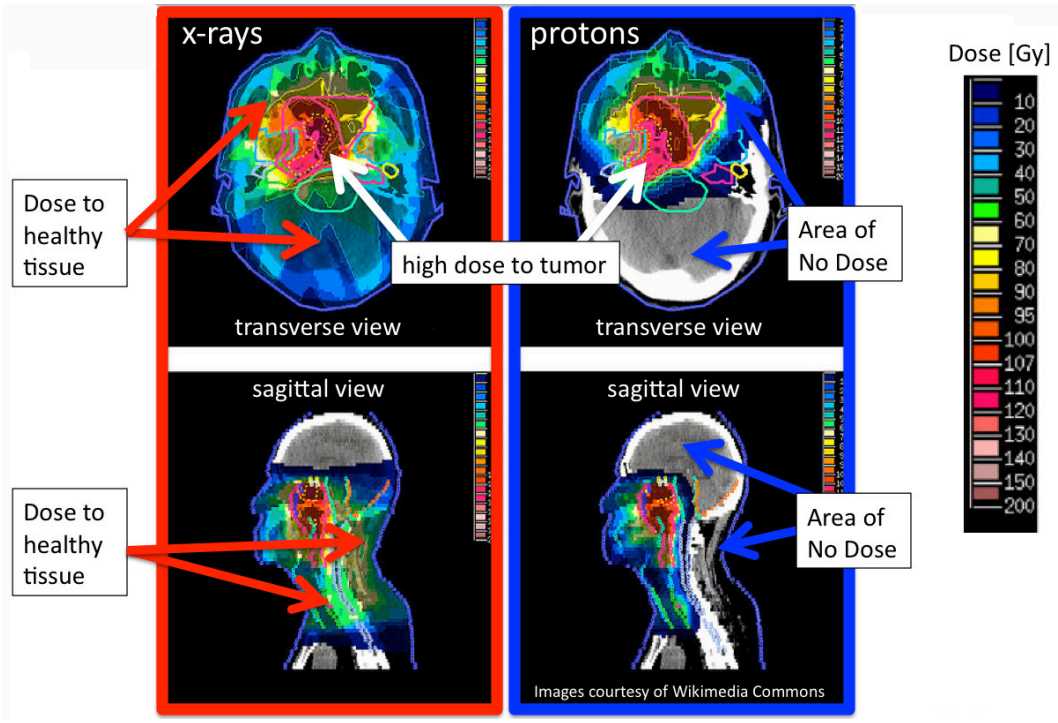

Figure 1.2: Image courtesy of Wikimedia Commons. Dose deposition comparison of IMRT (left) and IMPT (right). Dose sparing to healthy tissue is clearly seen in the proton treatment plan. Additionly, the dose deposited in the healthy tissue by the protons is shown to be lower than that deposited by the x-rays.

(not the accelerator) is the bottleneck limiting the growth of proton therapy. Avoiding sensitive anatomies and/or providing optimal dose contouring is best accomplished when the protons can be delivered at multiple, unconstrained entrance angles. This suggests the need for a rotatable gantry to transport the protons around and into the patient.

To date, gantries rely on large, heavy, resistive (DC) magnets, and a few new designs propose using superconducting magnets as the final bending element in the gantry head. Including magnet elements, beam line components and counterweights, the final weights of these gantries are typically over 100 tons. In order to reduce the size and weight of a gantry, one needs to increase the field strength of the magnets. Resistive magnets, however, are already at their maximum field strengths and superconducting

magnets are limited by the critical field and critical current, i.e. the field and current achievable before the conducting material ceases to be superconducting. Pulse power magnets, however, can be driven by high-energy capacitors, generate an intense short duration magnetic field and is the major component in this thesis work. Their largest restrictions of pulse power are repetition rates, mechanical stresses, Ohmic heating and voltage breakdowns, all of which seem controllable with present day or near future technologies.

To maximize transport efficiency, pulse power magnets should be coupled and synchronized to accelerators that provide high current, short pulse proton beams such as laser accelerators, synchrotrons and Fix Field Alternating Gradient (FFAG) accelerators [14]. The bulk of this thesis work considers laser accelerators[1], because they provide high-yield, short bunch length, ultra-low emittance proton beams that are predicted to scale to higher energies with future generation lasers, Chapter 2. Control of the large divergence angles and 100% energy spread associated with laser accelerated proton beams was demonstrated using a pulse power solenoid. A simulated and theoretical feasibility study that coupled a scaled 250 MeV laser accelerator to a 1.5 m high, pulse power, rotatable gantry was then performed and indicates the need to also develop pulse power dipoles on the order of 8.6 T (25 cm bending radius) and pulse power quadrupoles on the order of 400 T/m (5 cm in length); each of which are within reach with present day technology. It also looks promising that compact, high current conventional accelerators may be appropriate to couple to a pulse power gantry. This too would provide a small scale and flexible configuration for a single accelerator with multi-treatment rooms, while the laser's ability to deliver high-yield,

[1]Laser Accelerator Example - PHELIX laser system, GSI Darmstadt, Germany: 0.4 to 20 ps pulse duration, 120 J energy, 10^{20} W/cm^2 maximum intensity, 1.054 μm wavelength [15]. Present repetition rate is 1 shot per 90 minutes.

short bunch length proton beams via pulsed optics remains promising for research applications such as an injector for high energy physics, generating short lived isotopes, researching nuclear phenomena, for use as a high intensity ion probe, isochorically heating matter and a possible component for use in fast ignition research.

Chapter 2

Laser Accelerated Protons

Over the last decade, there has been extensive research regarding the generation of multi-MeV proton beams from the interaction of intense ($I > 10^{18}$ W/cm^2) short-pulse ($\tau <$ [ps]) laser light with solid micron-thick foils. This laser matter interaction leads to the acceleration mechanism known as Target Normal Sheath Acceleration (TNSA) [16, 17] which produces an electrostatic acceleration field of the order TV/m on the rear-side of the foil, while the foil's contaminant layer of H_2O and hydrocarbons provides the source of protons and other ions [16]. This results in high per-shot proton yields with large energy spreads, large divergences and small transverse- and longitudinal-emittances [18]. Applications in addition to possible compact and cost effective proton therapy [10, 9, 2, 3, 7, 8] may include a laser accelerator injector for high energy physics [19, 18, 7, 20, 21], the generation of short lived isotopes [22], nuclear phenomena [23], a high intensity ion probe [18], isochoric heating [24] and fast ignition [25].

A number of acceleration mechanisms from solid targets have been identified - such

as shock acceleration [26, 27], hole boring [28, 29, 30] and Target Normal Sheath Acceleration (TNSA) [16, 17]. Other acceleration mechanisms have been proposed such as Radiation Pressure Acceleration (RPA) [31, 32, 33, 34] and BreakOut Afterburner (BOA) [35, 36, 37]. TNSA has been the most widely studied, most prevalent and best understood of the acceleration mechanisms and is the principal proton acceleration method used in this work.

Although the present proton energies available from a laser accelerator are less than those available with conventional accelerators, the laser offers a much more compact accelerating system. Using a flat foil target, the 500 fs Nd:Glass PHELIX laser with 100 J on target can routinely accelerate protons to 25 to 35 MeV. The smaller short-pulse systems, like the 30 fs Ti:Sapph DRACO laser with 4 J on target, can routinely accelerate between 10 and 15 MeV protons. Using flat-top cone-shaped targets, the maximum published proton energy is 67.5 MeV [38, 39] using 80 J near 10^{20} W cm^{-2} from the Trident laser system at Los Alamos National Laboratory. Additionally, unpublished results from the same researchers[1] and the same laser system have resulted in 75 MeV protons from mass limited, flat foil targets.

2.1 Laser-Matter Interaction

Laser proton acceleration via the TNSA mechanism begins with the generation of a hot dense plasma on the front surface of the micron-thick foil target. As the laser propagates through the target to a depth of $\delta = c/\omega_{pe}$, its energy is absorbed and reduced to a factor of $1/e = 1/(2.718...)$. Here, δ is known as the skin depth, $\omega_{pe} = \sqrt{n_e e^2/m_e \varepsilon_0}$ is the electron plasma frequency, where n_e is the electron density, e

[1] including Marius Schollmeier from Sandia National Laboratory, New Mexico

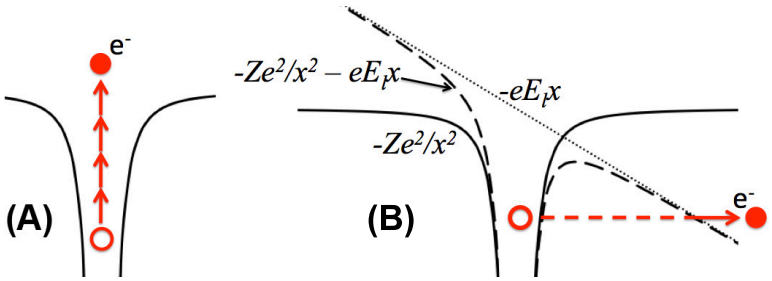

Figure 2.1: **(A)** Multi-Photon Ionization: The absorption of multiple photons will have a cumulative effect and transfer enough energy to the electron for it to escape the potential well. **(B)** Electron Tunneling: The external time varying electric potential from the laser field (dotted line) and the binding potential of the atom (solid line), together, deform the binding potential allowing for the possibility of an electron to tunnel and escape.

is the charge of an electron, m_e is the mass of an electron and ε_0 is the vacuum perittivity. The prevailing ionization mechanisms are tunneling and multi-photon ionization. Multi-photon ionization begins at laser intensities near 10^{11} W/cm^2, and tunneling ionization has a probability of occurring that is dependent on the frequency ω of the laser light, the ionization potential E_{ion} and the laser light's electric field strength. Both can occur even when $E_{ion} >> \hbar\omega$. In the tunneling case, the superposition of the external electric field E_l can lower the barrier long enough for tunneling ionization to occur [40]. This timeframe can be estimated from $\tau_{tunnel} \approx \sqrt{2mE_{ion}/e^2E_l^2}$, and the potential well follows the form $V(x) = -Ze^2/x^2 - eE_lx$ seen in Figure 2.1. Here e is the electron's charge.

The ionization on the front side of the target leads to a free electron population that the laser's electromagnetic plane waves can now accelerate. The forces exerted on the electrons by the electric and magnetic fields follow the Lorentz equation $\mathbf{F} = e\mathbf{E} + e\mathbf{v} \times \mathbf{B}$, which lead to momentum gains that are both perpendicular ($e\mathbf{E}$) and parallel ($e\mathbf{v} \times \mathbf{B}$) to the direction of laser propagation.

A brief look at the perpendicular motion in linearly polarized laser light shows that

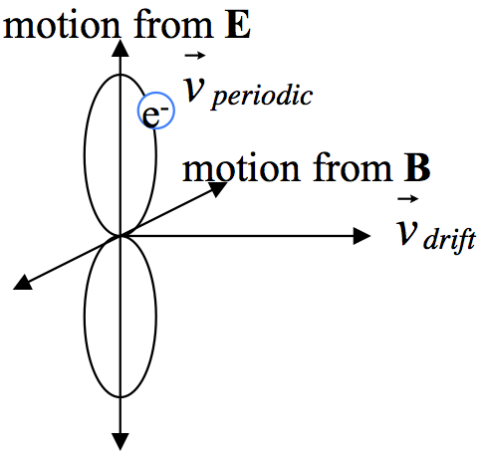

Figure 2.2: Figure 8 motion of a free electron in an electromagnetic plane wave from the point of view of the average rest frame. There exists both a periodic velocity and a drift velocity.

the electric field $\mathbf{E} = \mathbf{E}_0 sin(\omega t)$ leads to a periodic force

$$\mathbf{F}_\perp = e\mathbf{E}_0 \sin(\omega t) \tag{2.1}$$

and a periodic electron velocity $\mathbf{v}_{periodic} = \frac{-e\mathbf{E}_0}{m\omega}\cos(\omega t)$. The parallel momentum gain found by looking at the time average of $\mathbf{v}_{periodic}$, which as illustrated in Appendix 8.2, shows that there exists a force parallel to the laser's propagation direction and equal to,

$$\mathbf{F}_\parallel = \frac{-e^2}{4m\omega^2} \bigtriangledown \mathbf{E}_0^2 \ , = -mc^2 \bigtriangledown \gamma_{os} \tag{2.2}$$

Here, $\gamma_{os} = \sqrt{1 + < a_0^2 >}$ and $< a_0 > = < eE/mc\omega >$ is the time averaged normalized electric field of the laser, and $\mathbf{F}_\parallel$ is the ponderomotive force of the laser light. The perpendicular and parallel forces result in an electron trajectory that follows a figure-8 path[2] in the co-moving frame with a forward component, Figure 2.2.

The relativistic electrons move through the micron-thick target within a 5° to 15° divergence half-angle, possess a density near critical density[3] $n_{cr} = 10^{21}$ cm^{-3} for a

[2]A detailed derivation of the figure-8 motion can be found in Chapter 3 of Reference [41].

[3]The critical density is the density at which a plasma becomes opaque to an electromagnetic wave and is defined as $n_{cr} = m\omega^2/4\pi e^2$, where ω is the frequency of the laser light.

micron wavelength laser light and have temperatures $T_e = T_{hot}$ near the ponderomotive potential of the laser light [42, 43, 44, 45, 17]. An estimate[4] of the energy that an electron gains from the laser is given by $T_{hot} \approx m_e c^2(\sqrt{1 + \frac{I\lambda^2}{1.37\times10^{18}}} - 1)$ [46], e.g. $I = 1 \times 10^{20}$ W/cm^2 and $\lambda = 1.057$ μm gives $T_{hot} \approx 4.1$ MeV.

Some of the early accelerated electrons leave the target, while the electric charge separation causes the later electrons to return to the target. As the hot electrons turn back to the target, they form a cloud extending into vacuum by several Debye lengths, $\lambda_D = \sqrt{\frac{\epsilon_0 k_B T_e}{e^2 n_e}} \approx 7438 \times \sqrt{\frac{k_B T_e[eV]}{n_e[m^{-3}]}}$, where k_B is Boltzmann's constant, T_e is the electron temperature and n_e is the electron density. The process is illustrated in Figure 2.3. This hot electron cloud forms intense longitudinal electrostatic sheaths of

[4]The value T_{hot} is the energy of the electrons oscillating in the transverse electric field of the laser light and does not account for any longitudinal motion.

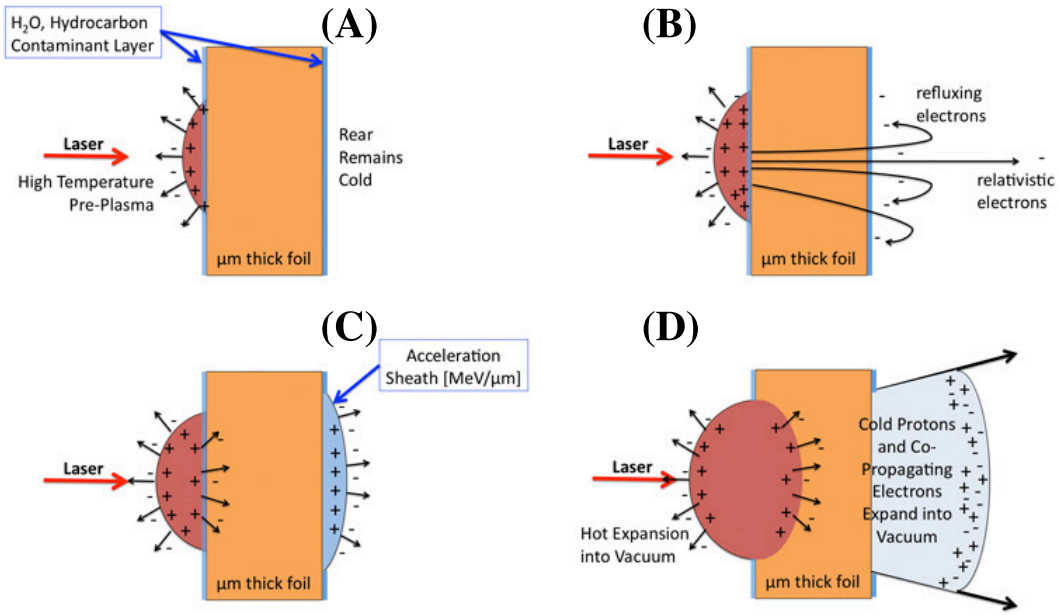

Figure 2.3: The TNSA Process: (**A**) The incident laser ionizes and heats the front of the target. (**B**) Electrons are accelerated in the laser forward direction to relativistic energies. A small portion (of order a nC) leave the target while the rest return to form (**C**) the [TV/m] accelerating sheath. (**D**) The protons from the rear layer of water and hydrocarbon contaminant expand into vacuum along with the co-propagating electrons.

the order $E_{sheath} \approx k_B T_e / e\lambda_D \approx$ TV/m with a Gaussian profile at the vacuum-solid interface. This field is responsible for field-ionization and acceleration of the water and hydrocarbon surface contaminants. Therefore, the kinetic energy of the ions is directly related to T_{hot} as will be discussed in section 2.2.

2.2 Plasma Expansion

Using a self-similar expansion model [42, 44], information about the structure of the ion front, the ion energy spectrum and the maximum achievable ion energies can be approximated. The 1-dimensional expansion model assumes quasi-neutrality and that the electron density n_e follows a Boltzmann relation,

$$n_e = n_{e0} \exp(-e\Phi / k_B T_e) \tag{2.3}$$

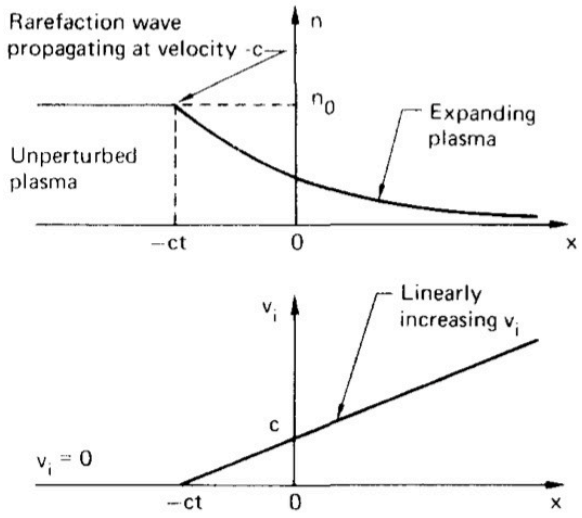

Figure 2.4: Image from Reference [42] of the density and velocity profiles from the self similar solutions. The expansion extends into vacuum while the rarefaction wave propagates into the unperturbed plasma with velocity c_s.

where n_{e0} is the unperturbed electron density and Φ is the electrostatic potential. The ions follow the continuity equation,

$$\frac{\partial n_i}{\partial t} + v_i \frac{\partial n_i}{\partial x} = -n_i \frac{\partial v_i}{\partial x} \tag{2.4}$$

and the equation of motion,

$$\frac{\partial v_i}{\partial t} + v_i \frac{\partial v_i}{\partial x} = \frac{-Ze}{m_i} \frac{\partial \Phi}{\partial x} \ . \tag{2.5}$$

Self-similar solutions for Equations 2.4 and 2.5 lead to a density of $n_e = Zn_i = n_{e0}\exp(-x/c_s t - 1)$, a velocity of $v_i = c_s + x/t$ and an electric field of,

$$E_{ss} = \frac{k_B T_e}{e c_s t} = E_0/\omega_{pi} t \ , \tag{2.6}$$

where $e = 2.71828...$, $\omega_{pi} = \sqrt{n_{e0} Z e^2/m_i \epsilon_0}$ is the plasma frequency, $E_0 = \sqrt{n_{e0} k_B T_e/\epsilon_0}$ and $c_s = \sqrt{Z k_B T_e/m_i}$ is the velocity of the rarefaction wave that propagates into the plasma. Figure 2.4 from Reference [42] illustrates the density and velocity profiles of the expanding plasma. In this model, an ions velocity begins from zero at the rarefaction wave and increases linearly with x. Although the linear increase predicts ions with infinite velocities as x approaches infinity, their densities fall exponentially to zero ensuring a finite velocity for all ions. The ions located at $x = 0$ at time t_0, therefore, approach $v_i = c \cdot ln(t/t_0) + v_{i0}$.

Simulation results from Reference [47] are based on this self-similar expansion model and give a nice illustration of the charge separation and electric field within the plasma expansion. As seen in the left image of Figure 2.5, there are three distinct areas of charge. There exists a positive charge of σ at $x = -c_s t$ which is where the rarefaction

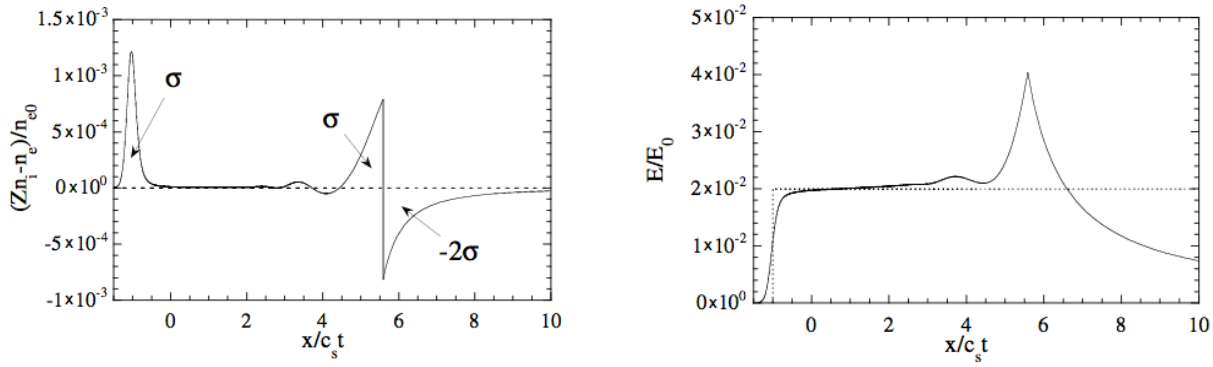

Figure 2.5: Simulation results from Reference [47]: **Left** Charge separation within the flat foil target at time $\omega_{pi}t = 50$. The ion front rests at $x/c_st \approxeq 5.59$. **Right** The electric field corresponding to the space charge in the left image. The dotted line is Equation 2.6.

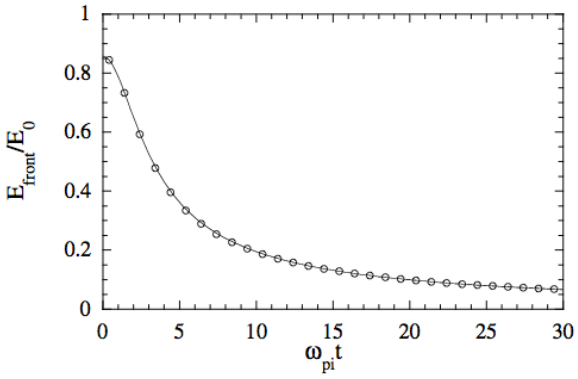

Figure 2.6: The electric field at the ion front as a function of time from Reference [47]. The numerical results are plotted with circles and Equation 2.7 is plotted with a solid line.

wave stands, a positive charge of σ behind the ion front which stands at $x/c_st \approxeq 5.59$ and a negative charge of 2σ which represents the electron cloud in front of the ion front. The total charge around the ion front is then $-\sigma$, which is responsible for generating the electric fields presented in the right image of Figure 2.5. Evolution of the field follows,

$$E_{front} \approxeq \frac{2E_0}{\sqrt{2 \times 2.71828 + \omega_{pi}^2 t^2}} \tag{2.7}$$

and is presented in Figure 2.6. The force $m_i dv/dt = ZeE_{front}$ can be integrated to find the velocity of the ion front, which then follows,

$$v_{front} \approxeq 2c_s ln(\tau + \sqrt{\tau^2 + 1}) \ , \tag{2.8}$$

where $\tau = \omega_{pi}t/\sqrt{2e}$ is the normalized acceleration time. The maximum velocity and energy is obtainable by taking the limit $\omega_{pi}t >> 1$:

$$v_{max} \approx 2c_s ln(2\tau) \tag{2.9}$$

$$E_{max} \approx \frac{1}{2} m_i v_{max}^2 = 2Zk_B T_e [ln(2\tau)]^2 \ . \tag{2.10}$$

The self-similar model predicts the energy spectrum of the ions yielding the number of ions per unit energy as

$$\frac{dN}{d\varepsilon} = n_{i0} c_s t / \sqrt{2\varepsilon Z k_B T_e} \ \exp(-\sqrt{2\varepsilon / Z k_B T_e}) \tag{2.11}$$

Here, n_{i0} is the ion density in the unperturbed plasma, i.e. the solid state density which is typically $\approx 10^{23}$ cm^{-3}. One can see that the slope of the exponential decay is dependent on the relativistic electron temperature. This allows an approximation of T_e to be extracted from a measured spectrum, e.g. $T_e = 0.4$ MeV from the spectrum in Figure 2.9.

2.3 Proton Beam Characteristics

The spatial and energetic characteristics of laser accelerated proton beams are diagnosed using RadioChromic dosimetric film[5]. This film responds optically to dose deposited within its active layer, and its response is sensitive to the high energy loss rates exhibited by protons as they pass through the active layer. Since the co-propagating electrons have a much lower energy loss rate, information about the protons can be

[5]International Specialty Products, www.ispcorp.com

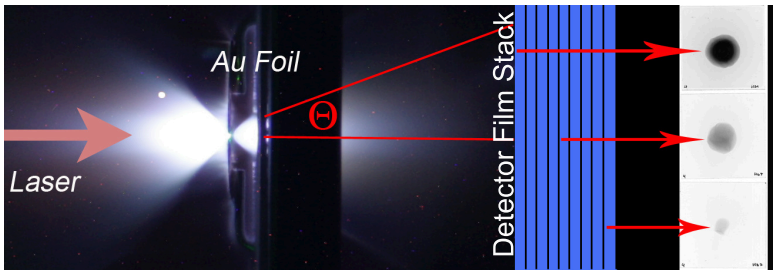

Figure 2.7: Illustration of data collection for laser accelerated protons using dosimetric film stacks. The laser is incident from the left. The protons are accelerated to the right within an energy dependent divergence angle and expose the dosimetric film stack. An exposed film stack is presented in Figure 2.8.

measured without significant influence from their co-propagating electrons. Layers of film are stacked together and placed behind the target, Figure 2.7, and the protons loose energy as they pass through the film layers. Because the protons deposit the largest dose where they stop, as described by Equation 8.1 in Appendix 8.1, each film layer corresponds to a Bragg peak energy. Figure 2.8 shows nine dosimetric film layers that were stacked and placed 32 mm behind a 24 μm Au foil target. The protons were accelerated with the PHELIX laser system and reached a maximum energy of 23.3 MeV. The film shows the energy dependent divergences, and the optical density illustrates the exponentially decaying spectrum as predicted from Equation 2.11.

Using RadioChromic Film Imaging Spectroscopy (RIS) [48], the optical density of the film is converted to proton numbers per unit energy. Figure 2.9 illustrates the energy spectrum and divergence angles as extracted from the film layers in Figure 2.8. An integration over the spectrum indicates that 2×10^{12} protons between 3.7 and 23.3 MeV were accelerated. The protons are contained within a relatively uniform angular distribution with up to a half-angle divergence of 7° for high energy protons and 20° for low energy protons. The largest divergences originate from areas where

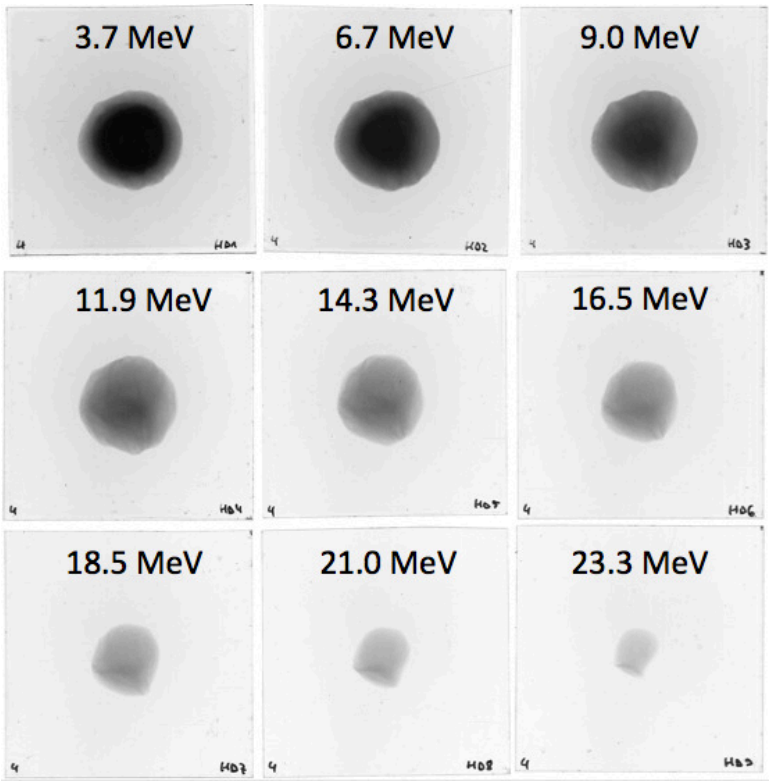

Figure 2.8: Direct measurement of laser accelerated protons from a single PHELIX laser pulse. The low energy protons deposit a larger dose and have a larger beam profile than the higher energy protons. The film stack was positioned 32 mm after the 24 μm Au foil target.

the gradient of the electrostatic sheath is strongest [49].

The energy gained by a proton is, in part, dictated by where the proton is located within the electrostatic sheath. The electrostatic sheath has a Gaussian shape, and the maximum electric field strength is located at the center of the sheath. This means that the maximum energy that a given proton can reach is dictated by its radial position within the sheath. A proton's energy is also influenced by a partial screening of the electric field. The protons within the contaminant layer or those with a slow acceleration start interact with an electric field that is partially screened by the protons that are well under way in the acceleration process.

Proposals and/or experiments to control the divergence of laser accelerated protons

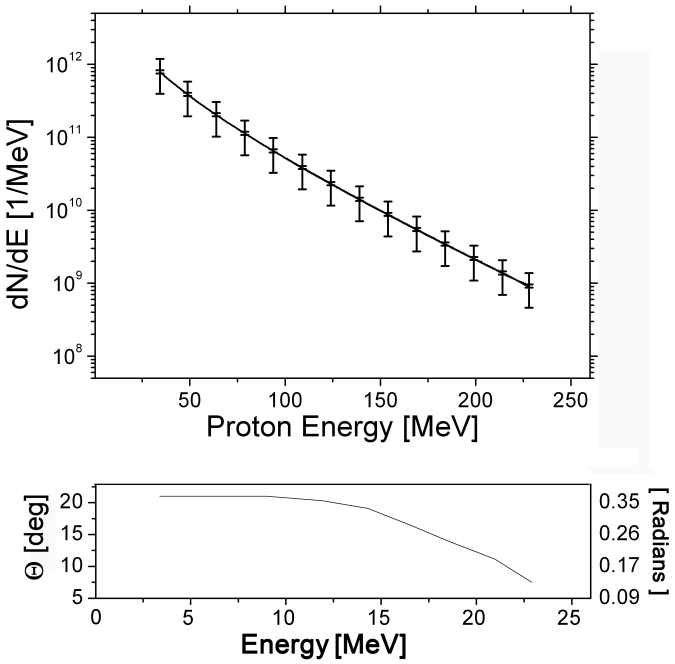

Figure 2.9: **Top:** Processed results of the data presented in Figure 2.8, including 5% RIS error bars and 50% shot-to-shot error bars. The exponential reduction of dN/dE for increased energies is one characteristic trait of laser accelerated protons. **Bottom:** Maximum beam divergence as a function of proton energy. The large beam divergences for low energy protons and the moderate beam divergences for the high energy protons is another characteristic trait of laser proton acceleration.

include attempts to shape the electrostatic sheath via novel target designs such as hemispheres and trumpets [24, 50, 51], attempts to shape the electrostatic sheath with an annular laser beam [52], and attempts to capture and collimate[6] proton beams using ion optics such as a laser-triggered plasma lens [53, 54], permanent magnet quadrupole PMQ [55, 7, 56] or a pulse power solenoid [57, 58, 1]. To date, the most effective focusing of laser accelerated protons is accomplished with magnetic fields.

[6]Collimate in this writing means to transform the diverging protons into a parallel proton beam as opposed to using an aperture to keep the parallel protons and remove the diverging protons.

2.4 Alternative Acceleration Methods

There are two main regimes of laser proton acceleration; the TNSA regime and the transparency regime. The latter occurs in ultra-thin targets where the target thickness is at or below skin-depth of the laser light, i.e. the target thickness is at or below the penetration depth of the laser. In the transparency regime, the laser-matter interaction begins as an enhanced TNSA. The enhancement comes from a strong volumetric heating as a result of the laser penetrating a larger portion of the target volume. Experiments systematically reducing the target foil thickness (down to 10 nm) while using high contrast laser beams demonstrate this enhanced volumetric heating [59, 60, 61].

Just as in TNSA, the relativistic electrons generate accelerating electrostatic sheaths, but in the transparency regime, the electrons continue to gain energy from the laser light. Particle-in-Cell simulations using PICLS [62] show that the electrons continue to gain energy from the laser via large amplitude plasma waves. This occurs when the laser pulse length is near that of the plasma wavelength, $\lambda_p = 2\pi c/\omega_p$. The electrons continue to transfer their energy to the protons during this process, and the electron temperature reaches a constant as the energy absorbed by the laser becomes equal to the energy transferred to the protons. In essence, the electrons are continuously pushed by the laser while pulling the protons along. For the acceleration method termed Break-Out Afterburner (BOA) [35, 36, 37], it is suggested that the coupling of electron energy to ion energy occurs via Buneman instabilities [63].

Alternatively, it is proposed [31, 32, 33, 34] that thin foils be irradiated with circularly polarized laser light. The advantage of this Radiation Pressure Acceleration (RPA) is seen in its scaling characteristics. The maximum proton energy scales proportionally

with laser intensity ($E_{max} \propto I_L$), which is an exponent of two greater than the scaling characteristics of TNSA. The circular polarization eliminates the oscillating component in the $\mathbf{v} \times \mathbf{B}$ force. This greatly reduces the electron heating and allows the electrons to be compressed into a high density layer near the front of the laser pulse. The electric field then generates a restoring force that then accelerates the ions. If one can properly balance the target thickness, target density and laser intensity so the radiation pressure equals the restoring force, then the electrons and ions should continue to gain energy from the laser and propagate ballistically as a quasi-neutral bunch. The early claims of RPA, however, have not yet been reproduced.

Chapter 3

Ion Optics for Beam Capture

A requirement of proton therapy is to deposit 2 Gy dose over a 1 liter volume, which requires on the order of 10^{12} protons in total. Common treatment times of a few minutes or less then generate the need to deliver on the order of 10^{10} protons per second. Although lasers can accelerate up to 10^{13} protons per laser pulse, a large number of protons will fall outside of the desired energy range. Additionally, without correction, the large beam divergences limit the number of protons that can be directed into the patient.

Since the divergence is determined by the electrostatic sheath and the shape of the target, it may be that novel target geometries can provide control over the divergence. Presently, the most effective control has been accomplished with ion optics that are positioned after the target. Ion optics have the extra benefit of decoupling the acceleration mechanism from the divergence control, and a number of focusing elements are available. The successful demonstration of capture and collimation of laser accelerated protons has been accomplished using three different techniques: laser triggered

plasma lenses, permanent magnet quadrupoles, and pulse power solenoids. To date, the pulse power solenoid has the most efficient capture efficiencies, as demonstrated by me in this thesis work.

3.1 Direct Current Magnets

3.1.1 Resistive Magnets

Since quadrupoles and solenoids are the two most common and most effective magnets used for focusing charged particles, it is important to understand their strengths and weaknesses. These two types of resistive focusing magnets are capable of generating magnetic fields of a few Tesla, operate in either AC or DC mode, offer temporally long magnetic fields relative to the bunch length of the laser accelerated proton beam and, in DC mode, benefit from magnetic field shaping via iron cores.

Viewing the focal lengths f of a quadrupole[1] and a solenoid in the thin lens approximation shows that the magnitude of the magnetic field B, in each case, scales with the momentum p of the proton.

$$f_{quad} = \frac{r}{l}\frac{p}{qB} \tag{3.1}$$

$$f_{sol} = \frac{4}{l}\frac{p^2}{q^2B^2} \tag{3.2}$$

Here, q is the particle charge, l is the length of the lens and B/r is the quadrupole's

[1]Quadrupoles are usually characterized by the gradient of their magnetic field. Reducing the quadrupole bore for a given field strength results in larger gradients and larger focusing. Here, we are concerned with the magnetic fields, and not the gradients, to form a direct comparison with the focusing power of a solenoid.

magnetic field gradient where r is the radius of the quadrupole. At first glance, one may see the two lenses as comparable. Because the quadrupole focuses in one transverse plane and defocuses in the other, two quadrupoles separated by a length L and rotated by 90° with respect to one another are needed to form a doublet which is capable of focusing in both planes. The doublet has the final focal length of $1/f_{doublet} = L/f_{quad}^2$, so the net focusing power is proportional to the square of the magnetic field [64]. Therefore, both f_{quad} and f_{sol} are proportional to $p^2/(q^2B^2)$. The drawback of quadrupoles, however, is that this formulation is based on paraxial particle trajectories. Considering TNSA protons, the defocusing of the first quadrupole in a doublet configuration adds significantly to the already large divergence. This results in significant beam clipping by the aperture of the second quadrupole.

On the other hand, the solenoid lens is only capable of focusing. As charges enter the radialmagnetic fields B_r of a solenoid, the Lorentz force causes an azimuthal acceleration. The resulting azimuthal velocity v_ϕ leads to an inward radial force when it interacts with the longitudinal magnetic field B_z within the bore. Compared to quadrupoles, a solenoid lens can accommodate larger acceptance angles and larger transport efficiencies. The magnetic field strength B needed when scaling to higher proton energies (or higher momentums p) scales simply as $I \propto B \propto p$, where I is the current driving the solenoid field. The solenoid, therefore, is the more appropriate ion optic for this application.

Although resistive solenoid magnets offer us the ability to collimate laser accelerated protons of a few MeV, they are limited by their DC power supply and resistive (Ohmic) heating. This means that they are not scalable to the energies required to perform proton therapy.

3.1.2 Superconducting Magnets

Superconducting magnets offer an additional increase in magnetic field strength compared to resistive magnets. A conductive wire's resistance can reach zero by cooling the material to below its critical temperature. Considering that the cryogenic system uses liquid helium, this technology is expensive. It also has physical limitations. The number of electrons in the superconducting band is not only affected by the temperature of the conductor but also by the interaction with magnetic fields. The rate of change in the field can lead to eddy currents and a localized increase in temperature, while strong magnetic fields can change the phase of the conductive material and lead to a reduction in the superconducting electron population. When the field changes too rapidly or it is too strong, the magnet will suffer from magnetic quenching resulting in a return to the resistive state. Additionally, defects in the conductive material can lead to localized resistance resulting in rapid boil-off of the cryogenic bath and a large scale Ohmic heating, i.e. a loss of superconductivity.

Although superconducting magnets offer an increase in the magnetic field strength when compared to resistive magnets, this magnetic quenching limits the scalability of the technology. In the future, superconducting magnets in combination with novel targets that reduce the proton beam divergence may, together, offer a reasonable solution for the capture and transport of laser accelerated protons.

3.2 Pulse Power Solenoid

Pulse power solenoids are also a form of resistive magnets. They have air cores instead of the usual iron or μ-metal[2] cores found in resistive DC solenoids. Pulse power magnets achieve the largest magnetic field strengths compared to any other magnet. They are powered by applying a temporally short, high voltage pulse from the pulser[3] across the conductive wire, allowing one to drive strong fields without generating strong Ohmic heating.

The decision to use a solenoid came from its high capture efficiencies but also its azimuthally symmetric magnetic field. The azimuthally symmetric field results in a more uniform collimated beam compared to that of a quadrupole. This can only benefit spectral shaping and dose deposition routines when and if the times comes. Additionally, pulse power solenoids are well understood and routinely used to generate high magnetic fields such as the few millisecond $>$ 90 T fields produced by the High Field Labs at the Helmholtz-Zentrum Dresden-Rossendorf (HZDR) [65] and Los Alamos National Laboratory (LANL) [66]. Single turn pulse power current loops have routinely generated $>$ 300 T at LANL over a time period on the order of nanoseconds [67], although these current loops have a lifespan of at most a few shots. The solenoids used in this thesis work generate up to 16 T, and this present design will need to generate 38.4 T in order to collimate 250 MeV protons. With the exclusion of voltage breakdown (Section 3.2.7), the 16 T field is only limited by the maximum

[2]This is due to two reasons. The first is that μ-metal saturates near 1 T and pulsed solenoids are being designed to generate fields far greater in strength than this. Therefore field shaping will require another technique. Second, as will be discussed in Section 3.2.5, the changing field within a solenoid leads to induced currents and large forces within conductors, and μ-metal ($\approx$77% nickel, $\approx$16% iron and $\approx$5% Cu) is slightly conductive.

[3]A pulser consists of a single capacitor or a bank of capacitors and is responsible for driving the current inside the solenoid. The two pulsers used in this work could deliver 32 kJ and 50 kJ per pulse at a maximum voltage of 16 kV. A detailed discussion is presented in Section 3.2.4.

voltage of the capacitor, and it is reasonable to assume that this design can achieve at least slightly higher field strengths before structural integrity is compromised.

3.2.1 Scaling of the Magnetic Field

The first step in this thesis work was to determine the appropriate ion optic for laser accelerated proton therapy. This means that the chosen design must collimate protons and must be scalable to accommodate 250 MeV protons. As presented in Section 3.3, many groups have demonstrated collimation at modest proton energies, e.g. $\leq$ 10 MeV, with permanent magnet quadrupoles and laser driven plasma lenses. The permanent magnet quadrupoles are not scalable, and the scalability of the plasma lens has yet to be demonstrates. Pulse power ion lenses, however, are a technology capable of having their magnetic field scaled. The focal power[4] of the solenoid follows,

$$\frac{1}{f} = (\frac{q}{2m_0\gamma\beta c})^2 \int_{-\infty}^{\infty} B_z^2 dz \tag{3.3}$$

where $m_0\gamma\beta c$ is the momentum of the particle and accounts for relativistic effects by including the Lorentz factor γ, and $\beta = v/c$. Therefore, $1/f \propto B^2/p^2$ and B must scale with $p \approx \sqrt{E}$ for a fixed geometry. The first generation solenoids presented in this work demonstrated a collimation of 13.75 MeV protons for an 8.5 T field. This scaling suggests that the maximum tested field of the solenoid, 16 T, will collimate, i.e. make parallel to the longitudinal axis, 48 MeV and that 38.4 T will collimate 250 MeV protons. Please see Appendix 8.3 for a comparison of a short solenoid to a long solenoid.

[4]The focal power is defined as the inverse of the focal length f.

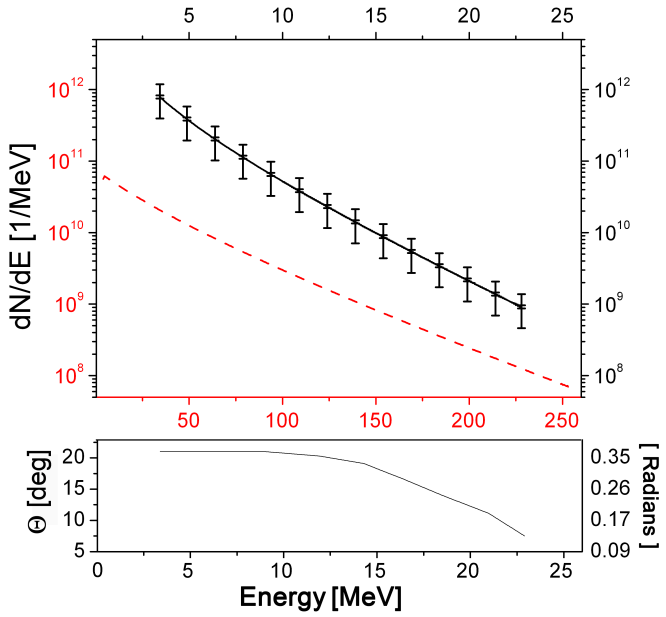

Figure 3.1: Processed results of the data presented in Figure 2.8 (black solid curve, top and right axes, includes 5% RIS error bars and 50% shot-to-shot error bars) along with a scaled (predicted) TNSA spectrum with maximum energy of 250 MeV (red dashed curve, botton and left axes). The total number of protons in both cases is 10^{13}.

3.2.2 Proton Beam Capture for Cancer Therapy

Chapter 2 suggests that the maximum proton energies will reach 250 MeV as laser technology advances and that the shape of the spectrum will likely remain an exponential decay following $dN/d\varepsilon = n_{i0}c_s t\sqrt{2\varepsilon\varepsilon_0}exp(-\sqrt{2\varepsilon/\varepsilon_0})$, where N is the number of protons and ε is the kinetic energy. To be conservative, one can assume that the angular divergences will remain and that the total number of accelerated protons will not exceed the presently achievable 10^{13} per laser pulse. This suggests that a 250 MeV spectrum will possess characteristics similar to spectra measured today. The 250 MeV spectrum shown in Figure 3.1 was generated by stretching the spectrum presented in Figure 2.9 from 23 MeV to 250 MeV and normalizing $dN/d\varepsilon$ such that the total number of protons remains the same, $N = 1.85 \times 10^{12}$. The new slope gives

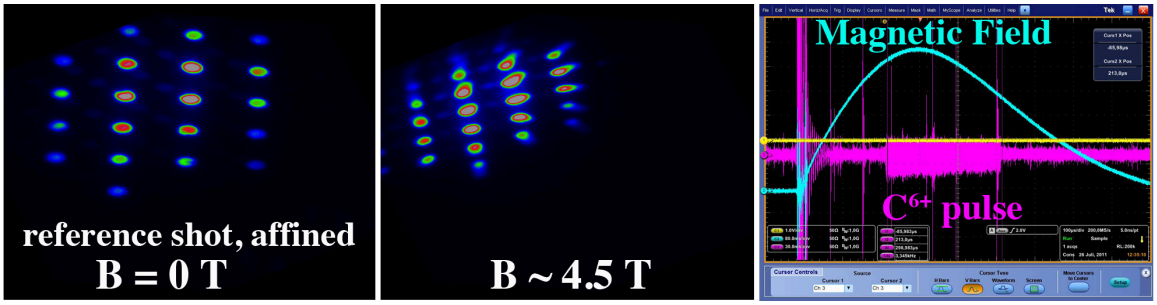

Figure 3.2: Example of induced rotation and focusing of 11.4 MeV/u C^{6+} ions traveling through the solenoid's magnetic field. An affine transformation was applied to both scintillator images. The beamlets were created with a pepper-pot placed before the solenoid. The magnetic field rise-time was 330 μs (blue curve, at right) and the C-beam pulse length was 300 μs (magenta measurement, at right), resulting in a blurring of the time-integrated image at center.

a $T_e = 7$ MeV. Since $\epsilon_{max} \propto T_e \propto \phi_{pond}(I^{0.5})$, this suggests[5] that the required laser intensity is at least on the order of 10^{21} W/cm^2.

Although the total number of protons seems large, only a small energy range will have the appropriate Bragg peak ranges to deposit a dose to the tumor site. In addition, the number of protons per MeV reduces as the maximum energy of the spectrum is increase. To keep the treatment times to a few minutes or less, the proton numbers within the useful energy range for therapy applications must be maintained, consistent with a useable or achievable laser repetition rate. This requires a lens with high capture efficiency.

3.2.3 Particle Motion in the Field of a Solenoid

A charged particle's motion in a solenoidal field is directly determined by the Lorentz force $\mathbf{F} = q\mathbf{v}\times\mathbf{B}$, where $\mathbf{B}$ has only radial and longitudinal components. The ini-

[5] Assuming $T_e \propto I_L^{0.5}$ from Chapter 2 leads to $\frac{T_{e,1}}{T_{e,2}} = \frac{I_{L,1}^{0.5}}{I_{L,2}^{0.5}} \rightarrow I_{L,2} = [\frac{7.0MeV}{0.4MeV}\sqrt{2.9\times10^{19}W/cm^2}]^2 \approx 9\times10^{21}$. Assuming that $T_e \propto I_L^{0.7}$ because of relativistic effects [[68]], $I_{L,2} \approx 1.8\times10^{21}$.

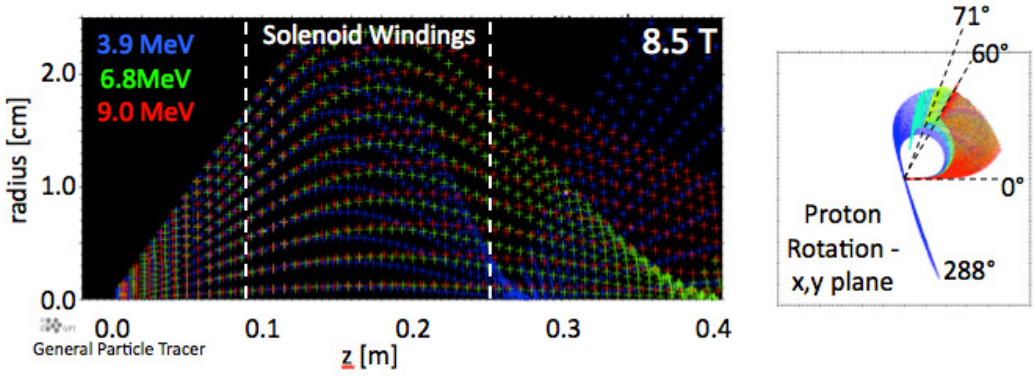

Figure 3.3: **Left** Sagittal view of particle tracking through an 8.5 T magnetic field for 3.9, 6.8 and 9.0 MeV protons. The focal lengths follow Equation 3.3. **Right** Transverse view of the total rotation through the solenoid's 8.5 T field shown in the left image. The rotation follows Busch's Theorem [69]

tial interaction of the charge's velocity v_z with the radial magnetic field B_r at the entrance of the solenoid leads to an azimuthal force F_ϕ, and the beam of charges begins to rotate. The azimuthal velocity v_ϕ gained at the entrance interacts with the longitudinal field B_z inside the bore resulting in an inward force. This focusing effect is independent[6] of the sign of the magnetic field, so the solenoid always forces the particles towards its axis. Upon exiting the solenoid, the particles again interact with the radial magnetic field. The sign of the field is now opposite what it was at the entrance, resulting in an azimuthal deceleration of the particle

An example of trajectory changes do to the solenoid field are shown in Figure 3.2. Here, a collimated beam of 11.4 MeV/u carbon ions from the GSI Universal Linear Accelerator (UNILAC) were pass through the solenoid field. The beam's pulse length was 300 μs, and it was directed on to a scintillating screen[7]. A CCD camera captured time-integrated images of the scintillated light. The solenoid's magnetic field rise time was 330μs. The CCD images illustrate a narrowing of the ion beam waste due

[6]Completing the cross product in the Lorentz equation gives $F_\phi = qv_zB_r$ and $F_r = qv_\phi B_z$. The only two combinations of B_r and B_z are $(-B_r, B_z)$ and $(B_r, -B_z)$ which always result in F_r being radially inward.

[7]EJ-212 plastic scintillator, ELJEN Technology, Texas USA

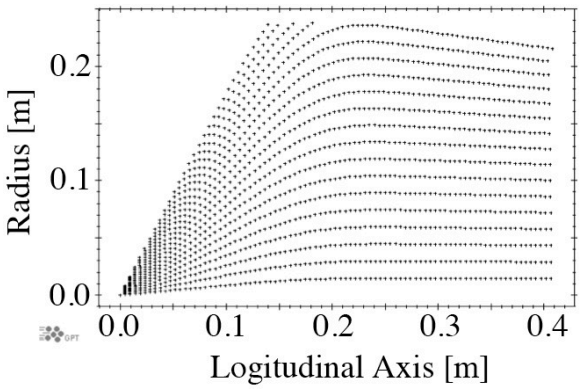

Figure 3.4: Ray tracing of a single energy showing the spherical aberrations of HZDR's first generation solenoid design. The aberrations are a result of increased focal powers at larger radii (Figure 3.5).

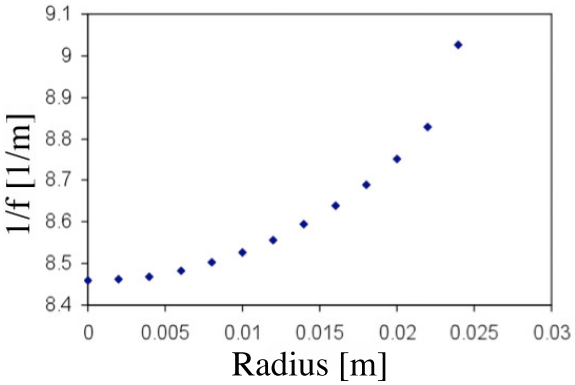

Figure 3.5: Focal powers determined from equation 3.3 for HZDR's first generation solenoid design. The increased focal powers at higher radii are directly responsible for the spherical aberrations seen in Figure 3.4

to focusing, as well as a 15° rotation.

Particle tracking was performed with General Particle Tracer [70] to predict the rotation and focusing of a laser accelerated proton beam passing through the solenoid. As dictated by the Lorentz force, the rotations and focal lengths are directly dependent on the particles' momenta, Figure 3.3. The solenoid, therefore, disperses protons outside of a given energy range, allowing it to act as a quasi-energy filter.

Spherical Aberration

Examination of proton trajectories shows that the focal strength increases as the distance off axis increases, Figure 3.4. Using the thin lens approximation of Equation 3.3 and the Biot Savart law,

$$\mathbf{B} = \frac{\mu_0}{4\pi} \int_C \frac{I d\mathbf{l} \times \mathbf{r}}{|\mathbf{r}|}, \tag{3.4}$$

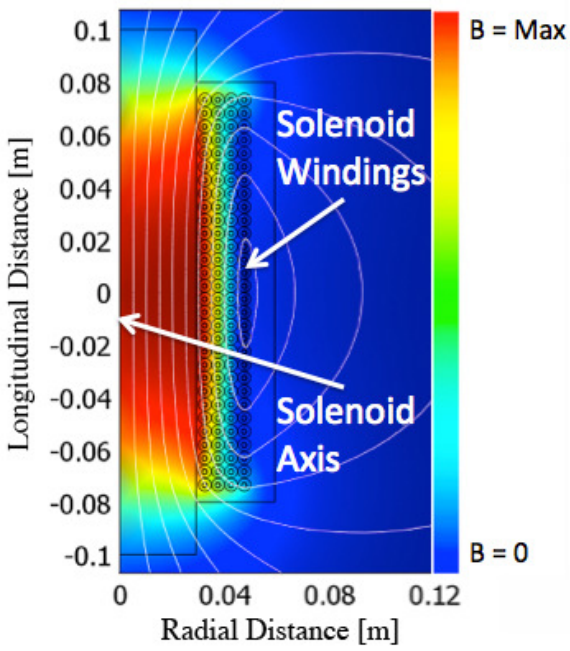

Figure 3.6: Magnetic field map generated by COMSOL for the first generation solenoid design. One can see the increased field strength at larger radii resulting in the focal powers seen in Figure 3.5 and the spherical aberrations seen in Figure 3.4.

a simple routine was written to integrate B_z^2 from $-\infty$ to ∞ along varying radii for the geometry of the first version solenoid to determine the focal power of the solenoid. The result is in agreement with the particle tracking and shows that the focal power of the solenoid is stronger at the edges compared to the center, Figure 3.5. In addition, the computer program COMSOL [71] was used to simulate a 2-dimensional field map of the solenoid, where radial magnetic field gradients are clearly seen to increase the magnetic field strength at larger radii, Figure 3.6. This is directly responsible for the increased focusing power at larger radii which is, by definition, the spherical aberrations of the solenoid.

Phase Space Analysis and Emittance

It was demonstrated [18] that laser accelerated protons possess ultra-low emittances: $\varepsilon_t < 0.004$ mm mrad and $\varepsilon_l < 10^{-4}$ eV s, which are at least 100 and 10^4 fold better than conventional accelerators, respectively. This and the laser's ability to accelerate

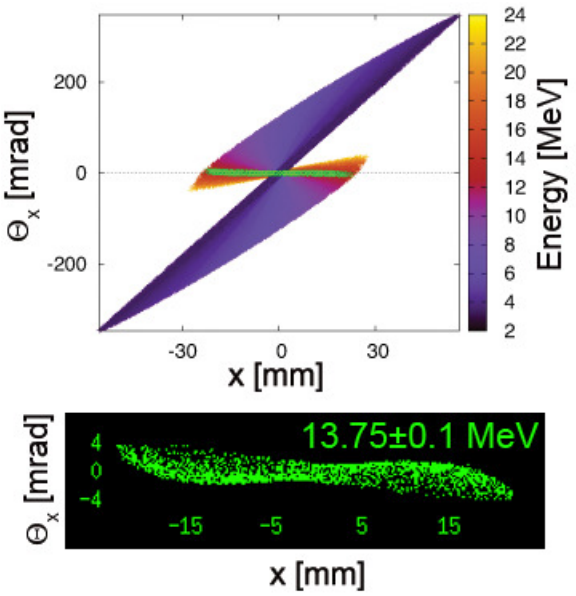

Figure 3.7: A phase-space plot of what we expect to see after protons accelerated by the PHELIX laser system are passed through an 8.5 T field of the pulse power solenoid. The 13.75 ± 0.1 MeV protons are highlighted in green, and their horizontal nature in the phase-space plot indicates that they will be collimated by the pulse power solenoid.

high yields of protons is what separates it from its conventional counterparts. The demonstrated high capture efficiency of the solenoid lens ensures the retention of the large particle numbers. However, chromatic, spherical and higher order aberrations influence the spectrum and emittance after the solenoid. For applications in high-energy physics, the capture and collimation of these high-yield, ultra-low emittance beams will ideally retain these advantageous beam characteristics, but the retention of ultra-low emittance may not be necessarily required for medical applications. Two questions arise at this point: What is the spectrum after the solenoid, and what is the effect of the aberrations on the emittance for a given energy, or energy range?

Simulation results from a phase-space analysis of laser accelerated protons tracked through an 8.5 T solenoidal field are presented in Figure 3.7. Details of the simulation and simulated proton source will be discussed in Chapter 4. The results illustrate the severity of the chromatic emittance growth after the solenoid lens when considering the entire proton population. This is a direct effect of the 100% energy spread in the proton beam. In this case, protons within a single energy range of 13.75 ± 1.25 MeV

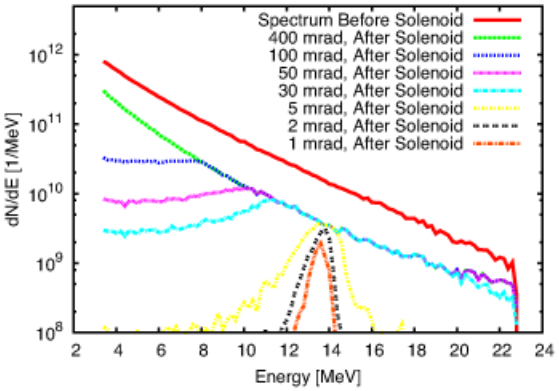

Figure 3.8: Post-solenoid spectra within different diverging beam envelopes for an 8.5 T field. As seen in Figure 3.7, many protons are contained within large divergence angles θ_x. Fewer protons are contained within small divergence angles.

are collimated or near collimated. As seen in Figure 3.3, low energy protons are over focused, and high energy protons continue to diverge but at a reduced angle. Although the lower energies diverge rapidly and the higher energies continue to diverge, protons accelerated on axis are unaffected by the radial and longitudinal magnetic fields. This results in a 100% energy spread in the proton population on axis after the solenoid, however, as seen in Figure 3.8, the density of protons on axis and outside of the desired collimation range is negligible compared to those that are collimated.

When one considers a single energy or smaller range of energies, the emittance is significantly smaller. An example of this is the collimation of 13.75 ± 0.1 MeV protons with the 8.5 T field. The resulting 1-σ and 2-σ emittances are 2.5 and 10.2 π mm mrad, respectively. This emittance is on par with that of low emittance conventional accelerators. Therefore, at the expense of loosing the ultra-low emittance in exchange for a low emittance, laser accelerators coupled to pulse power solenoids can produce a collimated proton beam and retain the high proton yields.

It was suggested that shortening the solenoid will lower the emittance growth [6], as the emittance scales as $\varepsilon = \alpha_c \Omega^2 (\Delta E/E)$. Here, $\Delta E/E$ is the collimated energy window, Ω is the maximum divergence angle of the protons and α_c has units of [m/rad] and is a geometric dependent constant which increases for longer solenoids

and larger target-to-solenoid distances. The shortening of the region containing the magnetic field will reduce the focusing power ($1/f \propto \int_{-\infty}^{\infty} B_z^2 dz$) unless there is compensation with a larger field strength. This can be done by increasing the number of windings per length N/l or the driving current I, since the magnetic field strength $B = \mu_0 NI/l$.

3.2.4 Pulse Power Sources

The HZDR Pulsers

The high voltages used to drive temporally short currents in the solenoid are supplied by a pulser. The pulser can be a single capacitor, a bank of capacitors or even a Marx generator. In the work presented here, two pulsers were used, and their basic circuitry followed the diagram illustrated in Figure 3.9. The rise time, $t_{rise} = \pi/(2\omega)$, of the solenoid's magnetic field is determined by the angular frequency $\omega = (LC)^{-1/2} = 2\pi f_B$ of the capacitor-inductor circuit (LC circuit) and plays an important role with induced currents as will be discussed in Section 3.2.5. There are two important points to be made about pulse power sources. One is that a great deal of energy [kJ] can be stored in the capacitor, and this energy can be released quickly resulting in a large power source. Two is seen when looking at the energy deposited in the circuit which follows the power law $P = I^2 R$ where I is the current in the circuit and R is the resistance of the circuit. Temporally short pulses allow the energy deposited within the conductor by even a high current to remain low. For example, during $t_{rise} = 400$ μs, a 16 kA current across the solenoid results in a near 3° C temperature increase.

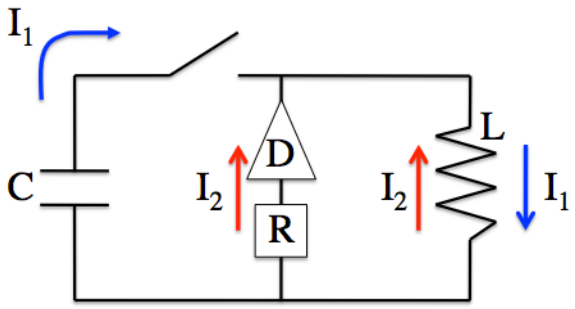

Figure 3.9: Basic schemaic of the capacitor-solenoid circuit. The blue arrows indicate the direction of the current as it approaches its maximum I_{max}. During this time, the diode blocks the path across the resistor. At I_{max}, the voltage reverses and the current passes through a resistor. Choosing R = 2Ω ensures that the current is critically damped.

The first pulser is driven by a bank of 5 capacitors with 250 μF in total. It can deliver 32 kJ of energy at a maximum voltage of 16 kV. Its trigger is an ignitron capable of withstanding currents up to 250 kA. This makes the pulser valuable for low inductance (i.e fast magnetic field rise times, τ [ns]), high field generation, and experiments have been planned to study laser-matter interaction in 100 T magnetic fields using this system. This pulser was used during the commissioning of early solenoid designs but was eventually sent to the LULI laser system at the École Polytechnique in Palaiseau, France. The second pulser, Figure 3.10, is driven by a single 50 kJ, 164 μF capacitor. It is designed to be smaller and more mobile than the first pulser, allowing it to travel to different institutions around Europe. Its maximum voltage is limited to 16 kV, and it is switched by a thyratron. Both systems charge relatively quick from 430 V, 32 A power. The first pulser can be fully charged in a few seconds, while the second pulser can reach a full charge at nearly 0.5 Hz.

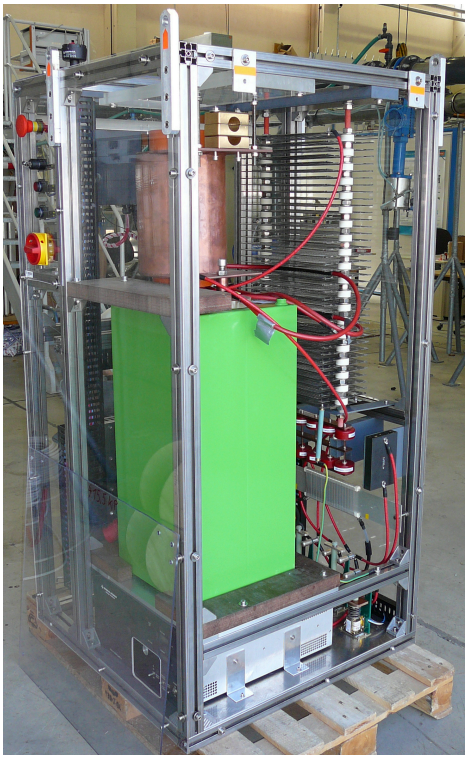

Figure 3.10: Pulser number two for the pulse power project at HZDR. The pulser is under 2 m in hight and houses a single 50 kJ, 164 μF capacitor. It can hold up to 4 C of charge and is limited to a maximum voltage of 16 kV. It was designed to be compact to allow for easy transport and to accommodate a small foot-print in an experimental hall.

Ideas for High Rep. Rate Systems

The more significant limitation of pulse power technology does not come from the scalability of the magnetic field, as discussed in Section 3.2.1, but rather with the repetition rate of the pulser, which must match that of the laser. The repetition rate of a medical laser accelerator will need to be high enough to keep treatment times to a few minutes or less, since the shot rate must compensate for the number of protons available per shot. Ti:Sapphire lasers already operate at several Joules per shot and 10 Hz and may one day operate at higher rates. The larger and more energetic lasers presently operate at around one pulse per 60 to 90 minutes, because their optical components need time to cool. Novel cooling techniques are being developed to increase the repetition rates. For example, the Mercury laser at Lawrence Livermore National Laboratory uses slabs of ytterbium-strontium flouroapatite crystals for their

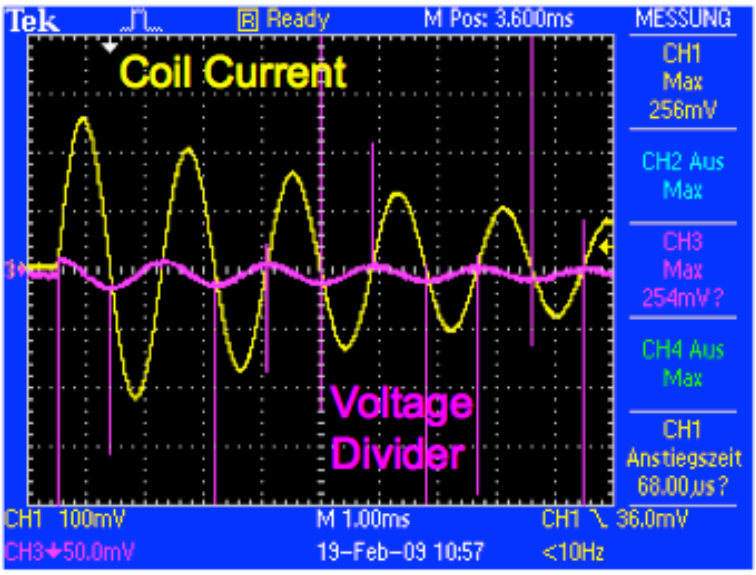

Figure 3.11: Measurements of the current and voltage for the initial underdamped capacitor-solenoid circuit. The current (yellow curve) is out of phase from the voltage (purple curve) by $\pi/2$. The oscillations prolong the resistive heating of the solenoid. A crowbar diode and 2 Ohms of resistance were added to the circuit (Figure 3.9) to critically damp the fall (Figure 3.14).

gain medium, and passes a sub-sonic[8] helium gas across them that keeps them cool. In 2007, the 10 Hz system was at a stage that could operate at 55 J per shot for seven hours and 61 J per shot for several minutes [72].

The HZDR pulser's repetition rate is mostly limited by the charging time, because the voltage between the capacitor's poles follows $V_{capacitor} = V_0[1 - \exp(-t/RC)]$. For these systems, the resistance R, the capacitance C and the DC source of voltage V_0 are fixed. Hypothetically, the charging rate will significantly increase if $V_{capacitor}$ is initially near the desired voltage, and this may not be so difficult to accomplish. As seen in Figure 3.11, the circuit was underdamped and the voltage oscillated until all the energy dissipated and the remote grounding relays closed. One may be able to use a fast switch, such as a thyristor, and close the circuit when the voltage reaches a maximum on the back-swing (i.e. at the moment the current returns to

[8] 0.1 Mach

zero before switching directions). The residual charge on the capacitor will ensure that $V_{capacitor} >> 0$, thus reducing the charge time. This is not a new technique and is commonly utilized in industry.

Scaling the Power Source

If laser acceleration eventually produces 250 MeV protons, the next generation pulsers will need to drive a list of beam transport elements to first capture and then bend the particles around and into the patient. This will require a more energetic pulser or many pulsers driving certain elements. The energy stored in the capacitor-system follows $E = (1/2)CV^2$, so for a desired voltage V, one needs to scale the capacitance C. This is easily done by increasing the number of capacitors in the system. It is reasonable to assume that a compact bank of capacitors can drive an entire beam transport system while remaining cost effective.

3.2.5 Characterizing Eddy Current Effects

When interacting with a conductor, the changing magnetic field $\partial\mathbf{B}/\partial t = -\nabla \times \mathbf{E}$ induces an electromotive force (EMF) and eddy currents. The diffusion into the conductor is governed by the frequency ω of the field and the material's electrical conductivity σ and magnetic permeability μ. These induced currents oppose the driving magnetic field and, therefore, oppose the diffusion of the field into the conductor, Figure 8.4. The depth at which the field is reduced to $1/e = 1/2.718...$ of its value is termed the skin depth $\delta = \sqrt{1/\pi f_B \mu\sigma} = \sqrt{2/\mu\sigma\omega}$. The velocity of the diffusion into the conductor then follows $v_d = \delta\omega$. For copper, $\sigma = 5.96 \times 10^7$ [S/m], and with $\omega = 5000$ the skin depth $\delta = 2.3$ mm and the diffusion velocity $v_d = 11.6$

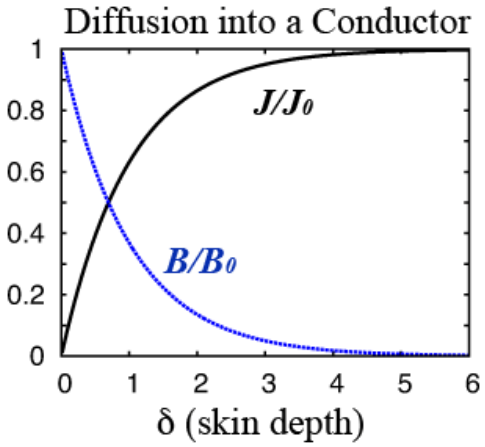

Figure 3.12: Magnetic field diffusion into a conductor and the resulting induced current density as a function of skin depth. The magnetic field B is normalized to B_0, the field the surface boundary of the conductor, and the induced current density J is normalized to $J0$ which is the total induced current density found by integrating J from the surface to a depth $d = \infty$

m/s.

As demonstrated in Appendix 8.4, the diffusion equations follows,

$$\alpha \nabla^2 \mathbf{A} = \frac{\partial \mathbf{A}}{\partial t}$$

for $\mathbf{A} = \mathbf{H}$, $\mathbf{B}$, $\mathbf{E}$ and $\mathbf{J}$. Here $\alpha = 1/\mu\sigma$ is the diffusivity which has the units of $[\mathrm{m}^2/\mathrm{s}]$. What this tells us is that the higher the diffusivity, the more rapidly a magnetic field will penetrate a conductor. Therefore, higher conductivities σ result in slower penetration speeds and shallower skid depths. This is because the higher conductivity allows for larger eddy currents to flow, which in turn oppose the penetrating magnetic field. Induced currents in conducting eddy shields can provide a shielding effect by matching the proper conductivity and material thickness to the frequency of the magnetic field.

The eddy currents act to prevent the penetration of the magnetic field into the conductor by generating magnetic moments $\mathbf{m}$ that oppose the driving magnetic field $\mathbf{B}$. Left unshielded, these induced fields become a concern since they may be strong enough to torque ($\boldsymbol{\tau} = \mathbf{m} \times \mathbf{B}$) metal optical components, defocus metal target foils or influence proton trajectories. Since the end goal of this work is to develop a com-

Figure 3.13: A Cu pipe with a 3 mm wall was placed inside the bore of the solenoid before pulsing to 16 T within a rise time of 400 μs. There is a solid Al bolt inside the pipe. The induced Eddy currents generated a $\mathbf{J} \times \mathbf{B}$ pinching effect that squeezed the pipe around the bolt. If the field can bend metal, there is a concern that it can move optical mounts place near the solenoid.

pact accelerator and beam transport system, understanding eddy currents becomes important. An extreme example illustrating the forces generated by the interaction of the eddy currents with the magnetic fields is presented in Figure 3.13. Here, a 3 mm copper cylinder placed inside the bore of the solenoid was pinched around a long aluminum bolt solely by the changing magnetic field.

As already mentioned, the thickness and conductivity of the conductor play a role in the induced fields. Most of the induced current in a conductor is concentrated at its surface. The current at a depth d follows $J = J_0(1 - e^{-d/\delta})$, where again the skin depth δ is the penetration depth within the conductor at which the magnetic field is reduced by a factor of $1/e$ (or to approximately to 36.8% of its original value). The rise times of the solenoids used in this work were between 330 and 400 μs, Figure 3.14, which leads to skin depths of 3.0 mm and 3.3 mm for aluminum and 2.4 mm and 2.6 mm for copper.

There was concern that induced currents within the target foil would generate a longitudinal movement and lead to a defocusing of the laser and a reduction of laser intensity. We considered that the doubling of the focal spot area, and not more, was acceptable. The maximum allowable longitudinal motion could then be calculated by the Rayleigh length $Z_R = \pi\omega_0^2/\lambda_L$ where ω_0 is the beam waist radius. For the

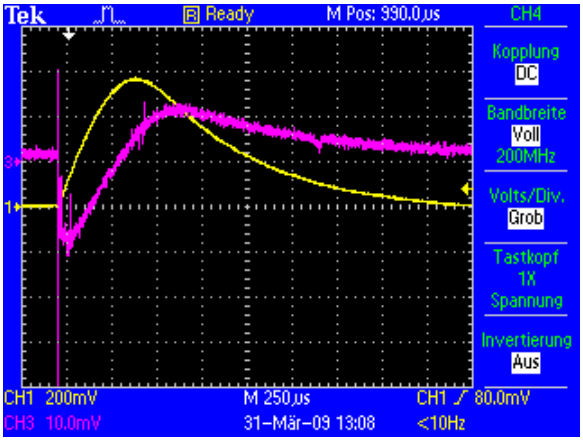

Figure 3.14: Plot of measured current (yellow curve) and voltage (purple curve) through the solenoid as a function of time. The magnetic field has a rise-time of 400 μs and a critically damped fall-time under 2 ms. The magnetic field can be considered static since the proton acceleration time is on the ps timescale and propagation time through the magnetic field is on the ns timescale.

DRACO laser ($\omega_0 = 2$ μm, $\lambda_L = 800$ nm) and the PHELIX laser ($\omega_0 = 8.5$ μm, $\lambda_L = 1.054$ μm), our constraints allowed for a longitudinal movement $Z \leq 16$ μm and 215 μm respectively.

Initial tests on target movement assumed a DRACO style set-up, Figure 3.15, as its large targets were the most susceptible to the magnetic pressure and there were and are future plans to couple the two systems for applications in beam transport and possibly dosimetric measurements of in-vitro cell irradiation[9] [73]. Additionally, a future laser proton accelerator may require high shot-density, large target foils like those used on DRACO. The set-up used a 6 cm diameter, 13 μm thick aluminum flat foil target. It was secured in a plastic target holder and placed on axis at 10 cm from the solenoid windings. Target motion was determined by reflecting a He-Ne laser off the aluminum target and onto a Position Sensitive Diode (PSD[10]), Figure 3.16. The laser light on the diode surface induced two voltage outputs - one for each transverse axis. Two lenses were placed before the PSD to magnify the sensitivity of the system.

[9]The in-vitro cell irradiation experiments mentioned here use laser accelerated protons to systematically irradiate single layers of biological cell cultures. The purpose is to determine the effects of ultra-high dose rates on cell survival and DNA double-strand breaks. These measurements provide a necessary comparison with conventional proton therapy dose-rates.

[10]S2044 Two-Dimensional PSD, Hamamatsu Photonics K.K., Solid State Division, www.hamamatsu.com

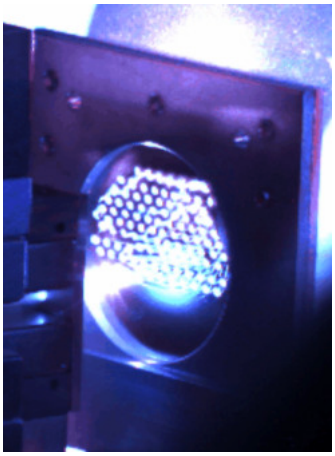

Figure 3.15: Image of the target foil in the DRACO target chamber during a cell irradiation experiment [73]. The OAP is lit in the background.

The left oscilloscope reading in Figure 3.17 shows the measured current though the solenoid and the two voltages output by the PSD. As indicated by the change in the PSD outputs, there is clear movement of the reflected laser light during the rise of the magnetic field. The maximum voltage change was converted to the maximum displacement across the diode. Two assumptions were made. One was that the pressure pushing on the target caused it to form a spherical shape. The second was that the displacement was so small that the position of incident laser light on the target foil remained unchanged. This position and the change in the reflected angle gave a rough estimation that the maximum displacement was between 50 and 100 μm. This length greater than the Rayleigh range for the DRACO laser. The right oscilloscope reading in Figure 3.17 shows the effect of an eddy shield on the same set-up [Note purple curve (CH3) settings: 200 mV per division in left image and 1.0 V per division in right image]. The eddy shield was a 20 mm thick, 300 mm diameter aluminum plate. This thickness is equal to 6 skin depths which confines $1 - 1/e^6 = 99.8\%$ of the inducible current. The plate was centered between the solenoid windings and the target. With the exception of the EMP spike at the moment of discharge, the measured PSD voltage remained unchanged during the rise of the field, i.e. no target movement was measured because the eddy shield reshaped the

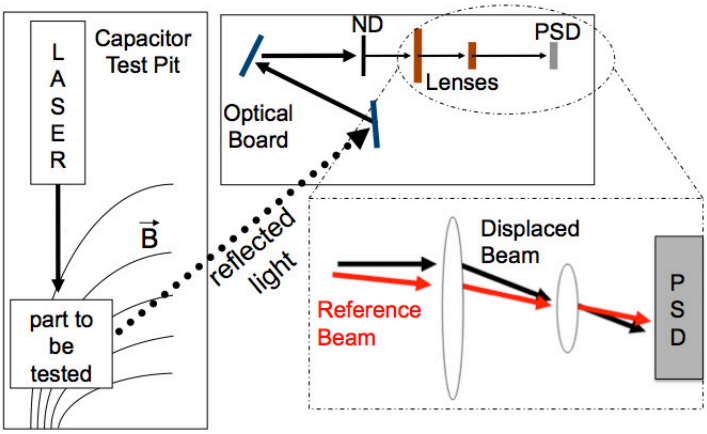

Figure 3.16: Experimental set-up for measuring induced motion in flat foil targets, optical mounts, OAP mounts and other conductive components near the solenoid's changing magnetic field. The laser, solenoid and pulser were located in the capacitor test pit of the High Magnetic Field Lab at HZDR. A series of mirrors, neutral density (ND) filters, lenses and a position sensitive diode (PSD) were placed on an optical table and outside of the test pit. The part to be tested was placed in a region of changing magnetic field, and the laser light was reflected off the part and sent to the PSD. Induced motion in the part was detected by movement of the laser light on the PSD surface.

magnetic field lines, Figure 3.18.

The field lines in the unshielded simulation (Left) reach the target positioned 100 mm from the solenoid and even extend outside of the plot boundaries. The shielded simulation (right) shows a full containment of the field lines along the axis. During the fall of the oscillation (after the peak current has been reached and the voltage swings into the negative), a crowbar diode in the circuit is engaged. The diode is in series with a 2 Ω resistor, and both are in parallel to the capacitor. This critically damps the current to prevent voltage oscillations, but it also lengthens the temporal fall of the field. This then lowers the frequency of the magnetic field, increases the skin depth and reduces the effect of the eddy shield. As seen in the right image, the target foil begins to move. Its movement is slight compared to the unshielded case and indicates that a good portion of the magnetic field is till being shielded within

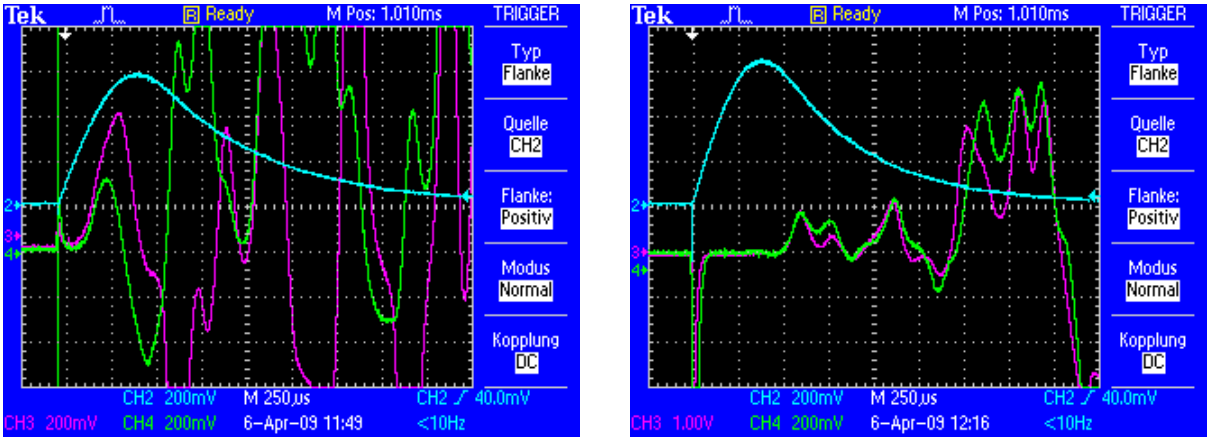

Figure 3.17: Oscilloscope measurements of induced target movement. **Left** The changing magnetic field (blue curve) induces eddy currents in the Al flat foil target. The movement of the target is recorded in both transverse planes by a position sensitive diode (green and purple curve). **Right** A conductive aluminum plate positioned between the target and solenoid eliminates target movement during the rise of the magnetic field. EMP from discharging the capacitor is responsible for the initial spikes on each channel.

the 20 mm of aluminum. A thicker eddy shield, or one made of higher conductivity, will only increase these shielding abilities.

Additional measurements of the eddy current effects were made on a 1-inch mirror mount and an aluminum OAP mount from the DRACO system. For both cases, laser light was reflected off a 1-inch mirror mounted to either the 1-inch mirror mount or the center of the OAP mount. The results revealed that even without an eddy shield, the OAP mount was unaffected by the eddy currents. The mirror mount showed movement when the field strength at the mount reached 0.18 T. In order to avoid induced motion, all 1-inch mirror mounts would need to be $\geq$ 20 cm away from the solenoid during a full-energy pulse (a distance easily achievable) or an eddy shield would be required. It was also determined that there was no effect of eddy currents on the motor stages or their position memory, even when the motor was placed 2 cm on axis from the solenoid windings.

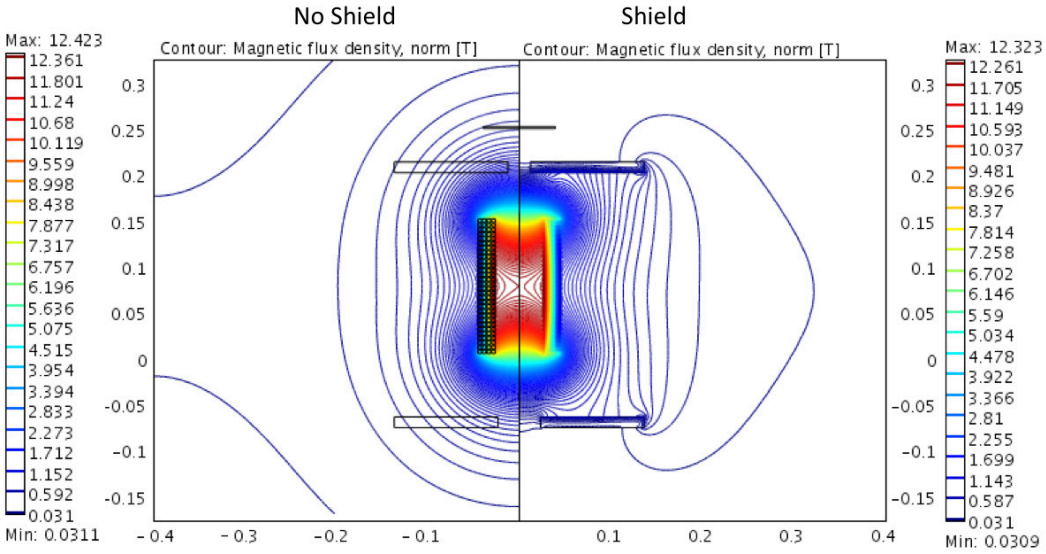

Figure 3.18: Comparison of magnetic contour lines for an un-shielded (left) and shielded (right) solenoid in the radial (horizontal axis [m]) and longitudinal (vertical axis [m]) planes.

Since the eddy shield shapes the magnetic field lines, a question arrises as to how the new field lines alter the proton capture and transport. As discussed in Section 3.2.3, the protons must first gain an azimuthal velocity from the radial magnetic field before the longitudinal field can provide a focusing affect. The eddy shield in the simulation is a single aluminum plate (20 mm thick, 300 mm diameter diameter, 50 mm diameter hole at center). Its center rests at 60 mm in front of the solenoid, and the target foil is positioned in front of the eddy shield at a distance of 100 mm from the solenoid. Figure 3.19 shows the on-axis radial and longitudinal magnetic fields for both a shielded and an unshielded set-up. The variation between radial magnetic fields is negligible. Therefore, the variation between the induced azimuthal velocities in either case is also negligible. The difference between the longitudinal magnetic fields is clearly seen, but this variation occurs almost entirely before the azimuthal velocity is induced. The result, which was confirmed by particle tracing, is that the focusing remains unaffected for this particular set-up.

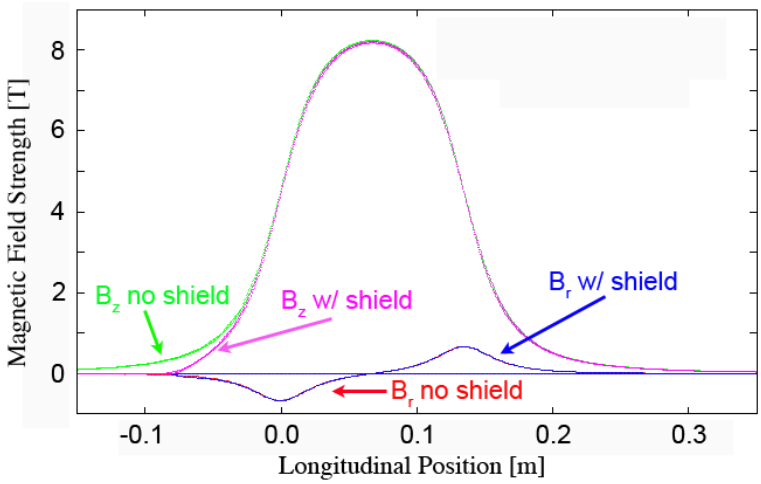

Figure 3.19: Comparison of on-axis longitudinal magnetic fields B_z and 0.01 cm off-axis radial magnetic fields B_r for a solenoid with an eddy shield (labeled: w/ shield) and without an eddy shield (labeled: no shield). The eddy shield was a 5 mm copper discs with a 300 mm diameter placed 50 mm in front of the solenoid entrance (i.e. at -0.05 m in on the x-axis). The disc had a 50 mm diameter hole bored at its center to allow protons to pass. The shielding effect on the longitudinal field is strong in the fringe-field region and negligible everywhere else. The effect on the radial field component is negligible everywhere.

There was also some concern that unshielded magnetic fields might induce magnetic fields that would alter proton trajectories. The largest conductor in close proximity to the solenoid is the aluminum optical board. To see the effect that this large conductor has on proton beam transport one can in principle use COMSOL to generate the superposition of the induced magnetic fields with the solenoid's magnetic fields. Unfortunately, this geometric set-up is non-symmetric (Figure 3.20) and needs to be simulated in a 3-dimensional environment as opposed to the more simple 2-dimensional environments offered in the previously mentioned eddy shield geometries. The machine running COMSOL did not have enough memory to complete such a complex simulation, however, an approximation of the field superposition was made using a self-developed Fortran routine.

The solenoid model is based on the first generation solenoid design and is approxi-

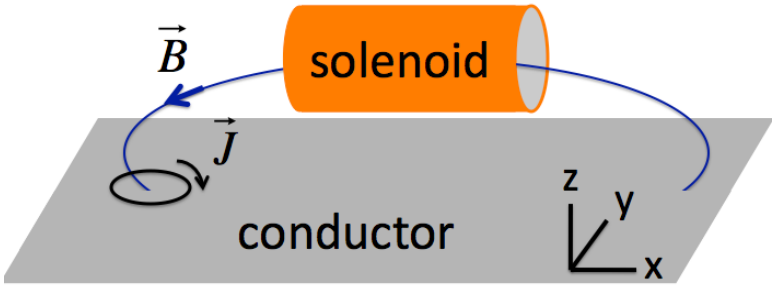

Figure 3.20: Illustration of the solenoid's magnetic field inducing currents in an aluminum optical board.

mated with 4 layers of 30 concentric current loops per layer (total current loops = 120). The radii are $a = 2.7$ mm, 3.2 mm, 3.7 mm and 4.2 mm, and the current loops are separated by 0.5 mm longitudinally. Each current loop is centered 200 mm above the optical board, Figure 3.20. The routine divides the optical board into discrete volume elements and calculates the solenoid's magnetic field at the center of each element. This induces a current density and generates a magnetic moment that is represented by a sphere with a diameter equal to one skin depth ($\delta_{Al} = 3.3$mm for the 400 μs rise time). This moment is now the source of the induced magnetic fields and can be used to calculate the induced fields along the path of the protons.

The longitudinal magnetic field B_z and the radial magnetic field B_r from each current loop (i.e. the source fields) are found at the center of each sphere using the Biot Savart law,

$$B_z = \frac{B_0}{\pi\sqrt{Q}}[E(k)\frac{1-\alpha^2-\beta^2}{Q-4\alpha} + K(k)]$$

$$B_r = \frac{B_0\gamma}{\pi\sqrt{Q}}[E(k)\frac{1+\alpha^2+\beta^2}{Q-4\alpha} - K(k)] \; . \tag{3.5}$$

Here, $E(k)$ and $K(k)$ are the elliptical integrals of the first and second kind, respec-

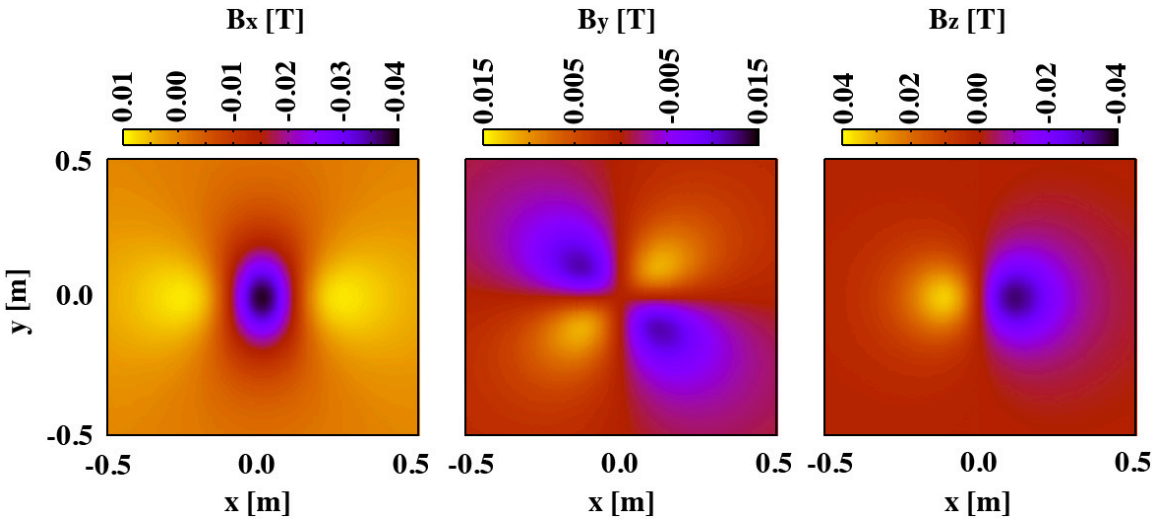

Figure 3.21: Magnetic field components at the optical board from the solenoid driven at 10 kA.

tively, r is the distance from the center of the current loop to the center of the sphere, $\alpha = r/a$, $\beta = z/a$ and $\gamma = z/r$, where a is the radius of the current loop and r is the distance from the current loop's axis to the center of the sphere. Furthermore, $Q = [(1+\alpha)^2 + \beta^2]$ and $k = \sqrt{4\alpha/Q}$. The magnetic field components at the surface of the optical board due only to the solenoid is shown in Figure 3.21.

As discussed in Section 8.4 and illustrated in Figure 8.4, the penetration of the time varying magnetic field into the aluminum induces currents that follow $J = J_0(1 - e^{-d/\delta})$, where J_0 is the induced current for a fully absorbed field. The optical board, therefore, allows for 63.2% of the magnetic field to be converted into a current density within the first skin depth. It follows that down to two skin depths, 86.5% of the magnetic field is converted into a current density; three skin depths leads to 95%; and at infinity, the entire field is converted into induced currents. Since the majority of the induced currents are concentrated in the first skin depth, this becomes the relevant scale length and is the rationale for equating the sphere diameter to $\delta_{Al} = 2r_{sphere} = 3.3$ mm. To account for the fields induced in depths below one δ_{Al}, the

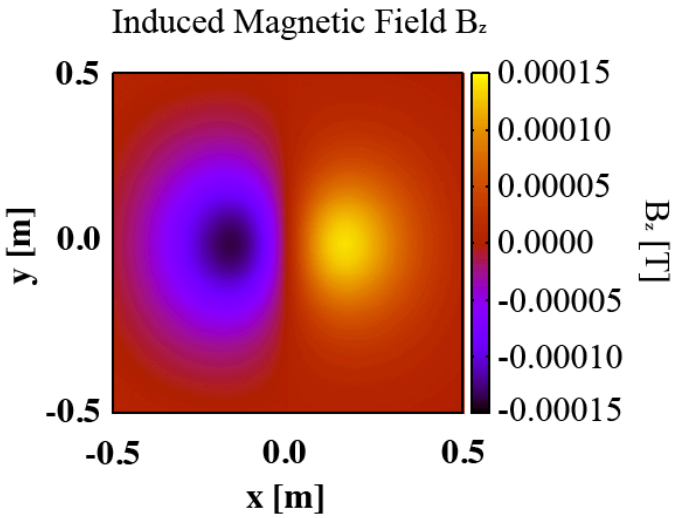

Figure 3.22: Induced magnetic fields B_z in a plane parallel to the optical board and centered on the solenoid axis.

current density is integrated to infinity. This results in a complete absorption of the magnetic field. This is a decent approximation since a 10 mm aluminum plate would absorb 95% of the field and a 20 mm plate would absorb 99.8% of the field.

The sphere now represents a magnetic dipole moment with an inner uniform magnetic field equal in magnitude but opposite in direction to the source field measured at the center of the sphere. The superposition of source and dipole fields at the optical board surface then cancel one another. At areas away from the optical board, the magnetic dipole field follows,

$$B_{z'} = \frac{\mu_0 M}{4\pi}[\frac{3cos^2\theta - 1}{R^3}] \tag{3.6}$$

$$B_{r'} = \frac{\mu_0 M}{4\pi}[\frac{3cos\theta sin\theta}{R^3}] \; . \tag{3.7}$$

Here, R is the distance from the dipole to the point of measurement, θ is the angle that subtends the dipole's magnetic field vector to the measurement point, M is the

magnetic dipole strength, and $B_{z'}$ and $B_{r'}$ are, respectively, the longitudinal and radial components of the dipole's magnetic field with respect to the dipole. Figure 3.22 presents the field distribution of B_z in a plane that is parallel to the optical board and centered on the solenoid axis. The magnitude of the magnetic fields from the superposition of the induced currents are between ±150.0 nT (±1.5 Gauss) on the axis of the solenoid.

The smallness of the induced field's magnitude in this plane is no surprise. If we consider the flux generated by the solenoid, it is largest within the windings where the magnetic field lines are confined to the solenoid bore. The flux outside of the solenoid can reach to infinite areas, which hugely reduces the magnetic field outside of a solenoid. Together, the small source field in the optical board and the $1/r^3$ fall-off keep the induced magnetic field weak back at the axis of the solenoid.

3.2.6 Forces within a Solenoid

The scaling the magnetic field to larger field strengths also scales the forces acting on the solenoid. The forces within the pulse power solenoid arise largely from the magnetic pressure pushing on the current carrying wires. Although eddy forces are present, they are small and contribute far less to mechanical stress. The time varying flux remains small along with the induced voltage, $|\varepsilon_{EMF}| = |d\phi/dt|$, because the eddy currents are confined within small regions of the small cross-sectional wires. For fast ($\approx \mu$s) rise times, the localized heating can generate shocks within the windings and plasma on their surfaces [74], however, the coils used in this work have rise times that are far too long for this to occur.

The magnetic pressure within the solenoid is directly dependent on the magnetic field

strength, regardless of its rate of change. Therefore, analytical approximations to the maximum strength of the forces acting on the windings are done using the value of the maximum current. Since conservation of energy requires that external work done by the magnetic force does so at the expense of the magnetic energy stored in the system, $\mathbf{F}_{B,i} \cdot \delta\mathbf{x} = -\delta U_B$. This can be elaborated on by looking at the magnetic flux $\Phi_B = B_z A$ and the inductance $L = N\Phi_B/I$ for a long solenoid. Here, $B_z = \mu_0 NI/l$ [T]. This is the longitudinal magnetic field for an ideal solenoid with current I where N/l is the number of current loops per unit length and A is the area of the solenoid's bore. Since the energy in the field obeys,

$$\begin{aligned} U_B &= \frac{1}{2} L I^2 \\ &= \mu_0 \frac{N^2 I^2 A}{2l} \ , \end{aligned} \tag{3.8}$$

the longitudinal force becomes,

$$F_z = \frac{dU_B}{dl} = -\mu_0 \frac{N^2 I^2 A}{2l^2} \tag{3.9}$$

in units of Newtons. The force is proportional to the square of the current, $F_z \propto I^2$, and squeezes the windings longitudinally inward. Similarly, noting that $A = \pi r^2$, the radial force is,

$$F_r = \frac{dU_B}{dr} = \mu_0 \frac{N^2 I^2 \pi r}{l} \ . \tag{3.10}$$

Again, the force is proportional to the square of the current, $F_r \propto I^2$ but is now radially outward. The significance of this I^2 scaling is seen when one considers future applications. As mentioned earlier for the solenoid design used in this work, the magnetic field $B \propto I$ will need to scale by a factor of 2.4 to capture and collimate 250

MeV protons. The I^2 scaling then increases the forces on the windings by $2.4^2 \approx 5.76$, and the structural integrity during such a high field pulse has yet to be tested.

These results are approximations based on a long ideal solenoid made of concentric current loops. Longitudinal and radial forces were calculated using a time varying (AC) module in COMSOL and are presented in Figure 3.23 in units of kilo-Newtons. The time varying voltage peaked at16 kV which drove near 16 kA of peak current after the 400 μs rise time. Equations 3.9 and 3.10 yield the approximations of $F_z \approx 8$ kN and $F_r \approx 70$ kN. There is clearly some discrepancies between analytical results and the COMSOL results, but the COMSOL results for the wires at the center of the solenoid are not off by more than a small factor when compared to these analytical results. Therefore, the analytical approximations prove useful as a rough estimate.

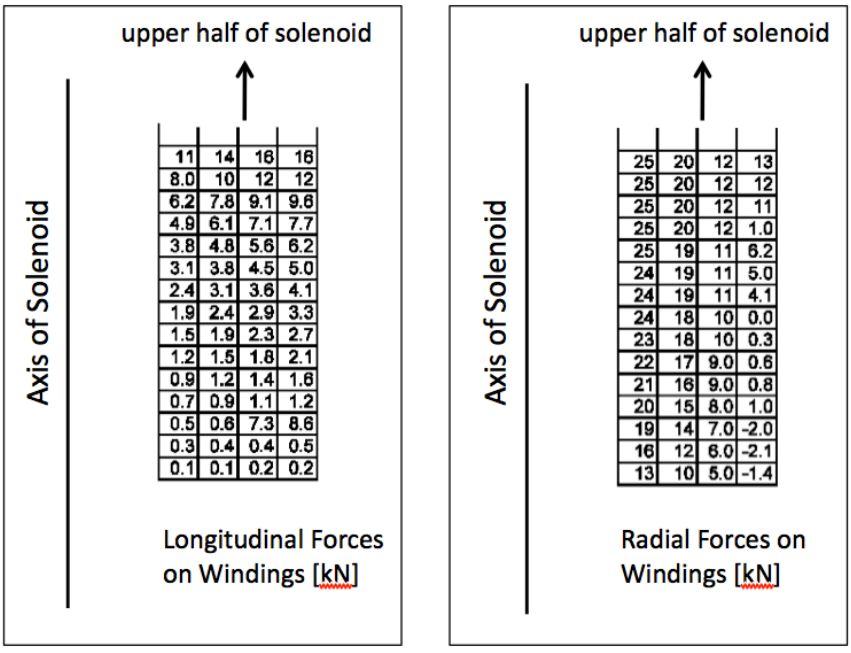

Figure 3.23: Longitudinal (left) and radial (right) forces [kN] on the solenoid windings from a 16 kV pulse with a 400 μs rise time. The solenoid modeled has 4 layers of 30 windings per layer. The wire dimensions are 3 mm by 4 mm. Due to symmetry, only the bottom half of the solenoid's windings are shown. The radii of the layers are 2.7, 3.2, 3.7 and 4.2 cm, and each layer is 150 mm in length.

3.2.7 Limitations of Pulse Power Technology

Pulse power magnets operate by rapidly applying voltages and currents significantly larger than what is used in DC resistive and DC superconducting systems. Limitations of these systems include induced currents in nearby conductive material from the rapid and strong dB/dt, mechanical stresses induced by the interaction between the current carrying wire and the magnetic field it generates, Ohmic heating due to high currents and high repetition rates, voltage breakdown resulting from the high potential of the pulse power supply and finally the need to use air-cores (i.e. the inability to incorporate μ-metal) where winding limitations can generate inhomogeneities in the magnet field. Although the thermal control and mechanical stress have not been a problem in this work, they may pose additional engineering challenges in future high repetition rate, high field systems.

The most significant limitation during this work was voltage breakdown, which here falls into two categories. The first category is associated with the breakdown mechanisms associated with high voltages that exist vacuum. These mechanisms can be triple-point emission [75], cascade emission from ionization via macro-particle impact [76, 77], enhanced electric fields from protrusions or bends in the current carrying wire or some combination of these [78, 79, 80]. The second category is the voltage breakdown on the high voltage circuit due to voltage spikes.

Here, we will begin with the first category of voltage breakdown; that associated with vacuum. The initial pulse power solenoid operated in vacuum and is thought to have suffered from triple-point emission (i.e. electron emission from enhanced electric fields at an insulator-conductor-vacuum boundary followed by an electron cascade) which resulted in a surface flashover, a charge cascade over the vacuum or both. Addi-

tionally, it is possible that loosely adhering materials were electrostatically repulsed off a wire lead. The bombardment of the material on the opposite lead can lead to localized ionization in addition to temperature increases leading to vaporization. This can initiate a voltage breakdown across the vacuum. Another possible reason for breakdown in vacuum may be electric field enhancements from rough surfaces or pointed areas on the copper leads. In any case, when the yield of ion emission by electron impact and the electron emission by ion impact and/or photon (i.e. one particle produces the other at the opposite poles) becomes great enough, breakdown occurs via charge cascade and a conducting channel is formed.

The frequency of the voltage also plays a role in the voltage breakdown processes. At vacuum pressures $> 10^{-6}$ mbar it was demonstrated that alternating currents have a lower breakdown voltage for a system compared to the system operating with direct current [81]. Our experiments operated between 10^{-5} and 10^{-6} mbar, well below the pressure resulting in the Paschen effect but still in a region where the alternating current may have lowered the breakdown voltage. Interestingly enough, at pressures $< 10^{-6}$ mbar, breakdown voltages rose for alternating current systems compared to direct current systems. The hypothesis put forward in Reference [81] is that the AC systems increased their voltage breakdown limits through conditioning. This occurs as the system operates and generates heat, thus removing contaminant layers and absorbed gases from the electrodes via evaporation. Reduction of the contaminants and gases reduces the possibility of them ionizing and generating a charge cascade. During the first experiment, we did not perform conditioning under vacuum, ironically, out of a fear of voltage breakdown. We therefore stepped up the voltage during the measurement process, but the vacuum chamber was openned after each pulse. In hindsight, conditioning may have increased the voltage breakdown

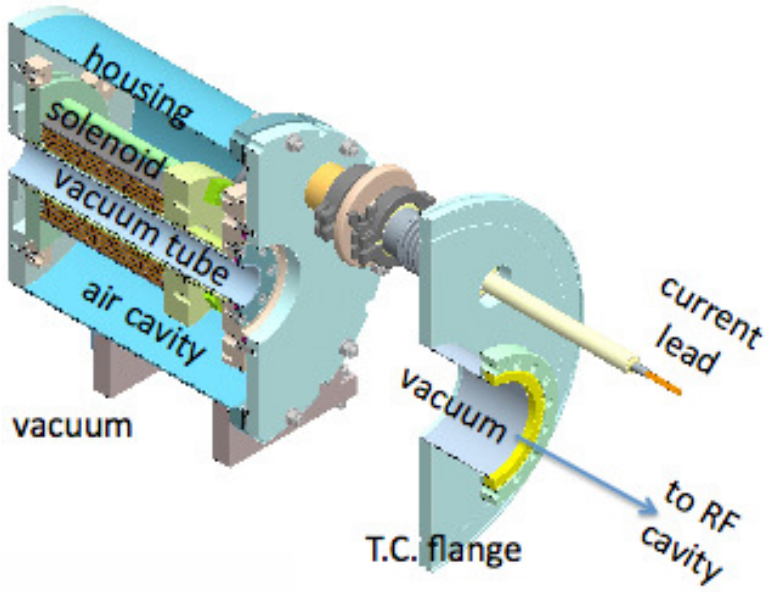

Figure 3.24: The encapsulated solenoid design for the Z6 target chamber. All conducting wires are separated from vacuum. The stainless steel housing is connected to the target chamber flange via two KF-40 bellows. According to COMSOL simulations, the eddy currents induced in the stainless steel reduce the magnetic field strength by 6%.

limit.

What followed the first experiment was an idea to improve the insulating characteristics of the system by eliminate the vacuum-conductor interface. Initial tests during the early research and development phases were performed in air without any voltage breakdowns over nearly 1000 pulses. Since air functions as a good insulator (at standard temperature and pressure), second generation solenoids were housed in stainless steel which incorporated additional insulations like Kapton, G-10 (a glass-reinforced epoxy laminate) and epoxy, Figure 3.24. The air between the solenoid and housing wall helped fortify the insulating properties [82], but these designs also suffered from voltage breakdown. It is believed that in the first encapsulated design, bubbles of trapped gas in the epoxy removed its insulating properties [83]. Strong fields can ionize the gas and accelerate the charges until they impact the wall of the insulator. The

impact releases more charges and a cascade and charge boring scheme follows.

The second category of voltage breakdowns was traced to mismatches of the impedances between the transmission line and the solenoid. The transmission line of length l can be characterized by its inductance L and its capacitance[11] C. For our transmission line, the characteristic impedance is $Z_0 = \sqrt{L/C} = 24.9\ \Omega$. Reflections can occur at the interfaces of components if their impedances do not match. The reflection coefficient describes the ratio of the reflected wave's amplitude to the incident wave's amplitude and follows

$$\Gamma = \frac{Z - Z_0}{Z + Z_0}\ . \tag{3.11}$$

When $Z = Z_0$, then $\Gamma = 0$, and there are no reflected waves.

Impedance is characterized by real values (from resistance) and complex values (from capacitance and inductance), and the phase shift by which the voltage lags the current is represented by the angle θ formed in the complex plane. The solenoid's impedance is $|Z| = \sqrt{R^2 + X_L^2} = 1.23\ \Omega$, where $X_L = 2\pi f L$ is the reactance for a frequency f. Our set-up possessed a $\Gamma = -0.88$, and the reflected voltage wave superpositioned with initial voltage to form a 1.88×16 kV $= 30$ kV spike across the thyratron. This lead to voltage breakdowns (surface flashovers) across the thyratron.

A simple solution to eliminate the voltage spikes is to introduce a terminating resistance on the capacitor end of the transmission line. To ensure that the resistor does not introduce reflected waves, its value should be matched with the impedance of the transmission line, i.e. $Z_0 = R$. Equating these values ensures that the resistor absorbs the reflected wave's energy, converting it to heat. What was immediately

[11] Energy can be stored in the capacitance of a coaxial transmission line. The current needed to charge a 300 nF/m coaxial cable follows $I_c = C_{coax} \times dV/dt = 300$ [nF/m] $\times 80$ [MV/s] $= 24$ [A/m]. This takes negligible current away from driving the solenoid.

available to us was a 21.5 Ω resistor. This gives a 7% voltage reflection that is sent back to the solenoid, while the remaining 93% of the wave is transmitted through the resistor and converted to heat. This results in a dampening of the high frequency voltage oscillations and a superposition voltage that is below the voltage breakdown limit of the circuit. Ideally, the resistance should be increased to $Z_0 = R = 24.9\ \Omega$, so that $\Gamma = 0$..

3.3 Alternatives to Pulse Power

Although the pulse power solenoid has been demonstrated to have large capture efficiencies and possesses a scalable magnetic field, alternative capture and collimating devices exist. The two alternatives presented in this subsection are permanent magnet quadrupoles (PMQs) and laser triggered plasma lenses. The PMQs may prove more suitable for other applications where the capture of low energy protons is desired, while the laser-triggered plasma lens may prove capable of scaling to capture high energy protons.

3.3.1 Laser-Triggered Plasma Lens

The laser-triggered plasma lens consists of a compact (3 mm long, 0.7 mm diameter) cylinder [53, 54]. Its electric field is driven by a short-pulse ($\tau = 350$ fs) high intensity ($I = 3 \times 10^{18}$ W/cm^2)) laser generating a TNSA-style charge separation on the inner wall of the cylinder. The initial phase consists of a Debye sheath generated by the hot electrons as they extend inwards towards the axis of the cylinder. The space charge field induces a plasma expansion off the inner walls of the cylinder which results in

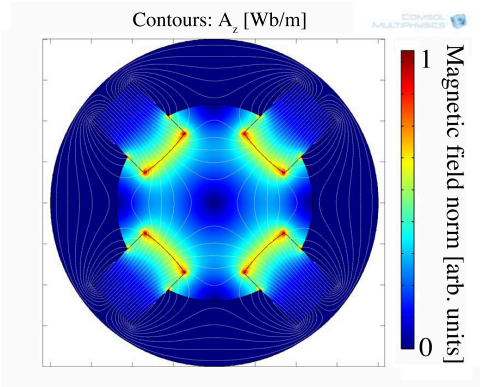

Figure 3.25: Magnetic field map of an electromagnetic quadrupole from COMSOL. The contour lines show the lack of azimuthal symmetry which is transferred to the proton beam after focusing which will increase the difficulty of spectral shaping and dose deposition.

strong, inward-pointing, radial electric fields. It was demonstrated that these fields are capable of collimating $\approx$ 7.5 MeV protons before propagating them to 70 cm behind the target.

The benefits of such an ion lens can be seen in its compactness and simplicity. However, the scaling of the electric field is questionable. Since the field generation relies on charge separation, one would need to increase the population of hot electrons to focus laser accelerated protons of higher energies. Also, as the proton energies increase, their interaction time in the electric field decreases requiring an even larger electric field to compensate. It may be, however, that these issues and uncertainties will be addressed, and this becomes an optional alternative to pulse power solenoids.

3.3.2 Permanent Magnet Quadrupoles (PMQs)

Permanent magnets are attractive because they are passive, but their strengths are limited and their aperture sizes are small. The field of an ideal permanent magnet quadrupole consists of four hyperbolic shaped poles, alternating north and south. Figure 3.25 illustrates the quadrupole field using an electromagnetic quadrupole, and in every practical sense, the field map's properties remains the same for PMQs. The poles generate a constant magnetic field gradient dB/dx with optical properties such

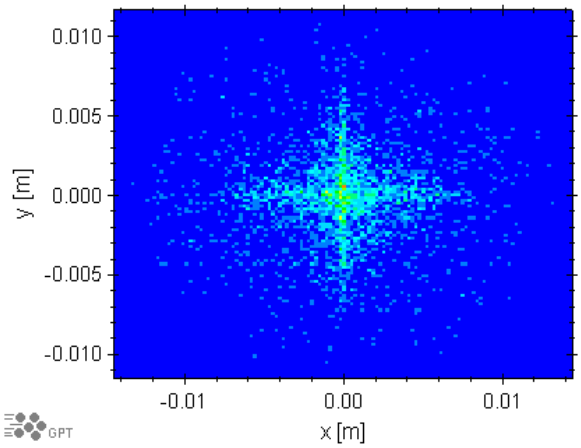

Figure 3.26: GPT simulation of a quadrupole triplet. The target to quadrupole distances (and field gradients) are 50 mm (105 T/m), 178.5 mm (-80 T/m) and 267.8 mm (110 T/m). The image captures the proton distribution at 1.25 m from the target. This triplet is capable of collimating 5.9 MeV protons. The star distribution pattern is characteristic of quadrupole doublets and triplets.

that a beam of charges passed through the PMQ is focused in one transverse plane and defocused in the other transverse plane. Properly combining two PMQs with one rotated 90° to the other forms a quadrupole doublet which can achieve an overall focusing in both planes. In addition to the weak focusing capabilities of PMQs, collimation of a laser accelerated proton beam with a doublet, or even with a triplet as shown in Figure 3.26, will result in an azimuthally non-symmetric proton distribution.

It was demonstrated that a PMQ doublet can focus 2.4 ± 0.1 MeV laser accelerated protons to a 3×8 mm^2 focal spot [7]. The field strengths were 55 and 60 T/m for the first and second PMQs, respectively, and the doublet had a capture efficiency of near 3%. Since the permanent magnetic field is at maximum on the order of 1 T and the focal power $1/f \propto dB/dx$, one must decrease the bore size of a PMQ in oder to generate a larger field gradient to capture higher energy protons. Through the use of smaller bore, 500 T/m PMQs, 14 ± 1 MeV protons were focused to a 286×173 μm^2 full-width half-max focal spot size at 50 cm behind the target [55]. The reduction in bore size, however, reduced the capture efficiency to 0.1%. It should also be noted that the reduction in bore diameter also resulted in capturing and focusing

the more paraxial protons instead of protons with any sizable divergence. Overall, PMQs offer a low capture efficiency for typical TNSA divergences. If, however, novel target designs can reduce the divergence of laser accelerated protons, then PMQs may become relevant.

Chapter 4

Simulation

As indicated in Chapter 3, a number of modeling and simulation programs were used in this work, two of which are commercially available. General Particle Tracer (GPT) [70] (Section 4.1) is a particle tracking code (not to be confused with a tracing code as the name implies) that is well established and widely used in the accelerator community to design accelerators and beam lines. It comes with a list of ready-to-use beam elements and also allows for user defined elements. The other commercially available computer program is COMSOL Multi-Physics [71] (Section 4.2) which can model alternating current systems, the magnetic fields they generate, and the currents induced in nearby conducting materials. It can also model the spatial distribution of the current in the solenoid wires as well as determine the forces exerted on the wires. This has been a valuable tool in understanding induced currents and eddy shielding. COMSOL version 3.5 was used in this work, and the latest version, 4.2, has incorporated a particle tracking capability.

Space charge effects were studied with the particle-in-cell code WARPrz [84]. This

is presented in Chapter 6. Additionally, a Fortran routine to recreate the dose deposition and optical density response of RadioChromic Film was developed, Section 5. Additional routines were written in Fortran to generate a laser accelerated proton source using the Monte Carlo method (Section 4.1.5) and extract emittances and spectra from GPT's phase-space coordinates (Section 4.3.1)

4.1 Particle Tracking

Particle tracking has been invaluable for this project. 3-dimensional tracking results can be obtained before experimental results, which allows one to perform trial runs of the experiment, cross check empirical calculations, predict the severity of spherical aberrations and optimize the experimental set-up and conditions (e.g. ensuring that a film position corresponds with a focused proton beam). Additionally, with the aid of post-processing routines, particle tracking yields information about the capture and transport efficiencies, phase-space coordinates and lens aberrations. Electromagnetic fields can be generated by GPT or input from an external file. Beam elements (such as apertures, dipole magnets, current loops, etc.) can be arbitrarily defined, oriented and positioned. It was demonstrated in this thesis work that GPT provides a realistic model of beam capture experiments when combined with a simulated laser accelerated proton source.

4.1.1 Equations of Motion

GPT is based on a fifth order Runge-Kutta solver [85] with adaptive step-size control. This algorithm ensures the program's accuracy while keeping the calculation time to a

minimum. GPT reads the initial laser accelerated proton distribution (Section 4.1.5) and the 3-dimensional electromagnetic field configuration, if input from an ASCII input file. The number of laser accelerated protons tracked in the simulation was limited to no more than 10^7.

GPT solves the following relativistic equations of motion:

$$\frac{d\mathbf{p}_i}{dt} = \mathbf{F_i} \tag{4.1}$$

$$\frac{d\mathbf{x}_i}{dt} = \mathbf{v}_i = \frac{\mathbf{p}_i c}{\sqrt{\mathbf{p}_i^2 + m_i^2 c^2}} \tag{4.2}$$

where the coordinates of the i^{th} proton are given by the position $\mathbf{x}_i$ and the momentum $\mathbf{p}_i = \gamma m \mathbf{v}_i$, and each proton is subject to the Lorentz force, $\mathbf{F}_i = q(\mathbf{E}_i + \mathbf{v}_i \times \mathbf{B}_i)$. GPT is also capable of including space charge effects. With the space charge option enabled, the Lorentz force acting on a single particle will depend on the position of all the other particles in the simulation. Therefore, the equations of motion can not be individually solved, and GPT re-writes them as $d\mathbf{y}(t)/dt = \mathbf{f}(t, \mathbf{y}(t))$ where $\mathbf{f}(t, \mathbf{y}(t))$ is a combination of the above equations of motions. The reader is referred to reference [86] for more information about combining the equations of motion into $\mathbf{f}(t, \mathbf{y}(t))$. As discussed in Chapter 6, to accurately model space charge, the electron temperature needs to be characterized.

4.1.2 Solenoids

A solenoid in GPT is modeled with many concentric current loops. Each current loop represents a single loop in the helical winding of the physical solenoid. The solenoids used throughout this research each contained four layers of 26 to 30 windings per layer resulting in the simulation using between 104 and 120 current loops.

Each current loop follows the spherical coordinate representation of the vector potential,

$$A_\phi(r,\theta) = \frac{\mu_0 I R}{4\pi}\int_0^{2\pi} \frac{cos(\phi)}{\sqrt{R^2+r^2-2Rrsin(\theta)cos(\phi)}}d\phi \tag{4.3}$$

leading to the magnetic field $\mathbf{B} = \nabla \times \mathbf{A}$.

4.1.3 Quadrupoles

The user defined variables for the quadrupole elements are its length L and its magnetic field gradient $\mathbf{G}$[T/m]. In cartesian coordinates, the magnetic field follows,

$$\mathbf{B} = \begin{cases} (\mathbf{G}_y, \mathbf{G}_x, 0) & \text{if } |z| < L/2 \\ 0 & \text{otherwise} \end{cases} \tag{4.4}$$

and the scalar potential follows $\Phi = -G_{xy}$. Although quadrupoles prove too weak to provide efficient capture of laser accelerated protons, their value is demonstrated in their ability to correct for dispersion in the beam transport of a compact pulse power gantry as discussed in Chapter 7.

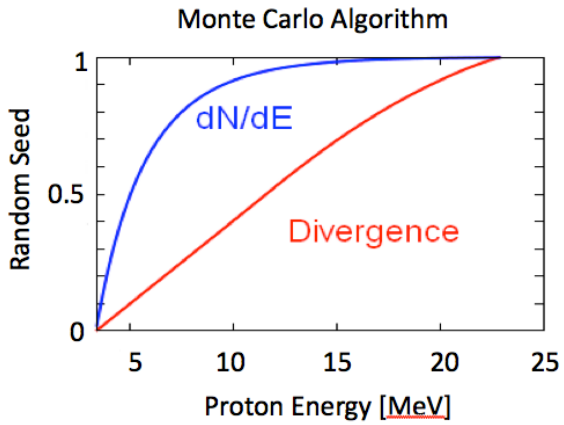

Figure 4.1: Probability distribution for energies and angles extracted from measurements using dosimetric film.

4.1.4 Sector Magnets

Sector magnets were used in the compact pulse power gantry feasibility study discussed in Chapter 7. In GPT, the user defines the bending radius R, maximum magnetic field $B = \pm mc\gamma\beta/qR$ and the incident and exit pole face angles. Fringe fields can be enabled, as discussed in Section 4.7.11 of the GPT manual, but without a physical pulse power magnet to base the model after, the fringe fields were left disabled and the sector magnets used in Chapter 7 were left as ideal magnets.

4.1.5 Proton Source Modeling with the Monte Carlo Method

General Particle Tracer was developed to assist in the design of conventional accelerators and beam lines. Therefore, all of the internal source configurations model conventional particle sources. As discussed in Chapter 2, the source of laser accelerated protons is nothing like a conventional proton source. Therefore, the proton distribution needed to be generated before particle tracking could be performed.

The simulated laser accelerated proton source is generated via the Monte Carlo method. Using FORTRAN, a routine was written to model the positions and mo-

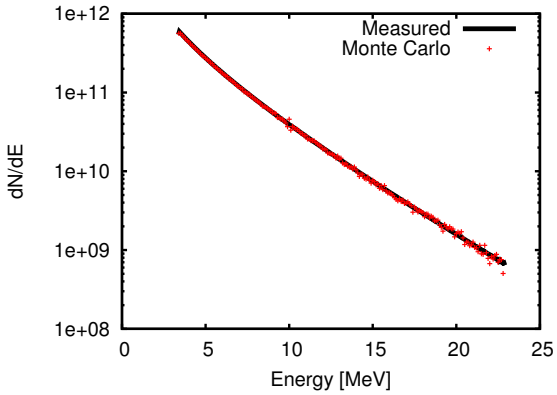

Figure 4.2: Comparison of the measured data (black line) and the Monte Carlo generated spectrum (red dots). The Monte Carlo input includes the probability distributions presented in Figure 4.1.

menta of laser accelerated protons as they emerge off the flat foil target. The input parameters are taken from direct measurements of the laser accelerated protons and include the energy-dependent half-angles through the use of a von Mises [87] distribution. The spectra dN/dE and the angular distribution θ of the measured laser accelerated protons yields two energy dependent probability distributions. These probability distributions are integrated and normalized to 1. The results are the curves in Figure 4.1. The desired number of protons can be set in the input file, and a random seed generator will produce statistically accurate values for dN/dE and θ based on the measured values.

The proton source is modeled after a point source. In reality, the accelerating sheath in TNSA has a finite size [88] near 400 μm for low energies (3 MeV) and near 50 μm for high energies (23 MeV). For the sizable geometries of a solenoid and the beam transport, it can be considered a point source. Figure 4.2 compairs the measured spectrum and the spectrum generated with the Monte Carlo algorithm.

4.2 COMSOL Multi-Physics

COMSOL Multiphysics is a software environment that was included in the simulation support of this thesis work to model the interaction of changing magnetic fields with conductive materials as discussed in Section 3.2.5 (eddy currents). This work used the AC/DC Module which is capable of modeling electrostatics, magnetostatics and electromagnetic quasi-statics. The user defines the geometries and the environmental characteristics such as the alternating current of a solenoid and the material, geometries and placement of conductive elements.

Some of the COMSOL results were introduced in Chapter 3. A comparison of shielded and un-shielded magnetic fields were illustrated in Figure 3.18. The longitudinal and radial magnetic field components along the axis of Figure 3.18 were presented Figure 3.19, and a magnetic field map illustrating a quadrupole field was presented in Figure 3.25.

4.3 Emittance Calculations

Sources of emittance growth come from chromatic aberrations resulting from the momentum dependent focusing, spherical and higher order aberrations and energy degradation (the latter is presented in Chapter 7). Because the emittance of laser accelerated protons is ultra-low, there is room for some emittance growth, however, retaining a low emittance is beneficial for an increased beam luminosity for High Energy Density physics applications. Emittance growth in medical physics applications must also remain small enough to not compromise dose deposition.

4.3.1 Emittance - Parametric Representation

Using a parametric representation, emittance ellipses along with their 1-σ and 2-σ values from the GPT phase-space coordinates were calculated. For particles moving in the z-direction, the beam emittance (ε) is generally characterized by the Twiss parameters α, β and γ. Both β and γ are always positive and α is negative for a divergent beam and positive for a convergent beam. These parameters are correlated by $\beta\gamma - \alpha^2 = 1$ and used to generate a 6-dimensional emittance ellipsoid in phase-space $(\mathbf{x}, \mathbf{x}')$. A two dimensional ellipse is found by projecting the ellipsoid onto a 2-dimensional subspace in x and $x' = dx/dz$. The area of the 2-dimensional emittance ellipse is, by definition, the emittance ($\varepsilon\pi$ = area). The number of protons within the emittance ellipse is determined by the applied standard deviation σ. For a Gaussian distribution of protons, a σ of 1, 2 and 3 will result in the ellipse surrounding 39%, 86% and 99% of the proton distribution, respectively. The 1σ deviation is also referred to as the root-mean-square emittance, ε_{rms}.

In the Courant-Snyder representation,

$$\varepsilon_{rms} = \gamma x^2 + 2\alpha x x' + \beta x'^2 \tag{4.5}$$

where $\alpha =< xx' > /\varepsilon_{rms}$, $\beta =< x^2 > /\varepsilon_{rms}$ and $\gamma =< x'^2 > /\varepsilon_{rms}$ are the Twiss parameters.

These parameters can be more easily extracted from GPT's phase-space coordinates using a parametric representation [89]. In this representation, the emittance ellipse is characterized by x_m (the maximum value of x), θ_m (the maximum value of x') and χ (the correlation phase characterizing the ellipse's orientation). Using,

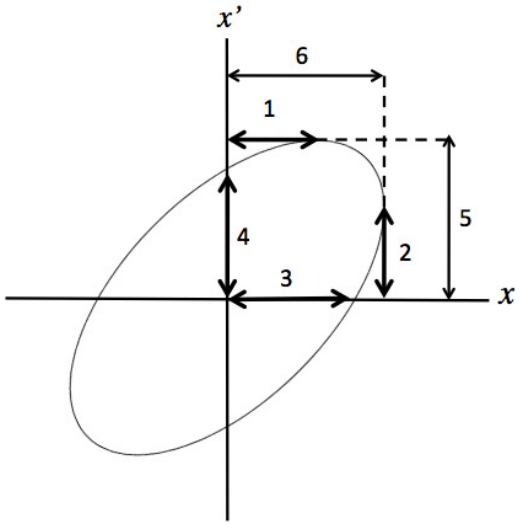

Arrow Label	Parametric	Courant-Snyder
1	$x_m sin(\chi)$	$-\alpha\sqrt{\varepsilon/\gamma}$
2	$\theta_m sin(\chi)$	$-\alpha\sqrt{\varepsilon/\beta}$
3	$x_m cos(\chi)$	$\sqrt{\varepsilon/\gamma}$
4	$\theta_m cos(\chi)$	$\sqrt{\varepsilon/\beta}$
5	θ_m	$\sqrt{\varepsilon\gamma}$
6	x_m	$\sqrt{\varepsilon\beta}$
	$tan(\chi) = x_2'/x_4' = x_1/x_3$	$\alpha = -x_2'/x_4' = -x_1/x_3$

Figure 4.3: Values of the parametric parameters and the Courant-Snyder parameters as illustrated on an emittance ellipse.

$$x = x_m cos(\delta) \tag{4.6}$$

$$x' = \theta_m sin(\delta + \chi) \tag{4.7}$$

an emittance ellipse is traced by varying the contour parameter $0 \leq \delta \leq 2\pi$. Figure 4.3 illustrates the connection between the parametric and Courant-Snyder representations on an emittance ellipse, and the connection between the main parametric parameters.

For an arbitrary distribution of protons,

$$x_m = \sigma\sqrt{< x^2 >} \tag{4.8}$$

$$\theta_m = \sigma\sqrt{< x'^2 >} \tag{4.9}$$

$$< x^2 >= \frac{1}{N}\sum_{i=1}^{N} x_i^2 \tag{4.10}$$

$$< x'^2 >= \frac{1}{N}\sum_{i=1}^{N} x'^2_i \tag{4.11}$$

$$< xx' >= \frac{1}{N}\sum_{i=1}^{N} x_i x'_i \tag{4.12}$$

$$\varepsilon_{rms}\pi = x_{m,1\sigma}\theta_{m,1\sigma}cos(\chi) = \sqrt{< x^2 >< x'^2 > - < xx' >} \tag{4.13}$$

$$\varepsilon_{2\sigma}\pi = x_{m,2\sigma}\theta_{m,2\sigma}cos(\chi) = 4\sqrt{< x^2 >< x'^2 > - < xx' >} \tag{4.14}$$

$$\varepsilon_{3\sigma}\pi = x_{m,3\sigma}\theta_{m,3\sigma}cos(\chi) = 9\sqrt{< x^2 >< x'^2 > - < xx' >} \tag{4.15}$$

4.3.2 Emittance Growth - Nonlinear Effects

Liouville's theorem [64] states that the proton distribution function in phase-space remains constant along the trajectories of the system. As discussed in Section 4.3.1, the emittance of a system is the elliptical area encompassing the proton distribution in phase-space. Therefore, if the distribution remains constant as Liouville's theorem asserts, then the emittance must also remain constant.

This assertion, however, only remains true for linear systems. The emittance calculation in Equation 4.5 came from an invariant transformation of the Hill's equation, $x"(s) + K(s)x(s) = 0$. Because Hill's equation is linear, emittance is not conserved in the presence of nonlinear effects, such as aberrations from a magnetic lens.

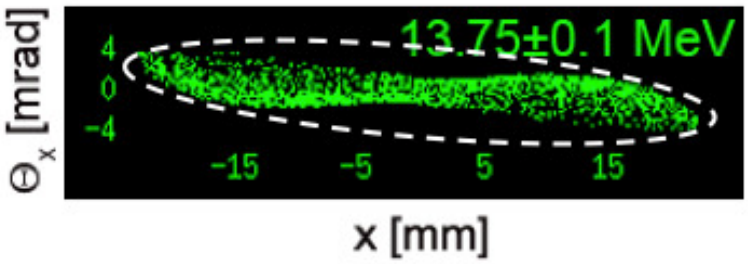

Figure 4.4: Illustration of filamentation for 13.73 ± 0.1 MeV protons after passage through an 8.5 T field. The nonlinear effects in this case are caused by spherical aberrations and lead to a spiraling of the proton distribution. To inclose all the protons inside an ellipse, the area of the ellipse must be increased, i.e. emittance grows.

Magnetic lens aberrations create what are known as filamentations[1]. Filamentation in accelerator and beam physics refers to the nonlinear imperfections that result in an amplitude dependent rotation frequency in phase-space. Severe filamentation results in spiraling of the particle distribution, mimicking two arms of a galaxy. As illustrated in Figure 4.4, the contour around this phase-space distribution is not a perfect ellipse. Instead, the outline has a slight spiral geometry at the ends. As one can predict, a larger filamentation expands the area of a fitted ellipse, directly increasing the emittance.

Another nonlinear effect occurs when protons are scattered. This situation is not presently problematic, but a future laser accelerator may require a proton energy degrader to shape proton spectra. The scatter from such a degrader will directly increase the emittance.

[1]Filamentation in accelerator and beam physics is not related to the filamentation of e^- in laser-solid interactions.

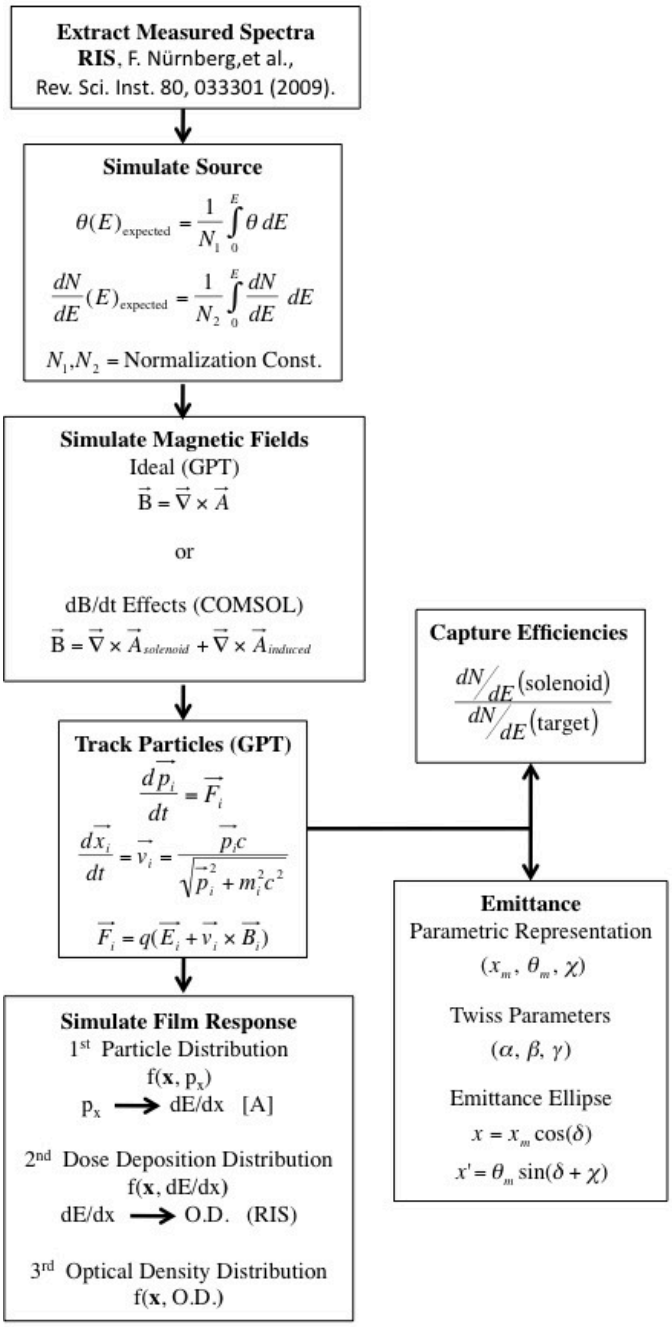

Figure 4.5: A flow chart of the simulations used in this thesis work. The simulated film response will be discussed in Chapter 5. The extraction of the spectrum and optical density response was obtained using RIS [48]. The calculation of the energy loss in RCF, cited as [A] in the flow chart, relies on output from a previously developed MatLab script [90].

Chapter 5

Results and Measurements

This project relied on both simulation results and experimental measurements, as they often depended on one another. For example, the simulation is based on measurements of the laser accelerated proton characteristics, which must first be measured and then extracted from the dosimetric films. Simulation then can provide tracking, expected dosimetric film responses and allow for the extraction of phase-space information and capture efficiencies. Experiments with the solenoid then confirm the tracking results. Because of this intertwined relationship between simulation and measurement, some results have already been presented.

All proton beam transport measurements were performed with the PHELIX laser system. PHELIX can be directed to three different target areas. Early proton capture and transport experiments were performed in the PHELIX Laser Hall (PLH), and after commissioning of the Z6 target chamber, later experiments were performed in the Z6 experimental area. The Z6 experimental area was developed for the LIGHT project[1] to inject laser accelerated protons into a conventional post-accelerating RF

[1]Laser Ion Generation, Handling and Transport (LIGHT) is a collaboration between the

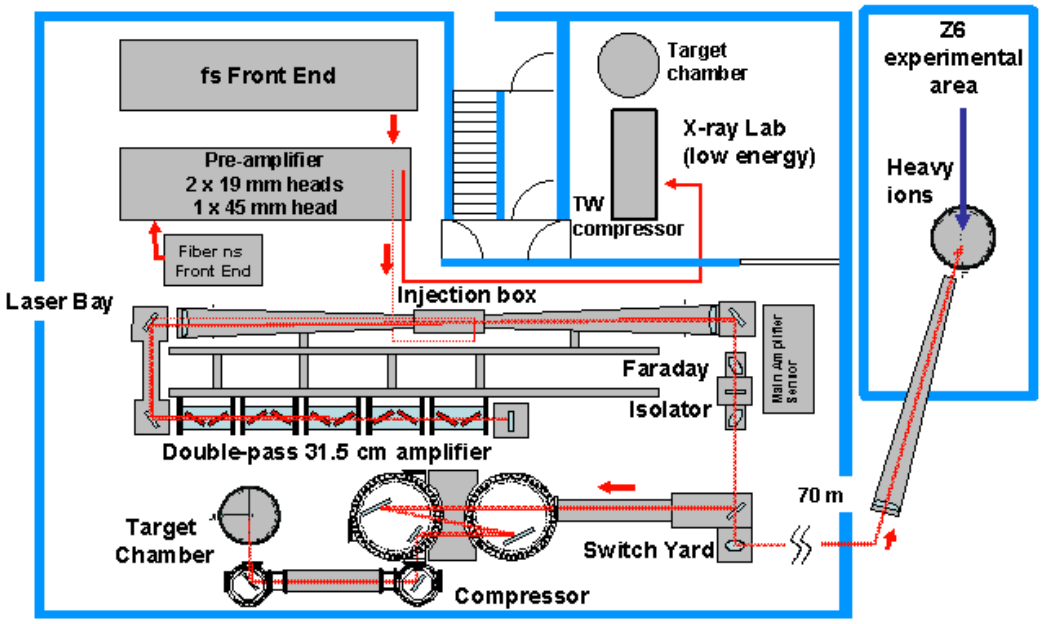

Figure 5.1: Overview of the PHELIX Laser System at GSI, Darmstadt, Germany. Three target chamber areas are shown. Experiments coupling the laser with the pulse power solenoid were performed in the Laser Bay (left) and in the Z6 experimental hall (right). Image courtesy of V. Bagnoud

cavity. The LIGHT project will not be the first project [91] to demonstrate injection, but the larger proton yield from PHELIX and the higher capture efficiencies of the pulse power solenoid look promising in making another significant advancement in High Energy Physics.

Helmholtz-Zentrum Dresden-Rossendorf, the Technische Universität Darmstadt (TUD), the Helmholtz-Institute Jena (HIJ), the Goethe University in Frankfurt and the GSI Helmholtz-Zentrum für Schwerionenforschung GmbH (GSI). The goal of the LIGHT project is to inject laser accelerated protons into an RF cavity for post-acceleration.

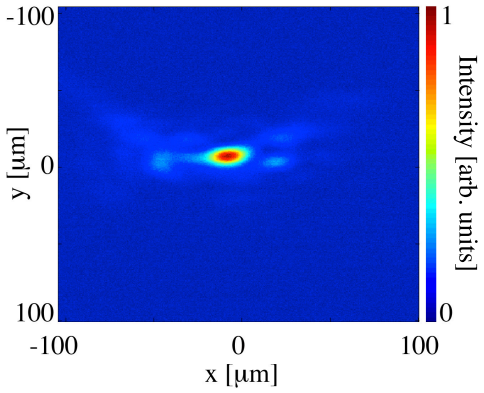

Figure 5.2: An example of the focal spot intensity distribution. At full-width half-maximum, the focal spot is 8.5 μm by 17 μm. This spot size contained 22% of the full laser energy, i.e. $\approx$ 16 J.

5.1 Proton Beam Capture and Transport

5.1.1 Experimental Set-up: PHELIX Laser Hall

The PHELIX laser system is well suited for beam transport experiments. The high per shot proton yields (up to 10^{13}) allow for ample protons to activate the dosimetric film after transport through the solenoid. Additionally, the PHELIX laser system can routinely generate proton energies above 20 MeV. These energies allowed us to demonstrate the large strength of the solenoid's field. As an example of typical laser characteristics, intensities of 2.9×10^{19} W/cm^2 were produced with 72 J of normal incident linearly polarized 1.054 μm laser light in 500 fs. The laser light was focused to an 8.5 μm by 17 μm diameter spot size (FWHM) on a flat 25 μm thick Au foil, and the spot size contained 22% of the laser energy.

The set-up of measurements at the PLH is shown in Figure 5.3. All dimensions, positioning and geometries of the solenoid are with respect to the windings and do not include the G-10 and other structural supports. The 150 mm long solenoid was positioned 95 mm from the 25 μm Au flat foil target. The Cu leads were positioned above the optical board with cylindrical plastic supports, and the current was passed from air to vacuum through four high voltage feed-throughs mounted on a 4 cm thick

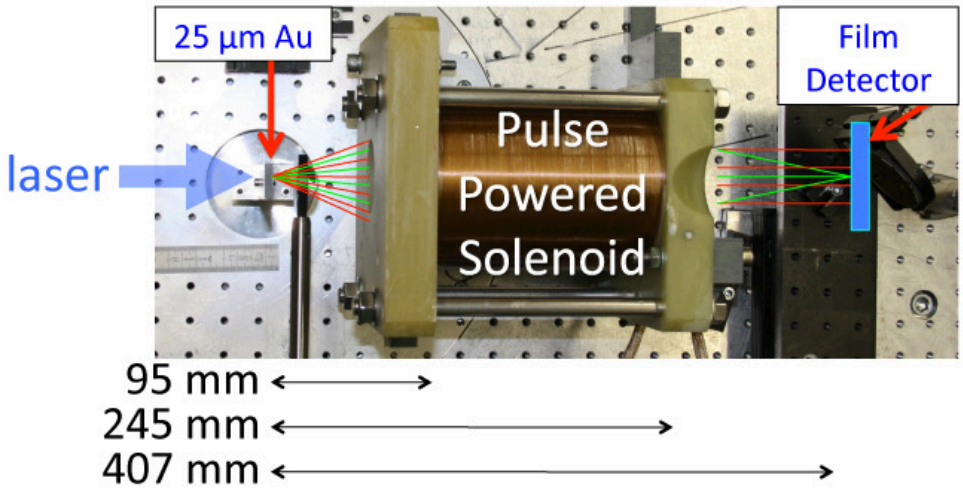

Figure 5.3: Photograph of the experimental set-up. From the left, 1.054 μm laser light is incident on a 25 μm Au flat foil target. The windings of the 150 mm long pulse power solenoid begin at 95 mm from the target. The dosimetric film stack is positioned at 407 mm from the target. The green and red lines illustrate the proton trajectories for low and medium energy protons, respectively.

PVC flange.

The pulser designed and built for this experiment suffered from voltage breakdown early in the experiment. This was an unfortunate consequence of a fast approaching beam-time and pressure to complete the pulser in the short timeframe. The only solution[2] to power the solenoid at this point was to use spare capacitors from the PHELIX laser system. The capacitors are located in the PHELIX capacitor bay which is conveniently located above the target chamber. The voltage was delivered through 10 high voltage cables connected in parallel. The rise-time of the field was 725 μs, Figure 5.4, and the laser was set to pulse at 350 μs after the capacitors were discharged. At this time, the magnetic field was at 80.6% of its maximum. The ratio of the magnetic field to the current driving the solenoid was 0.918 [T/kA], and the

[2]The work to quickly ready the spare PHELIX capacitors and high-voltage connections could not have been done without the skillful knowledge and help from the PHELIX crew. A special appreciation goes to Andreas Tauschwitz (GSI Plasma Physics), Momme Kreutz, Stefan Götte and Vincent Bagnoud.

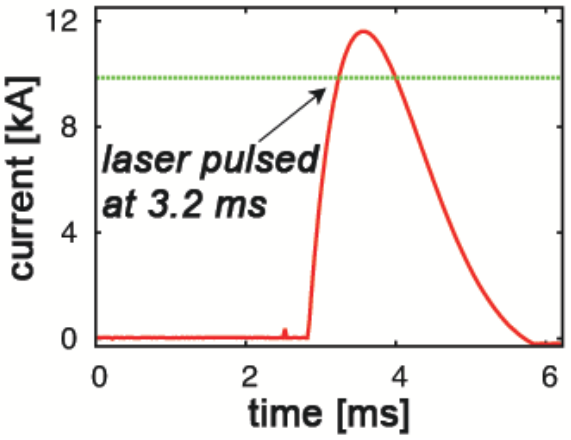

Figure 5.4: Plot of measured current through the solenoid as a function of time. The solenoid is pulsed at time t = 2.85 ms, and the laser is pulsed at t = 3.20 ms. The current at the time of the laser pulse is 9.25 kA ($B = 8.5$ T) as indicated by the green dashed line and can be considered static since the acceleration time is on the ps timescale and propagation time through the magnetic field is on the ns timescale.

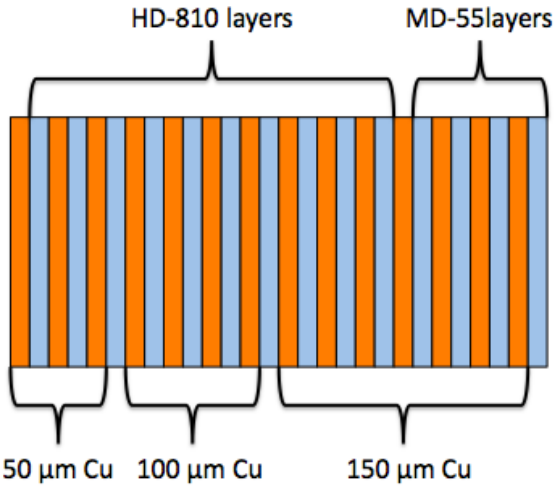

Figure 5.5: Dosimetric Film Stack. Layers of Cu were interlaced with layers of RadioChromic Film. The protons are incident from the left.

ratio of the current to the applied voltage was 0.973 [kA/kV].

5.1.2 Proton Beam Measurements

The protons were recorded using RadioChromic Film and copper foils, as illustrated in Figure 5.5. The copper foils had thicknesses ranging from 50 to 150 μm and were placed in front of each film layer. The first Cu foil stopped all protons with energies less than 3.7 MeV resulting in the low energy cut-off of the spectrum seen in Figure 2.9. A reference dosimetric film stack, Figure 5.6 (top), was placed at 32 mm from the target allowing for the spectrum in Figure 3.1 to be extracted. The proton beams were contained within a relatively uniform angular distribution with up to a

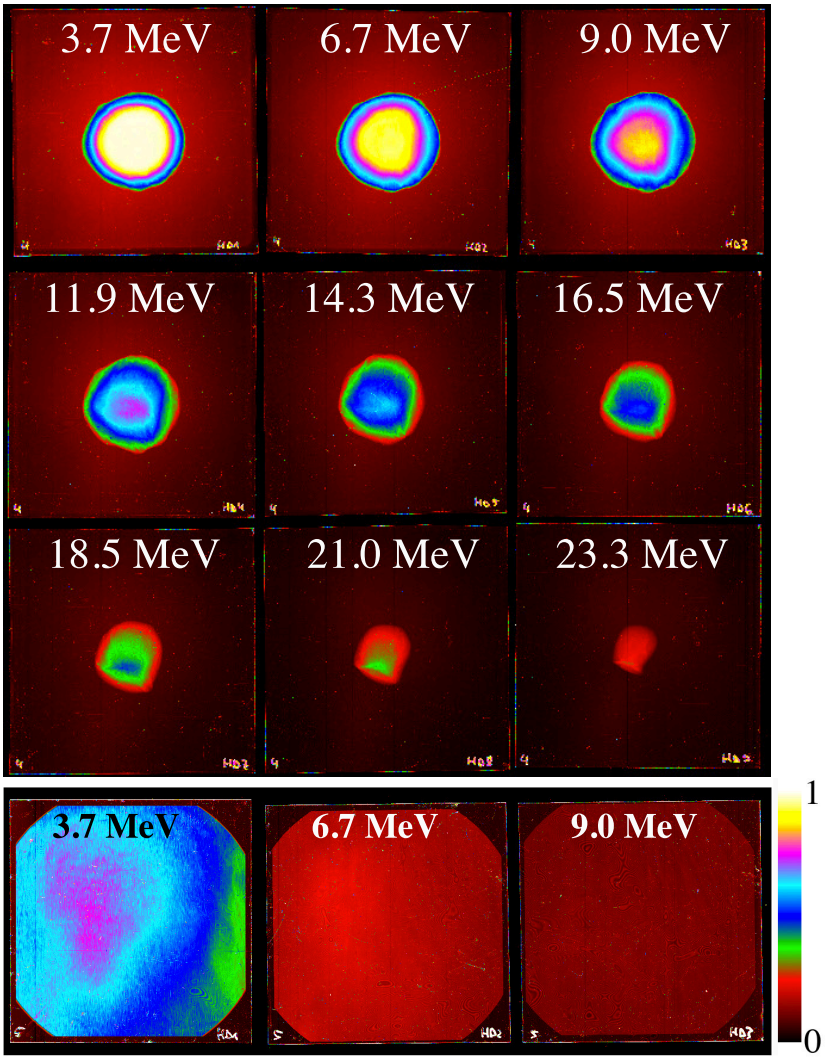

Figure 5.6: [Fase Color] Both top and bottom images are normalized to the linear color scale at the bottom right. **Top:** Color enhanced HD-810 RadioChromic Film reference shot. The film stack was positioned 32 mm form the target foil. **Bottom:** The first three irradiated HD-810 films positioned after the solenoid at 407 mm from the target foil. The solenoid field was set to zero, and its 48 mm bore acted as an aperture. The bore allowed for protons with a divergences $\leq 4.9°$ to pass through the solenoid as indicated by the circular distribution of dose.

half-angle divergence of 7° for high energy protons and 20° for low energy protons [Figure 2.8]. The acceleration process completed on the picosecond timescale, and the exponentially decaying proton spectra for this experiment had a maximum cutoff near 23 MeV. Integration over the experimental spectrum shows that 2×10^{12} protons with energies greater than 3.7 MeV were accelerated from the rear of the foil. A

second reference shot, Figure 5.6 (bottom), was taken with the film stack positioned at 407 mm from the target, i.e. after the solenoid. Four measurements are chosen to illustrate the capture and transport characteristics at 407 mm. Two measurements are presented in Figure 5.7 for a 7.2 T field and another two measurements are presented in Figure 5.8 for an 8.5 T field.

7.2 T Field

Two measurements are presented in Figure 5.7. The experimental characteristics for each shot are: 7.76 kA, 7.12 T and 81 J on target (top films) and 7.85 kA, 7.2 T and 77 J on target (bottom films). Comparison of the measurements shows a high degree of reproducibility, which will become important when this technology enters the application phase.

The 3.7 MeV protons were focused to a point between the solenoid and the film stack. The 6.7 MeV and 9.0 MeV protons were focused, but their focal spot was located behind the film stack. The 11.9 MeV protons were nearly collimated. The 14.3 MeV and higher protons had their divergences reduced, but not to the point of collimation or focusing.

The inhomogeneities of the dose distribution can be attributed to aberrations of the solenoid. The structures seen at the center of the films have been attributed to winding limitations as will be discussed later in Section 5.2. The less rigid, lower energy protons are affected by these higher order aberrations more than the rigid, higher energy protons. Effects of spherical aberrations that lead to limb brightening are also seen, most notably on the 6.7 MeV film layers and to a lesser extent on the 9.0 MeV film layers. These aberrations contribute to the emittance growth of the

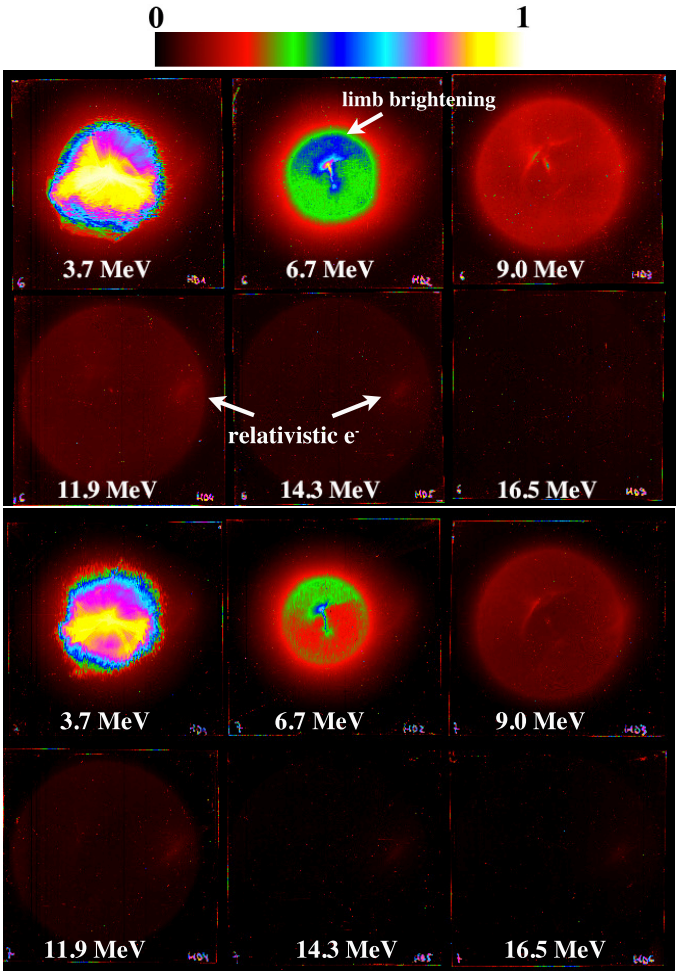

Figure 5.7: [**7.2 T**, Fase Color] Dosimetric film from 2 measurements: 81 J on target, 7.12 T (top) and 77 J on target, 7.2 T (bottom). Both images are normalized to the linear color scale at the top and show the first 6 films in the dosimetric film stack. The stack was placed at 407 mm behind the target foil. The film captured the 3.7 MeV protons as they diverged away from their focal spot. The 6.7 MeV films show limb brightening from spherical aberrations within the lens. The 6.7 MeV protons and, to a lesser extent, the 9.0 MeV protons were converging to their focal spot. The 11.9 and 14.3 MeV protons show a reduction in their divergence. The inhomogeneous distribution of dose is a result of spherical and higher order aberrations from the solenoid.

proton beam as discussed in Section 3.2.3. A uniform proton beam is one of the many requirements that a laser accelerated proton therapy system will need to meet. This is because non-uniformities in the proton beam will lead to an inhomogeneous dose distribution at the tumor sight. Typically, radiation therapy treatments are required

to have a dose variation of less than 5 to 10%.

8.5 T Field

The experimental characteristics for dosimetric films presented in Figure 5.8 are: 9.32 kA, 8.55 T and 72 J on target (top films) and 9.25 kA, 8.49 T and 70 J on target (bottom films). Comparison of the measurements again shows a high degree of reproducibility.

The protons follow the trajectories shown in Figure 3.3. The most notable feature is the recording of the 6.7 MeV protons very near their focal spot. Their FWHM is less than 2 mm and, including the shot-to-shot error in the proton yields, simulation indicates that the focal spot contained between 5.4×10^9 and 1.6×10^{10} protons with energies between 6.7 ± 0.1 MeV.

Figure 5.9 (A) shows the phase-space for all protons reaching this layer of film. The large butterfly shape is a result of the severe chromatic aberration. The 6.7 MeV protons are highlighted in green. As one can see from the phase-space plot, the dosimetric film was very near the beam waist for the 6.7 MeV protons. The slight rotation (clockwise from vertical) indicates that these protons posses a small divergence. Figure 5.9 (B) is a projection onto the x-axis of the phase-space plot of (A), integrated over θ, and takes into account the exponentially decaying spectrum. This resulting proton density distribution shows that most protons are concentrated on or near the axis at the position of the film stack.

What sets the pulse power solenoid apart from the alternative methods discussed in Section 3.3 is that the pulse power solenoid has high capture and transport efficiencies. Figure 5.10 presents the large capture efficiencies of the protons captured and

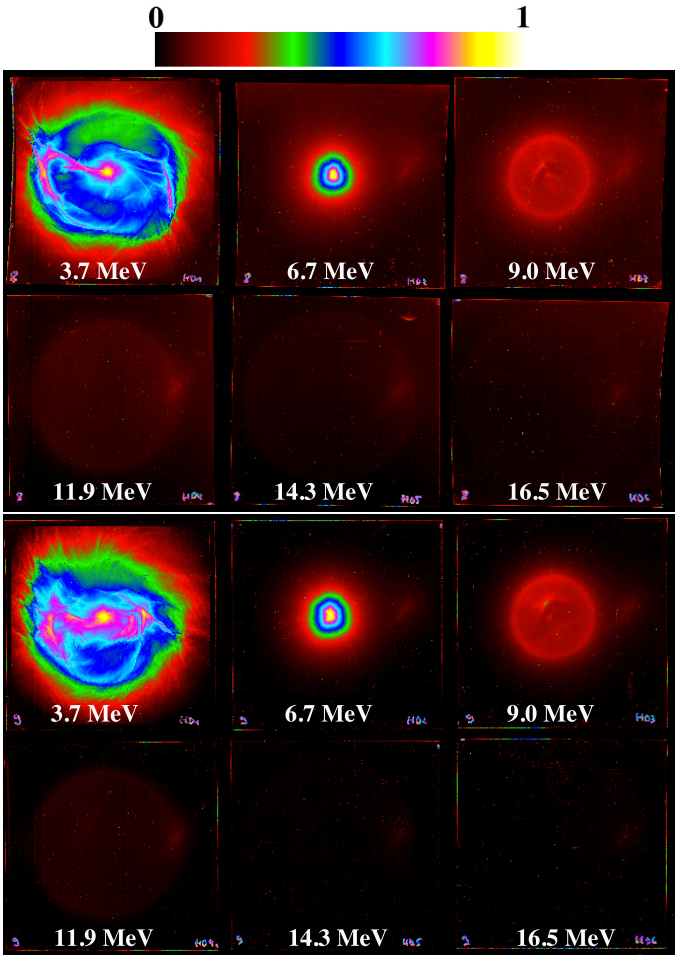

Figure 5.8: [**8.5 T**, Fase Color] Both images are normalized to the linear color scale at the top and show the first 6 films in the dosimetric film stack. The stack was placed at 407 mm behind the target foil. The film captured the 3.7 MeV protons as they diverged away from their focal spot. The 6.7 MeV focal spot was captured by the second film in each stack. Limb brightening can be seen in 9.0 MeV films. The 11.9 and 14.3 MeV protons were nearly collimated. The inhomogeneous distribution of dose is a result of higher order aberrations from the solenoid. Comparison of the top and bottom images shows the shot-to-shot reproducibility.

transported with the 8.5 T field. The minimum capture efficiency is 23% for the collimated 13.75 MeV protons. The less energetic protons have a lower rigidity and are more easily trapped in the magnetic field and result in capture efficiencies of 34% for the 3.7 MeV protons. Additionally, the more rigid, high energetic protons have lower divergence angles which results in capture efficiencies near 50%. As seen in Figure 5.10 the capture efficiency is at its minimum for the collimated portion of the beam.

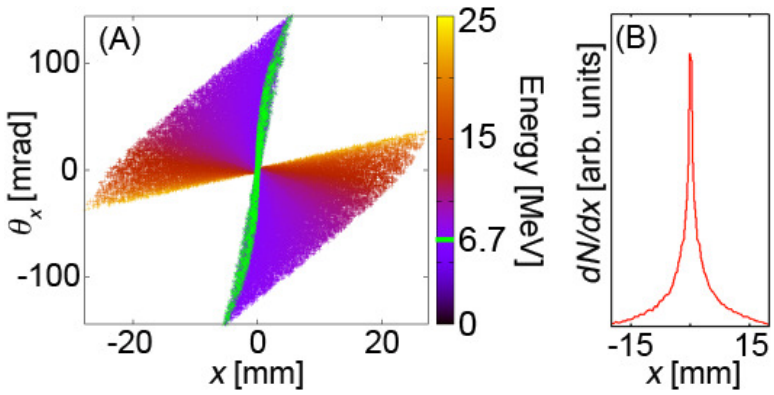

Figure 5.9: [Color Online] **(A)** Phase-space plot for all protons at or above 6.7 MeV for 8.5 T (i.e. protons incident on film layer #2 in Figure 5.8). The green points highlight the 6.7 MeV protons. **(B)** A projection of the entire phase-space plot onto the x-axis illustrates the proton density across the focal spot.

The higher capture efficiencies are associated with beams that are either focused (low energy protons) or still diverging (high energy protons). Until demonstration of the pulse power solenoid, the largest capture efficiencies were attributed to PMQ's and were near 3% for the collimation of 2.4 ± 0.1 MeV protons [7]. The pulse power solenoid is a factor of 7.7 more effective; nearly an order of magnitude.

An additional benefit of the pulse power solenoid is its ability to collimate a large energy spread which may become important in a future laser based medical therapy system. As seen at the bottom plot of Figure 5.10, 13.75 ± 1.25 MeV protons were collimated. This is 10.8% of the energy range in the proton spectrum. As discussed in Section 3.2.2, there are a limited number of protons accelerated by TNSA and a limited repetition rate of the laser. If TNSA scales to higher energies but the per-shot proton yield remains at the present level of 10^{13} per laser pulse, then laser accelerated proton therapy may need to rely on a single shot spread-out Bragg-peak (Figure 1.1) for dose deposition. The large collimated energy range will only benefit a future laser proton therapy system, and any unwanted parts of the spectrum can be trimmed away during beam transport.

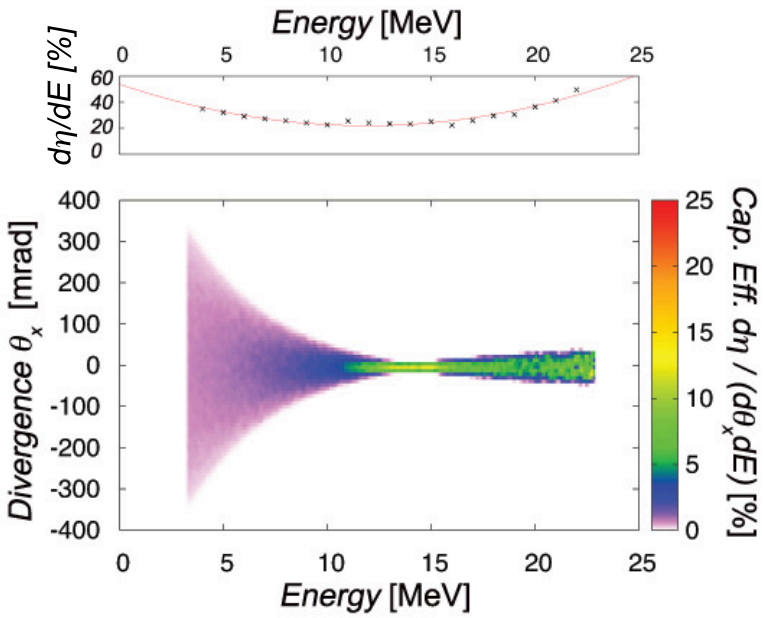

Figure 5.10: Divergence angles Θ_x of protons after passing through the 8.5 T field of the solenoid. The color density indicates the transport efficiency $d\eta/(d\Theta_x\ dE)$ for a single energy and single angle while the top is a projection showing the total transport efficiency $d\eta/dE$ for a single energy across all angles. As governed by the 8.5 T field, 13.75 MeV protons are collimated with near collimation of the 13.75 $\pm$ 1.25 MeV protons.

For application purposes, it is important to know how the spectrum looks after the solenoid. Protons of all energies pass through the solenoid, but they possess energy dependent divergences. Figure 5.11 illustrates the spectra after the solenoid for various angular envelopes. As the angular envelope is reduced, the proton spectra becomes dominated by the collimated protons and approaches that of a quasi-monoenergetic spectrum. The significance of this is the ability to use the pulse power solenoid as an energy filter, possibly with the need of an aperture, allowing only protons within a given energy range to propagate.

The two applications of proton therapy and post-acceleration will require a well controlled proton energy range and each will benefit from a low beam emittance. Analysis of the protons within the 1 mrad divergence envelop yields 1σ and 2σ emittances of

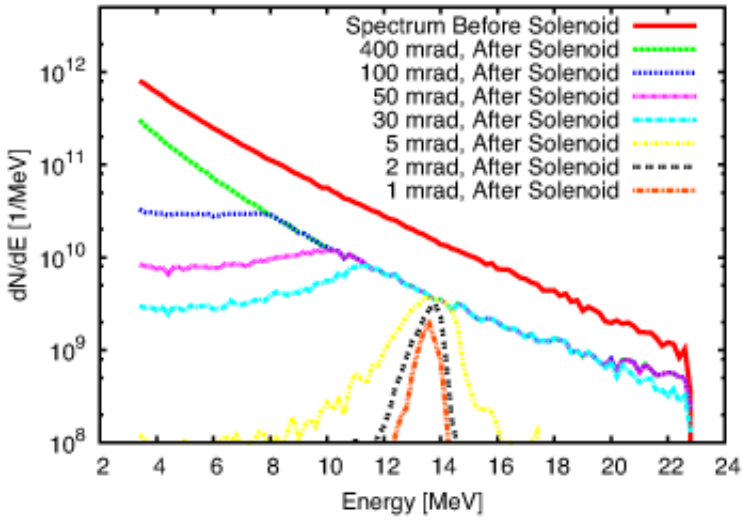

Figure 5.11: Proton spectra within various angular envelopes after the 8.5 T solenoid field. The 1σ and 2σ confidence band normalized emittances for the protons within 1 mrad are 2.5 and 10.2 π mm mrad.

2.5 and 10 π mm mrad, respectively. Integration over the 1 mrad spectrum indicates a yield of 1.7×10^9 protons.

5.2 Higher Order Aberrations

Noticeable structures, or inhomogeneities, were seen in the dosimetric films for measurements that included the magnetic field of the solenoid (Figures 5.7 and 5.8). Two hypotheses were considered to explain them. The first was attributed to the inhomogeneities in the laser focal spot being imprinted into the proton beam [49]. This did not explain the lack of structures in the reference measurements, but it could be argued that the focus varied from shot to shot such that the reference shot was made with a better focus. The second hypothesis, which was confirmed as correct via measurements, was that the solenoid possessed higher order aberrations.

What is meant here by higher order aberrations are magnetic field inhomogeneities

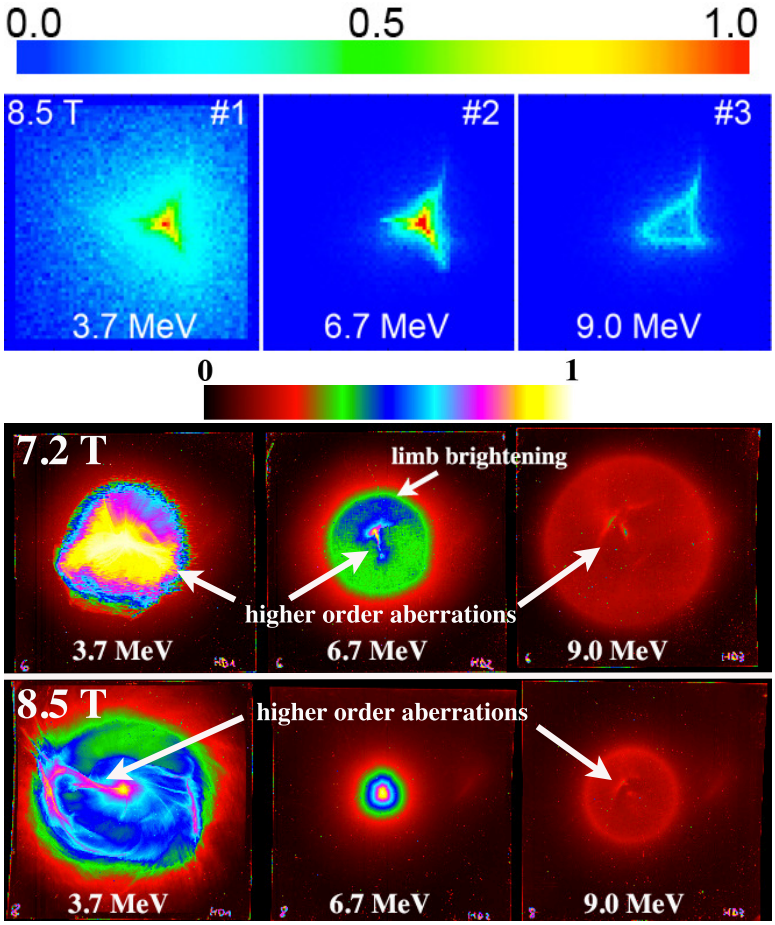

Figure 5.12: **Top:** Simulation of particle densities within dosimetric film layers illustrating the effect of higher order aberrations in a magnetic field. The simulation was meant to demonstrate the effect of non-symmetric magnetic fields and does not exactly replicate the geometry of the solenoid used in the experiment. **Bottom:** The first three films for 7.2 T and 8.5 T field strengths record the effect of the higher order aberrations from the pulse power solenoid.

resulting from non-ideal helical windings and their current-leads. Ideal solenoids are made of many concentric current loops. In reality, however, the current loops are replaced with a single wire helically wound. This helical winding adds a longitudinal current, and the "current rings" are more similar to tilted, longitudinally-advancing ellipses. When solenoids are constructed with multiple layers, like the solenoids presented in this work, the wire must not only move from a lower layer to a higher layer but also change directions. This forms partial Helmholtz loops at the entrance and

exit of the solenoid and leads to homogeneities within the magnetic field.

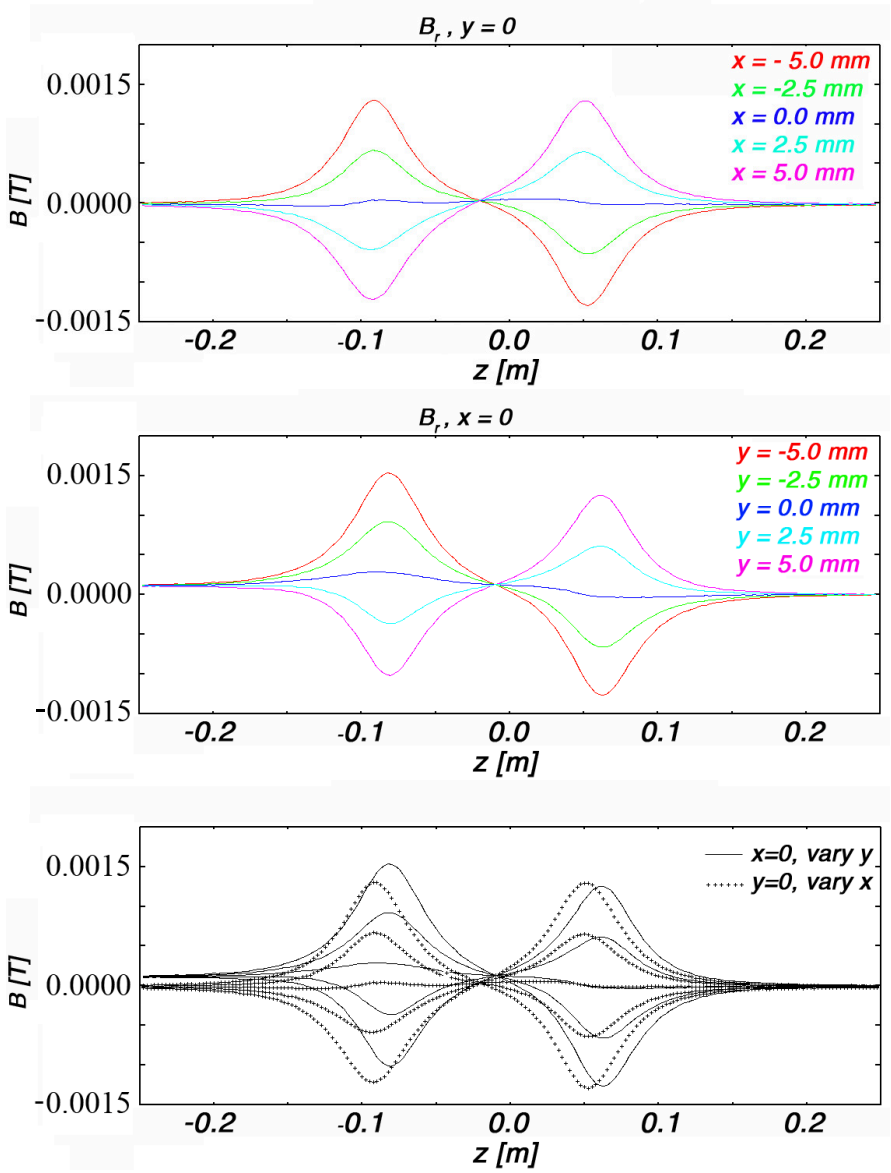

Figure 5.13: Radial Magnetic Field Measurements. Hall probe measurements in cartesian coordinates show inhomogeneities in the radial magnetic field. **Top** Vary x along z with y=0. **Middle** Vary y along z with x=0. **Bottom** Comparison of the top and middle measurements.

If severe enough, these higher order aberrations will alter a particle's trajectory. A simplified geometry was used to generate these aberrations in GPT. Four linear currents were places along side of each layer in the solenoid. This resulted in 16 linear currents in total. One of the four current line segments in each layer was offset longi-

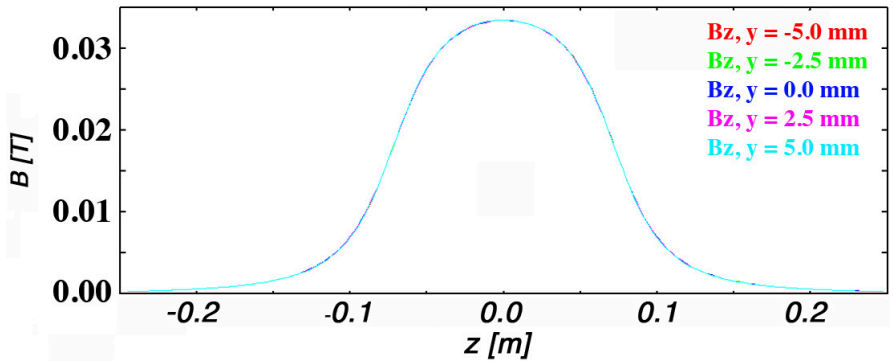

Figure 5.14: Measured longitudinal magnetic field for varying radial positions. Between -5 mm and 5 mm, there is no significant difference in B_z.

tudinally by 5 mm. These small perturbations to the magnetic field were enough to affect the proton trajectories and cause the aberrations seen in Figure 5.12.

Hall probe measurements using a DC current in the solenoid confirm the presence of magnetic field inhomogeneities. Ideally, the measurements of B_x and B_y would be equal across the axis, but this is not the case as seen in Figure 5.13. The fields across the axis differ by up to 0.6 mT (6 Gauss). The maximum longitudinal field strength B_z during the measurements was 0.034 T. Measurements of B_z were made for -5 mm $< x < 5$ mm and -5 mm $< y < 5$ mm, and since[3]

$$\frac{1}{r}\frac{d}{dr}(rB_r) + \frac{d}{dz}B_z = 0 \tag{5.1}$$

there should be a variation in B_z also. The variation in B_z for differing radial points within this range approached 0.1 mT (1 Gauss) and, due to the magnitude of the longitudinal field, is unnoticeable in Figure 5.14. The 6 Gauss variation of B_r leads to varying azimuthal proton velocities and varying focusing powers, Chapter 3. The variation, although slight, demonstrates the sensitivity that the radial component has on the focal power.

[3]From Maxwell's equations, $\nabla \cdot \mathbf{B} = 0$

The hypothesis, simulation and field measurements all suggested that higher order aberrations were responsible for the non-uniform proton distribution within the dosimetric films. For confirmation, measurements were again made by coupling the pulse power solenoid to the PHELIX laser system, this time at the Z6 experimental area. The power source described in Section 3.2.4 supplied the voltage to the solenoid, and this experiment used a luftspule (or air-solenoid) design, Figure 5.15.

This design separated the vacuum from the solenoid, allowing the solenoid and all its conducting wires to remain in air. As discussed in Section 3.2.7, the presence of air at or near standard pressure can increase the voltage breakdown limits by dampening charge cascades from triple-points and surface flash-overs. Simulations with COMSOL were used to understand how induced currents within the stainless steel housing would

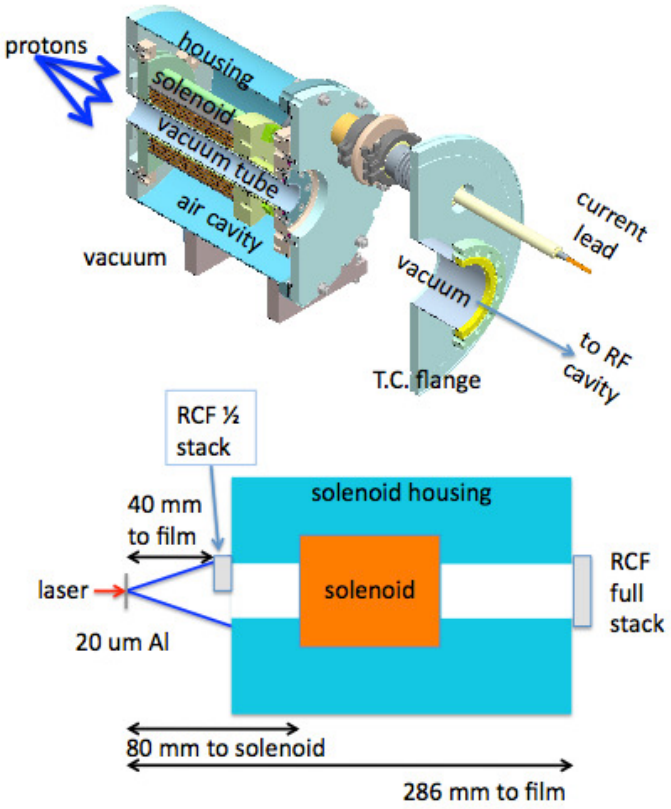

Figure 5.15: **Top** The encapsulated solenoid design for the Z6 target chamber. All conducting wires are separated from vacuum. The stainless steel housing is connected to the target chamber flange via two KF-40 bellows. The eddy currents induced in the stainless steel reduce the magnetic field strength by 6%. **Bottom** Schematic of the set-up inside the Z6 target chamber.

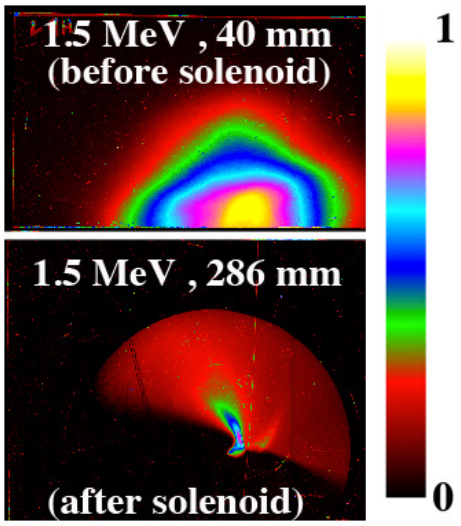

Figure 5.16: Two dosimetric films stacks record laser accelerated protons during a single laser shot in the Z6 target chamber. **Top** A half stack of film records half of the proton beam 40 mm before the solenoid. **Bottom** A full stack of film positioned 56 mm past the solenoid records the remainder of the proton beam. The higher order aberrations appear only after the protons are transported through the magnetic field.

affect the magnetic field. The stainless steel[4] has a low conductivity (near $\approx 2.3\%$ that of copper), and the simulations showed that the induced magnetic fields reduce the total magnetic field by 6%.

The target to solenoid distance was 80 mm. Two dosimetric film stacks were used simultaneously to deduce the origin of the structures on the dosimetric films. One film stack was cut in half and placed 40 mm from the target, i.e. 40 mm in front of the solenoid. The second film stack was placed at 286 mm, i.e. 56 mm after the solenoid. The results presented in Figure 5.16 clearly show that the higher-order aberrations from the solenoid field are responsible for the inhomogeneities within the proton beam. Before the solenoid, the proton beam is relatively smooth, but after the solenoid, it possesses an aberration.

In future applications, there will most likely be some drift space after the solenoid, so a demonstration of beam propagation becomes desirable. In the Z6 experimental hall, measurements were made at propagation distances of 880 mm past the target. The experimental set-up for these measurements is illustrated in Figure 5.17. The

[4]Steel type 1.4541: electrical resistivity $= 72 \times 10^{-8}$ Ω m. Typical copper: electrical resistivity $= 1.68 \times 10^{-8}$ Ω m.

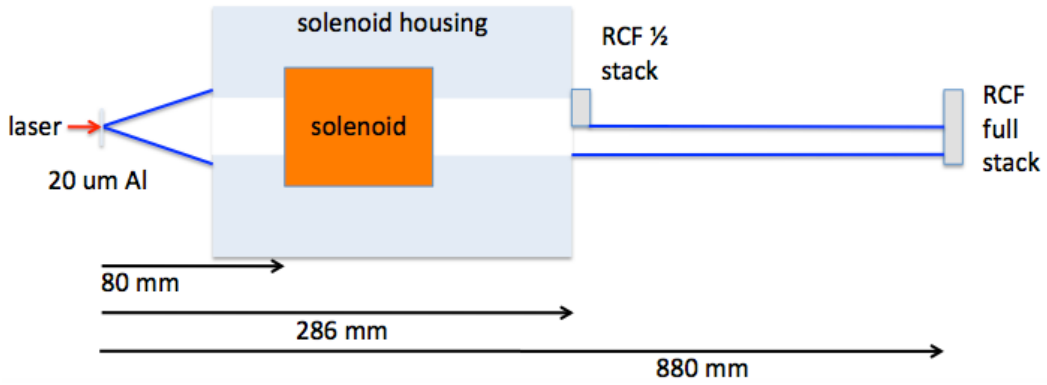

Figure 5.17: Set-up of the Z6 chamber for capturing and transporting laser accelerated protons to 880 mm past the 20μm flat foil target.

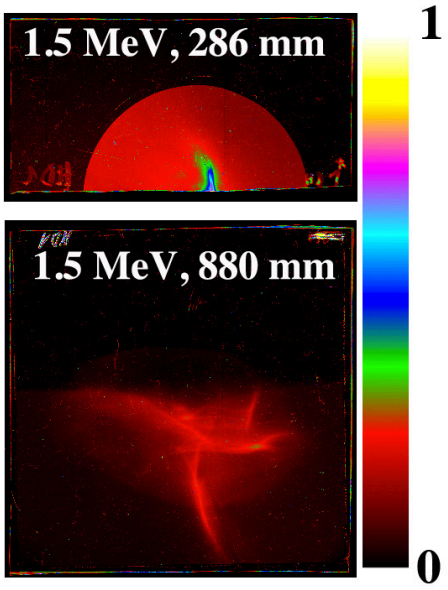

Figure 5.18: The first two dosimetric film layers from the 1/2-stack (top) and the full-stack (bottom) form the set-up shown in Figure 5.17.

target chamber is 0.5 meters in radius, so a beam pipe was attached to its walls to extend the available propagation distance.

Figure 5.18 shows the first dosimetric films from each of the two film stacks. Half of the proton beam is captured by the first film stack, and the rest of the proton beam travels downstream toward the second film stack. The demonstrated propagation to 880 mm past the flat foil target was an important step for both the LIGHT project and HZDR's laser-based proton therapy interests.

5.2.1 Emittance Growth

Beyond the aberrations discussed in Section 5.2, an important quantitative feature of the data are the well-defined spherical aberrations, which are evident as limb brightening in Figures 5.7, 5.8 and 5.12. The presence of spherical aberrations is useful for comparison of the experimental data to predictions from simulations. This in turn lends confidence to the particle tracking simulations, and allows us to infer an experimental limit on the proton beam emittance from these measurements. However to realize this, one must first extend the particle tracking simulations to include the full experimental response of the dosimetric film.

Dosimetric Film Response

A large amount of information can be extracted by the particle tracking program, and it was important to benchmark the simulations with measured data. This was done by adding a RadioChromic Film model to the package of computer simulation programs already mentioned. The full simulation now includes a proton source model

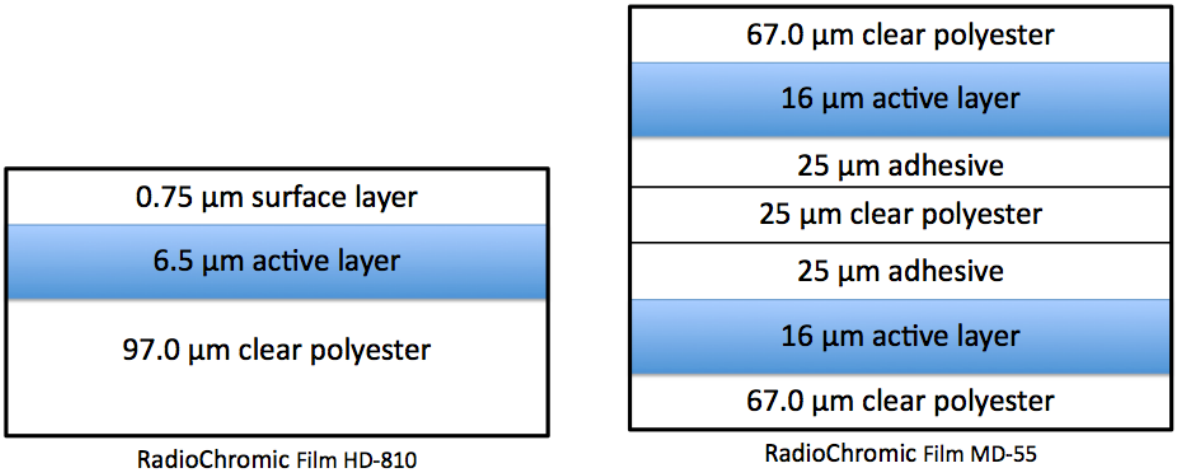

Figure 5.19: Schematic of HD-810 (left) and MD-55 (right) RadioChromic Film.

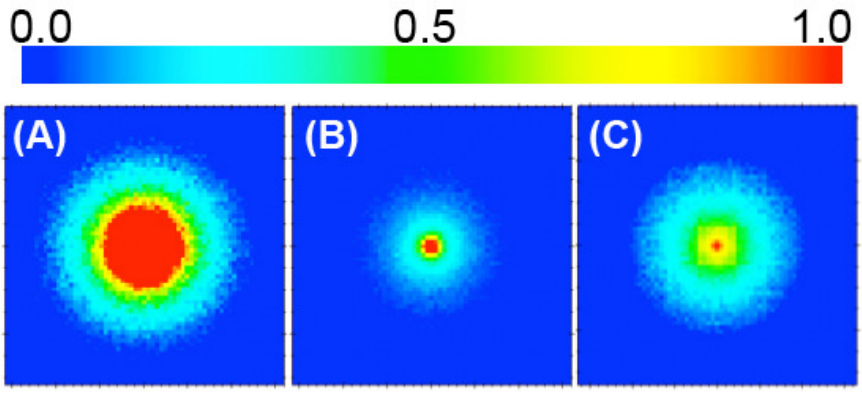

Figure 5.20: [Color Online, False Color, arbitrary units] Illustration of the generation of film response to protons from simulated data. **(A)** proton density in a simulated layer of film. **(B)** dose deposited from the protons in the left image. **(C)** final result after weighting the deposited dose with the optical density response of the film.

based on direct measurements, a magnetic field model based on a solenoids geometry, the inclusion of induced current effects, the accurate tracking of the protons with GPT and finally, the optical density response of the dosimetric film. It should be noted that this post-processing routine can be easily modified to provide simulation of dose deposition in a single layer of biological cells, thus providing simulation support for in-vitro cell irradiation experiments.

The two types of RadioChromic Film used in this work were HD-810 and MD-55. Illustrations in Figure 5.19 show the composite layers and thicknesses of each layer. The film is initially clear. After irradiation, the active layer will turn blue, and the optical density of the color change is dependent on the dose deposited in the active layer. There are differences between both films. The MD-55 has two active layers totaling 32 μm. This makes the MD-55 more sensitive than the HD-810 which only has a 6.5 μm thick active layer. This can lead to saturation of the MD-55 film if the dose is too large, so it is commonly placed after many HD-810 films where the dose is lower. Because the HD-810 film is about 104 μm thick while the MD-55 film is about 241 μm thick, the HD-810 films provide a finer energy resolution.

Using the screen element in GPT, the protons' trajectories and transverse positions are recorded at the positions of the dosimetric films. This results in the particle density plot shown in Figure 5.20 (A). A computer program [90] was previously developed to calculate the energy loss in RadioChromic Film types HD-810 and MD-55. It relies on the energy loss software SRIM (the Stopping and Range of Ions in Matter, [92]). It is used in this thesis work to generate files containing information about the energy loss within the active layer of the film.

Each proton is assigned a dose value for each active layer of dosimetric film as shown in Figure 5.20 (B). Now, the position of a proton in the film determines where its dose will be deposited, and the proton's momentum determines how much dose will be deposited. The result is a 2-dimensional dose deposition map with a 100×100 μm^2 grid resolution.

The correlation between the optical response and the dose deposition for RadioChromic Film types HD-810 and MD-55 were previously studied [48]. The response curves developed during this study were used to convert the 2-dimensional dose deposition map into a 2-dimensional optical density map, Figure 5.20 (C). This optical density map is a direct model of the active layer in the dosimetric film. The results are shown in Figure 5.21 for simulations using a 7.2 T field (top) and an 8.5 T field (bottom). Figure 5.21 shows that, with the exception of higher order aberrations, the simulation reproduces the data presented in Figures 5.7 and 5.8.

Limits on Emittance Growth

The spherical and chromatic aberrations have a direct effect on the emittance of the collimated proton beam. Earlier, Figure 3.7 showed the phase space of all protons

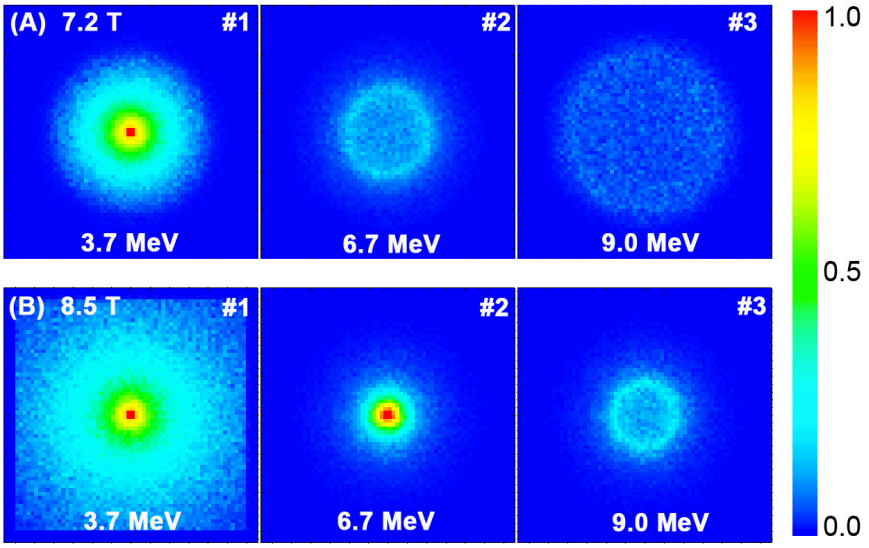

Figure 5.21: The first three layers of simulated HD-810 RadioChromic Film from protons tracked through 7.2 T and 8.5 T solenoid fields. As seen in the 7.2 T field (top three films), the intensity of the first film is highest, because it captured the most dose, while the third film captured the least. The second film shows an increased optical density around the circumference of the proton beam as a result of spherical aberration. This increased dose deposition is a direct result of the solenoid's spherical aberrations as discussed in Section 3.2.3. As seen in the 8.5 T field (bottom three films), the second film captured the near focus of the 6.7 MeV protons, while spherical aberrations are seen in the third film.

exiting an 8.5 T solenoid field. The colors correspond to the energy scale to the right and illustrate the dispersion generated by the solenoid. The magnitude of the chromatic aberration depends upon the geometry and field strength of the solenoid but also the energy range that is passed through the solenoid. Since the laser accelerated proton beam possesses a 100% energy spread, the aberration is significantly large. The chromatic emittance was found [6] to scale as,

$$\varepsilon = \alpha_c \Omega^2 \frac{\Delta E}{E} \tag{5.2}$$

where α_c is a geometric dependent constant, Ω is the maximum divergence angle and $\pm\Delta E/E$ is the ion energy range from which the transverse emittance ε is calculated.

The chromatic aberrations may be reduced with shorter length solenoids or with novel target geometries or new laser based accelerating techniques that yield near monochromatic proton beams.

The energy depended divergence angles were presented in Figure 5.10 and show that 13.75 ± 1.25 MeV protons are collimated. This collimated energy range is a direct effect of the spherical aberration caused by the varying focal powers as illustrated in Figure 3.5 from Section 3.2.3. The spherical aberration acting on a near monochromatic beam has the effect of "swirling" the phase-space ellipse, and Figures 3.7 (bottom) and 4.4 show this effect for 13.75 ± 0.1 MeV protons.

Since the spherical aberration is a result of the radial gradient of the axial magnetic field, future pulse power solenoids may benefit from new designs.

Chapter 6

Co-propagating Electrons

As discussed in Chapter 2, the laser accelerated protons co-propagate with electrons from the accelerating sheath. The electron-proton expansion is considered quasi-neutral, and the electron temperature cools as energy is transferred to the protons. A question arrises as to how the co-propagating electrons and the resulting space charge affect the capture and transport of protons by the solenoid lens. Does space charge affect the capture efficiencies or add an additional aberration due to electrostatic lensing?

Space charge simulations for the LIGHT project [95, 93, 94] at GSI were performed using the particle-in-cell code WARPrz [84] through a collaboration between the Technical University Darmstadt (TUD), Lawrence Berkeley National Laboratory (LBNL) and Lawrence Livermore National Laboratory (LLNL). The simulation contained 10^6 protons and the same number of co-propagating electrons. The results of the simulation are presented in Figure 6.1 and show an electrostatic lensing affect acting on the protons near the axis of the solenoid. Additionally, the capture efficiency

is shown to increase from 18.6% to 24.2% when the electrostatic Poisson self-field solver is enabled. This suggests that space-charge might be responsible for 30% of the transmitted protons.

6.1 Space Charge

One can predict a tight radius of curvature $r_{gyro} = mv_{\perp}/qB$ for the light electrons traveling in the magnetic field. Returning to the TNSA spectrum in Figure 2.9 with a proton energy range from 3.4 MeV to 23 MeV, the energy of the co-propagating electrons range from 1.9 keV to 12.5 keV. In an 8.5 T field, $r_{gyro} \leq 200\mu m$. There is some uncertainty of the WARPrz results, because the initial co-propagating electron population in the simulation possessed a temperature $T_e = 0$ keV.

Although the temperature of the electrons cool during the acceleration process, their final temperature in the expansion is not known. The addition of a temperature will

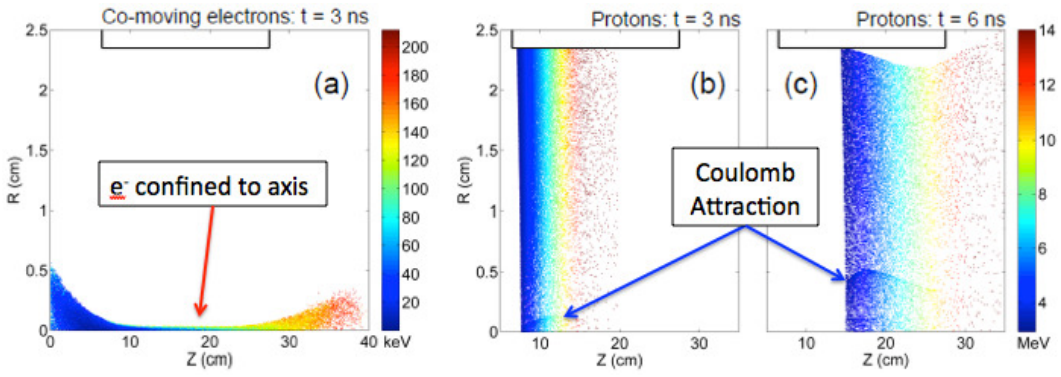

Figure 6.1: WARPrz simulations [93, 94] of electrons with $T_e = 0$ keV and protons with $T_p = 0$ keV propagating through an 8.5 T field of the first generation HZDR solenoid. In the three snapshots (a) through (c), the solenoid windings begin at z = 9.5 cm and end at 24.5 cm. **(a)** At time $t = 3$ ns, the electrons are tightly confined to a radius $r_{gyro} \leq 200\mu m$ on the axis of the solenoid. **(b)** The start of the electric lensing is seen at $t = 3$ ns. **(c)** At time $t = 6$ ns, the electric lensing effect is clearly acting on the protons near axis.

add additional velocity components to the individual electrons within the expansion. This becomes important when considering the capture efficiencies of the electrons. An electron's velocity parallel ($v_{\parallel}$) and perpendicular ($v_{\perp}$) to the solenoid's axis will dictate if the electron is transmitted through the solenoid or reflected away from the solenoid as indicated by,

$$\frac{v_{\parallel}}{v_{\perp}} > \sqrt{\frac{B_{max}}{B_{min}} - 1} \tag{6.1}$$

Here, B_{max} is the highest magnetic field strength of the solenoid and B_{min} is the magnetic field strength on axis and at the center on the solenoid. If the magnitude of the space charge of the electrons does indeed alter the capture efficiency of the protons, then adding a temperature to the electron population will need to be included in the simulation. The magnitude of the charge on axis is, therefore, in question for the results presented in Figure 6.1.

As discussed in Chapter 2, the electrons cool adiabatically by transfering their energy to the protons, but the co-propagating electron distribution function is unclear. For example, does the distribution function have the nature of an overlapping beam? Is it rather a plasma with a single temperature, or is it more complicated, such as a plasma with different radial and longitudinal temperatures. To answer this, quasi-neutrality measurements were performed at the PHELIX laser system. An accurate determination of the spatial charge distribution of the electrons and protons can lead

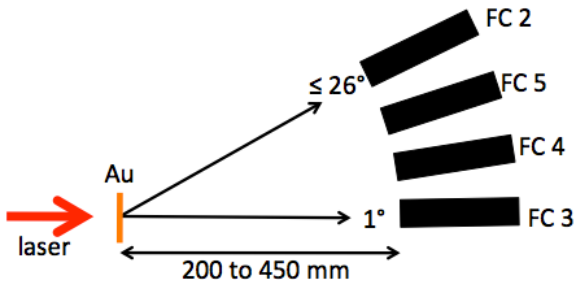

Figure 6.2: Schematic of the Faraday cup array. Four FCs were positioned between 1° and 26° off axis. The distance from the target to each FC in the array was equal and varied between 200 and 450 mm during the experiment.

to the determination of the Debye length and therefore the electron temperature. Miniature Faraday cups[1] were used in a collaboration between HZDR and the PALS Center in Prague, Czech Republic.

An LSP[2] simulation suggested that the energy transfer from the hot electrons to the accelerating protons ceased after 300 μm of the expansion's front. Additionally, the temperature at which the electrons decouple from the ions is of the order 200 keV. Using Faraday cups that were sensitive to either ions alone or ions and electrons, previous unpublished experiments[3] were performed with the LULI 100 TW Laser in August of 2003. Low energy electrons were stopped using thin foils, and the group estimated that 10 MeV protons from a 20 J, 300 fs laser pulse had co-propagating electrons with a mean energy of the order 50 to 100 keV. The difference between the

[1]The Faraday cups were designed and developed by D. Margarone, J. Prokůpek, and A.Velihan of the Department of Ultraintense Lasers, Division of High Power Systems/PALS Centre, Institute of Physics of the Czech Academy of Science, Czech Republic.

[2]Particle in Cell simulation - Large Scale Plasmas (LSP), R. Campbell, Sandia National Laboratory

[3]M. Cuneo, R. Campbell, T.E. Cowan, et al.

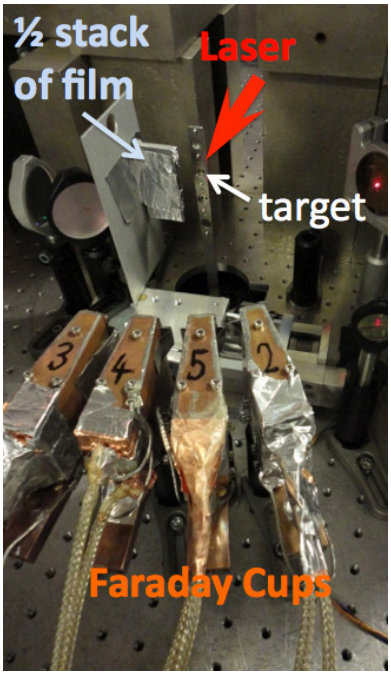

Figure 6.3: Image of the Faraday cups in the target chamber of the PHELIX laser hall. A half-stack of dosimetric film was placed in half of the beam path. Each of the four Cu housings (labeled 2 through 5) hold two Faraday cups each. Measurements were made on axis (0°) up to 24° off axis.

unpublished 2003 LULI experiment and the 2011 PHELIX experiment described in this section are newly designed miniature Faraday cups allowing for multiple radial measurements per laser shot. The 2011 experiment was capable of placing seven Faraday cups between 0° and 24°, allowing some Faraday cups to filter electrons with metallic foils while the others collected both electron and ion charges.

6.2 Experimental Set-up

A schematic of the Faraday cup array set-up is shown in Figure 6.2, and an image of the experiment is shown in Figure 6.3. One half of the radially symmetric proton beam was measured using dosimetric film positioned 60 mm from the target while the other half was measured using an array of Faraday cups positioned at 210 mm from the target. Up to seven Faraday cups could be operated at a given time. Two FCs are held in a single copper housing and separated by 15 mm. A 100 V bias was applied to each FC, and the opening of each FC could be adjusted from 0.5 mm to 2.0 mm. Flat foils of aluminum and gold were attached before the FC opening and used to absorb electrons below a given momentum. Using two 5 GS/s oscilloscopes, seven simultaneous measurements were made for each laser shot. With this sample rate, each channel could record a data point every 200 ps over a 20 μs time range.

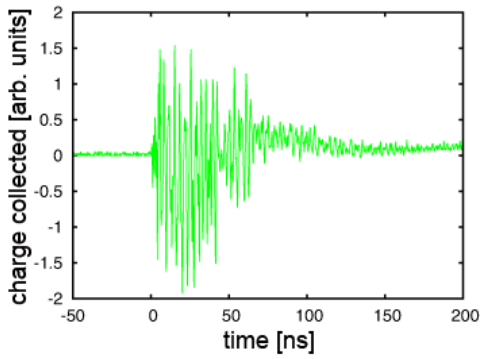

Figure 6.4: Original data from a Faraday cup placed 1° off-axis, 210 mm from the target. The large oscillations are a result of EMP from the laser-mater interaction.

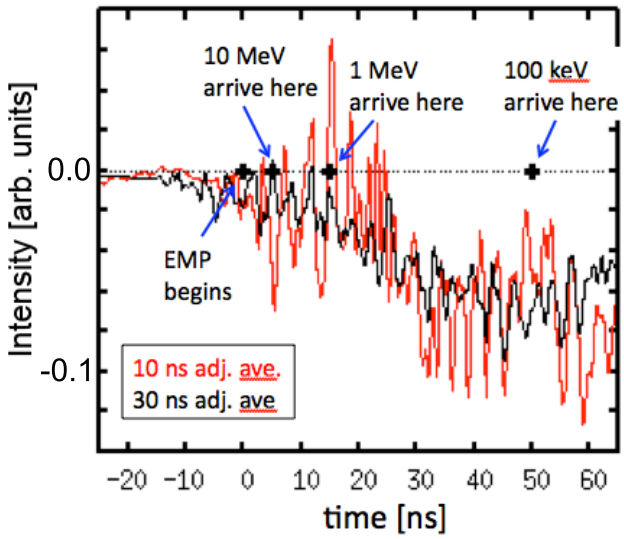

Figure 6.5: Adjacent averaging across 10 ns and 30 ns. Averaging over more data-points leads to a smoother curve but also a reduction of temporal resolution.

The Faraday cups were initially designed, developed and used on low power lasers ($I \approx 10^{15}$ W/cm^2). This experiment was the first to use them with a high power laser that generated far more EMP. Steps were taken to reduce the EMP within the FC circuitry. Both oscilloscopes were place inside a 5 mm thick copper Faraday cage, and tri-axial cables allowed for the outer conductor act as an eddy shielded. A specially manufactured vacuum flange kept the shield intact as the circuit passed from vacuum into air. Conductive metal tape was used to close any gaps between the Faraday Cage and the Faraday cups. The shielding capability was questionable at the FC collimator, i.e. where the charges enter the FC, and the power cable for the oscilloscopes and 100 V bias power supply. Although the power was sent through a transformer installed in the Faraday cage, the effect on the shielding is unknown.

6.3 Post-Measurement Signal Processing

The original signal, Figure 6.4, shows that EMP still affected the circuitry, and post-measurement signal processing was required. The signals were significantly smoothed using the techniques of adjacent averaging and high frequency filtering, but both techniques remove information from the dataset. Frequency cutting removes data that follows a given frequency, and adjacent averaging leads to a spreading of the measured signal and a reduction of temporal resolution. Both techniques eliminate sharp structures in the ploted curve.

Since one datapoint is recorded every 200 ps, using 51 and 151 datapoints averages the spectrum over a 10 and 30 ns timespan, respectively. The signal in the unprocessed data begins at $t = 0$, and as seen in Figure 6.5, the 30 ns average extends below $t = 0$ farther than the 10 ns average. This is unfortunate as the portion of the spectra we are most concerned with is in the 0 to 15 ns range (i.e. that affiliated with the > 1 MeV protons and their co-propagating electrons). Any details, such as rapid changes in the measured charge, are sure to be washed out.

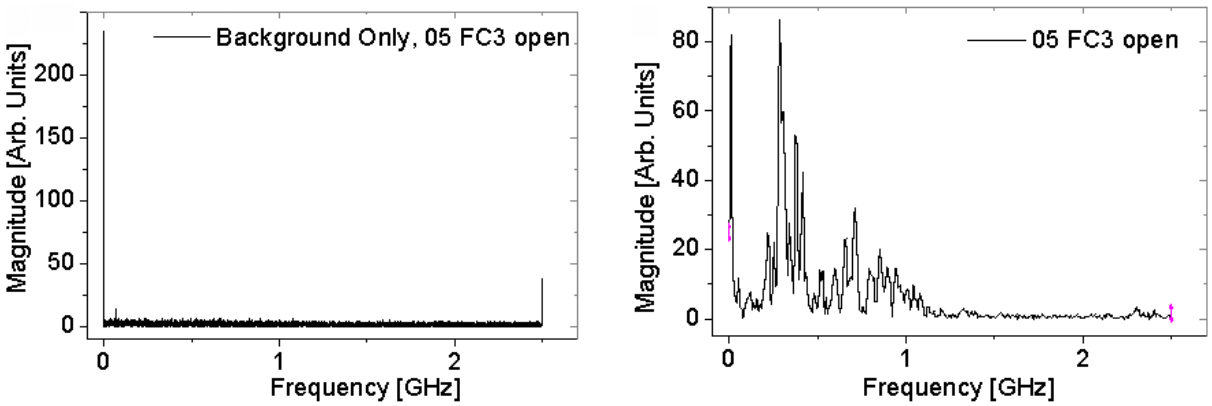

Figure 6.6: Frequency spectrum of the Faraday cup signal before the laser-matter interaction (left) and during/after the laser-matter interaction (right). This Faraday cup was positioned at 1° from the axis of propagation and did not use a foil filter.

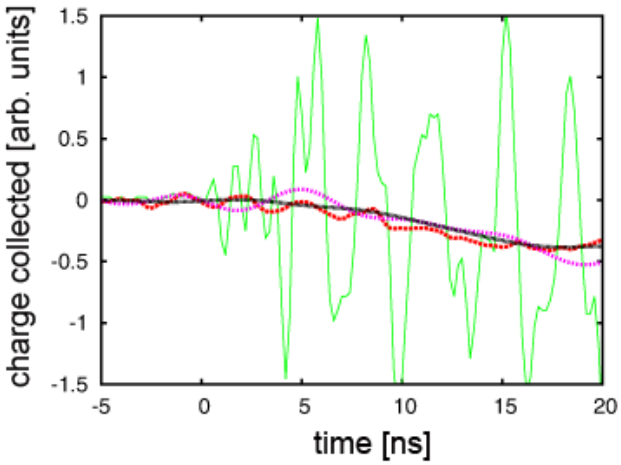

Figure 6.7: Faraday cup measurement. The green curve is the original data. The red curve was processed using and adjacent averaging technique with 51 datapoints (i.e. ±5 ns). The magenta curve was processed using a band block at 200 MHz and above. The black curve is a combination of both 51 point adjacent averaging and a frequency cut at 200 MHz and above.

The second smoothing technique used a post-measurement low-band pass filter. The measured spectra were converted from the time domain to the frequency domain using a Fast Fourier Transform[4]. Figure 6.6 shows the frequencies present in the FC circuit both before the laser-matter interaction (Left) and during/after the laser-matter interaction (Right). Band pass, band block and notch filtering were performed, but the removal of the major frequency peaks was not enough to smooth the final spectrum in the time domain. A smooth curve began to present itself only when frequencies at and above 200 MHz were cut. The final signal processing uses a combination of a 200 MHz frequency cut and a ±5 ns adjacent averaging, Figure 6.7.

Figure 6.8 shows an on-axis measurements for a single 78.4 J laser shot. The FC was 210 mm from the 10 μm flat gold foil target, and the half stack of dosimetric film indicates a maximum proton energy near 10 MeV, Figure 6.9. The largest electron and ion populations were measured near the axis. As seen in the 1° FC measurement,

[4]The Fast Fourier Transform was performed using the FFT signal processing routine in Origin Labs Pro.

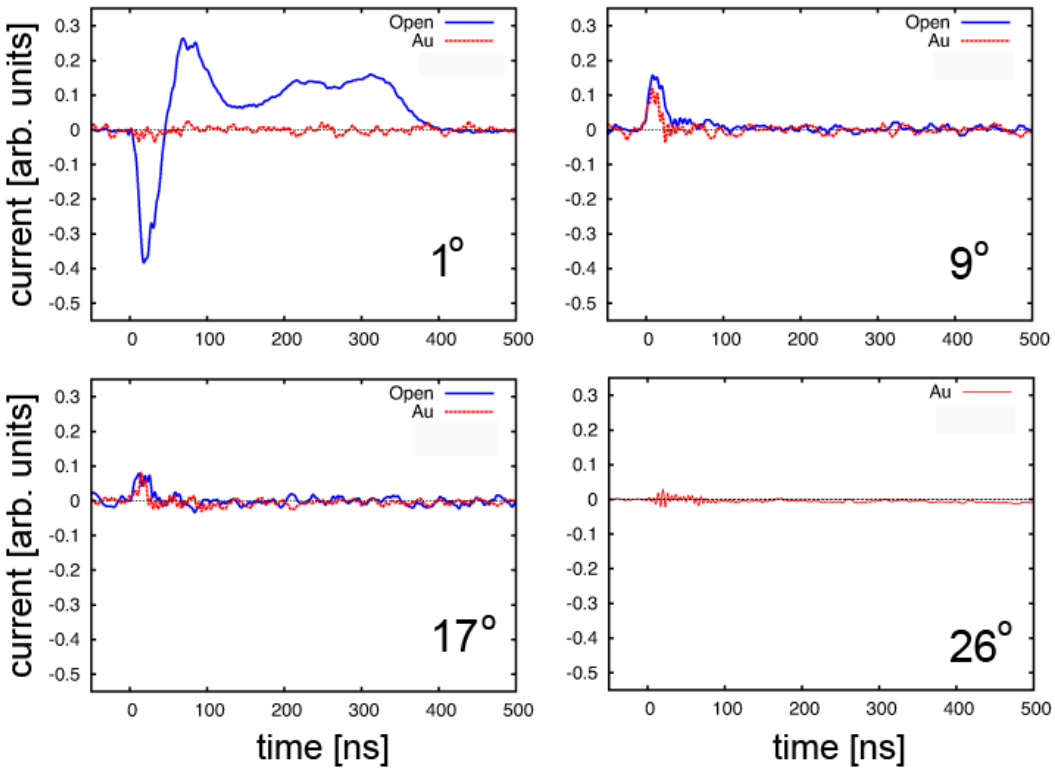

Figure 6.8: Measurement using 7 Faraday cups smoothed with a 5 ns adjacent averaging and a frequency cut above 200 MHz from a single laser shot. The red curves are measurements from Faraday cups with 1 μm Au foil filters. The blue curves are from Faraday cups without a foil filter. The Faraday cups were placed 210 mm from the target at 1°, 9°, 17° and 26° with respect to the target normal axis.

the expansion recorded by the open FC extends the entire range presented in the figure while the other FCs recorded much shorter expansions. The 9° and 17° FCs all measured positive charges, regardless of whether the 1 μm Au filter was used or not, but the 1° FC with Au foil shows no significant signal above the recorded background noise.

For the 1° with Au foil case, this flatness is surprising. According to the NIST stopping-power and range tables for protons (PSTAR[5]), a 250 keV proton has a range of 1 μm in gold. The time of flight between the target and FC for 250 keV protons is then 30 ns, however there is clearly no positive signal. NIST's ESTAR

[5]http://www.nist.gov/pml/data/star/index.cfm

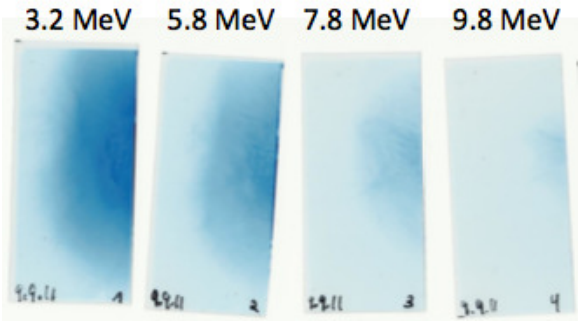

Figure 6.9: Dosimetric film half stack.

tables show that an 18 keV electron in gold will have a range of 1 μm, however, this uses a Continuous Slowing Down Approximation (CSDA) which accounts for the path length traveled and not necessarily the depth into the material that was traveled. The Monte Carlo Stopping and Ranges of Electrons in Matter (SREM) indicates that a 40 keV electron will be stopped in the 1 μm Au foil. The time of flight for 18 keV and 40 keV electrons would have been 2.7 ns and 1.9 ns respectively, so any signal from the more energetic electrons that pass through the FC is likely smoothed by the 200 MHz frequency cut (period of oscillation equals 5 ns) and the 10 ns adjacent averaging.

This still doesn't account for the lack of signal in this FC, regardless of it being positive or negative. Looking at the 1° FC without Au foil, there is a significant initial negative charge measurement followed by a long positive measurement. The two FCs at 9° and 17° recorded a positive signal from both the open FC and the FC with the 1 μm Au foil. It seems unreasonable that the 1 μm Au foil was just the right thickness and material to allow an exact amount of neutralizing electrons to enter the FC, but it is plausible that the 1° FC with Au foil was malfunctioning. Of the four laser shots that were measured, the 1° FC with foil recorded only an EMP signal, even for two shots that used a 2.5 μm Al foil.

The goal of this experiment was to extract an electron temperature during the early expansion. Unfortunately, with the loss of two days (40% of the setup and beam time), we were unable to improve the shielding. We instead measured the late hydrodynamic expansion. Without further reduction of EMP, the Faraday cups may not be useful, and other measurement techniques will be required.

Chapter 7

Future Prospects in Therapy

This section of the thesis concentrates on the future prospects of laser-based cancer therapy. Here, it is assumed that the scaling in Chapter 2 will someday result in 250 MeV protons, and that the spectrum will look like the scaled TNSA spectrum presented in Figure 3.1. It is also assumed that a pulse power solenoid and its accompanying pulse power magnets will offer high optical qualities, high mechanical strengths and operate at high repetition rates.

These challenges will need to be addressed in the future, but from the information presented in the earlier parts of this thesis, one can begin to understand the feasibility of using a laser accelerator coupled to a pulse power beam transport system. Of particular interest is what the spectrum will look like after beam transport around a patient. Although this information will not prove that a pulse power gantry will work, it gives us an idea of its strengths and limitations.

7.0.1 Achromatic Pulse Power Beam Transport

By expanding on the particle tracking simulations presented in Chapter 3, the full potential of high repetition rate pulse power magnets begins to emerge. The feasibility of beam transport through a simulated pulse power gantry was studied, and two principle assumptions were made. First, it was assumed that a scaled TNSA spectrum will be achievable with a maximum proton energy of 250 MeV and the currently achievable 2×10^{12} protons per pulse (Figure 3.1, red dashed line). The second assumption is that sufficiently high quality air-core pulse quadrupoles (up to 400 T/m over 5 cm) and pulse dipoles can be developed and pulsed with the laser repetition rate. Additionally, the solenoid remains as the initial capture and collimating element. The geometric properties of the solenoid remain unchanged and the field was scaled to 32 T.

The aim of the gantry design was to transport a broad energy range to include the possibility of using a single-shot spread-out-Bragg-peak; the reason being that the laser's repetition rate and accelerated proton numbers are presently predicted to be limited. A sufficient momentum spread and precise control over spectral shaping will be required in order to shape the dose deposited by a single-shot SOBP. The maximum achievable momentum spread will be dictated by dispersive effects as the beam passes through dipole fields, like those of a sector magnet. The dispersion causes a spatial separation of the proton beam into components of different energies. This may benefit spectral shaping via mechanical collimators, but it poses challenges for beam transport. Upon exiting a dipole field, each momentum component of the beam will have a slightly different trajectory than the next. This, however, can be controlled to a large extent by correcting the dispersion from one dispersive element

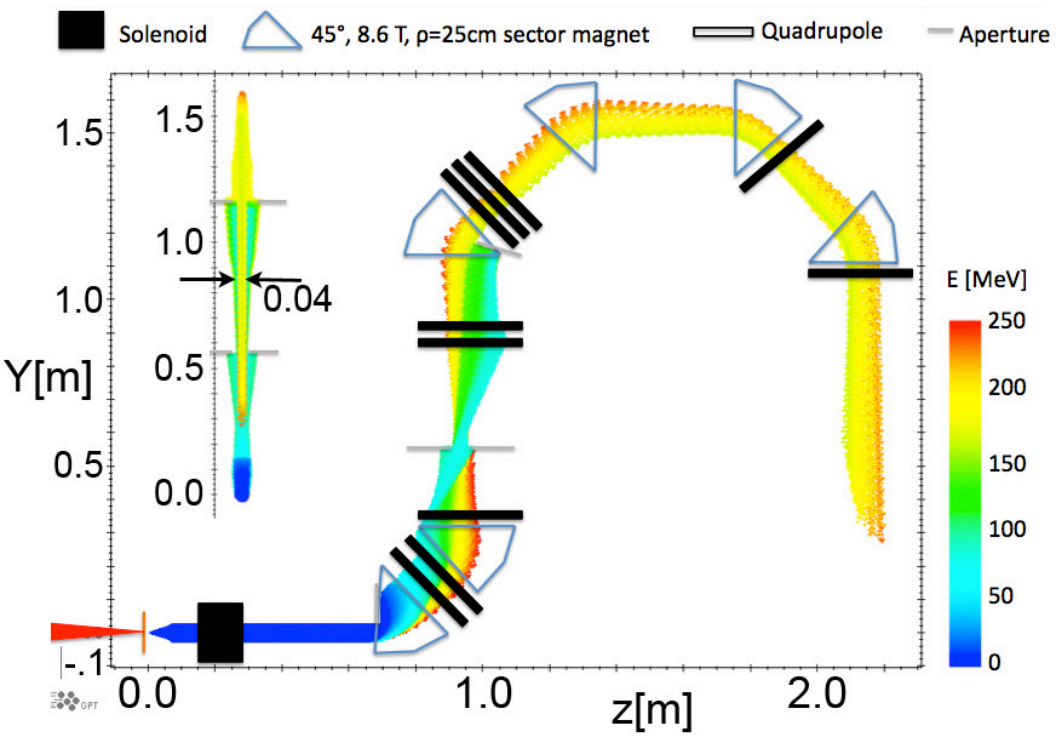

Figure 7.1: A proposed pulse power gantry concept for the transport of laser accelerated protons.

(like a sector magnet) with other dispersive elements (like quadrupole doublets or triplets) [96].

A simulated concept of the pulse power gantry is presented in Figure 7.1. The quadrupole fields used to correct the dispersion have reasonable strengths, and the dipole fields are 8.6 T and accommodate a central bending radius near 25 cm. The colors in Figure 7.1 indicate the beam's proton energies as labeled by the scale and illustrate the dispersion effects. As seen in the gantry design, most sector magnets are directly followed by at least one quadrupole. The hight that the proton beam reaches is 1.5 meters. If the magnets, structural supports and spectral shaping mechanisms do not add significantly to the overall size of the gantry, then the compactness alone offers a significant financial advantage over present day ion therapy gantries.

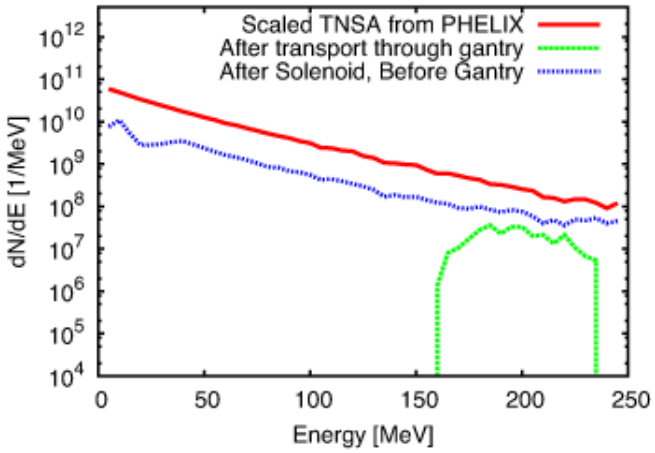

Figure 7.2: The available spectrum after protons accelerated by a single laser shot are transported through the gantry in Figure 7.1.

7.0.2 Proton Spectrum After Beam Transport

The spectra before the solenoid, at the exit of the solenoid and after the gantry are presented in Figure 7.2. The large energy spread from 160 MeV to 235 MeV after transport through the gantry suggests that a single-shot SOBP may be possible. The transport efficiency through the gantry for the central energy of 197.5 MeV is 43% which may be improved through further beam transport optimization. How useful this proton beam will be is another question. As seen in Figure 7.1, the proton beam exits the last magnet with a large energy dependent spatial spread. Future feasibility studies can determine if a dose deposition routine can be developed from such a beam.

Placing a final focusing element at the exit port becomes challenging because the beam is broad with a large energy spread. The idea of the SOBP is to spread the dose longitudinally across some depth range while scanning in the transverse directions. Since the beam at the exit port has a large diameter, it may be possible, or necessary, to deposit the dose across transverse areas of a tumor while scanning in

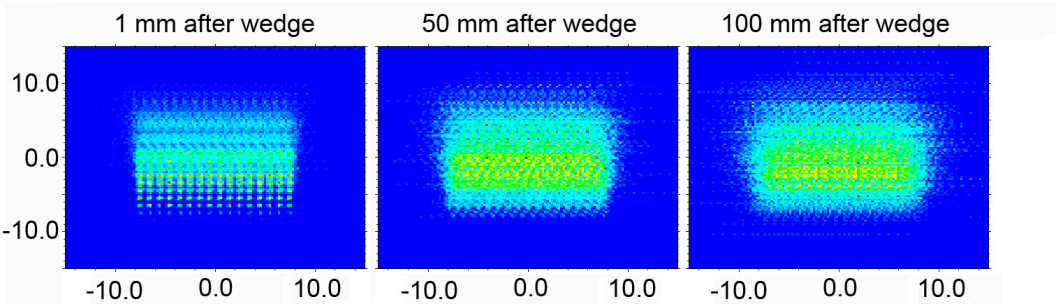

Figure 7.3: The effects of straggle and scatter from a Be wedge used to narrow the energy spread in the proton beam exiting the gantry in Figure 7.1.

the longitudinal direction. This would require a uniform monochromatic beam that can be shaped in its transverse planes.

The energy spectrum exiting the gantry can approach a monochromatic spectrum by degrading the energy of the faster protons. This can be accomplished by placing a wedge at the exit port. Since GPT does not account for the interaction of ions in matter, the angles of scatter, transmitted energies and longitudinal and lateral straggle lengths were extracted from SRIM for a Be wedge placed at the exit port of the gantry. The wedge thickness was set such that the proton energies would be nearly uniform after they exit the Be degrader. The full-width half-max after the wedge was 2 MeV centered around 150 MeV. One side effect was that the lateral straggle and angles of scatter introduced a spread in the final beam, Figure 7.3. Further studies of dose deposition routines will be able to quantify the usefulness of such a beam. Generally speaking, such a spread will increase the lateral dose penumbra at the tumor site. It may be that a wedge along with a final focusing element will offer better performance, but it should be noted that if an energy degrader is used, then the effects of activating its material need to be studied. Additionally, because the energies are reduced after the wedge, the laser must accelerate greater energies and the pulse magnets will need to produce stronger fields.

7.0.3 Coupling to Conventional Accelerators

By storing the energy in a capacitor and releasing the current in temporally short pulses, pulse power optics can operate at high field strengths and with less heating than their DC counterparts. The fact that the beam transport system is pulsed is of little concern when coupled to a pulsed laser accelerator. The scaling laws suggest that lasers will someday provide 250 MeV protons, but this does not mean that the conventional accelerators will become archaic and old technology.

The present cyclotron designs provide a 250 MeV proton accelerating source that is smaller than the present day laser accelerators. For example, the superconducting 250 MeV proton cyclotron at the Paul Scherrer Institute (PSI) in Switzerland has a compact diameter of 3 meters. Some cyclotrons can offer a large high-frequency AC (near continuous) current (up to 1.5 μA [97]) which, when coupled to a pulse power gantry, may offer enough protons per gantry pulse to treat a patient within a reasonable time. The problem here, however, will be frequency matching. If one considers using a kicker magnet to steer the beam into the gantry, then when the kicker magnet is off, the beam will need to go to a beam dump or storage ring. Such a high current and high energy proton beam would surely cause activation and temperature increases in a beam dump.

Other considerations are synchrotrons that can operate a low frequencies, e.g. 25 to 60 Hz [98]. Although synchrotrons are not compact, coupling them to pulse power gantries may offer a cheaper alternative to the present day DC gantries. Technologies like Fixed-Field Alternating-Gradient (FFAG) accelerators offer a continuous current like a cyclotron and an inexpensive storage ring like a synchrotron. The beam extraction system of the 150 MeV KEK FFAG in Ibaraki, Japan [99] consists of a 250

Hz kicker magnet. If such an accelerator with 250 MeV protons were coupled to a pulse power gantry, it may prove successful in reducing the costs and sizes of proton therapy clinics. The 150 MeV KEK FFAG has a 100 nA current. Assuming that a bunch length of 10's of nanoseconds is extracted at 100 Hz and sent through a 100 Hz pulse power gantry, there would be 6.24×10^9 protons per pulse. Proton therapy, generally speaking, requires 1.0×10^{12} protons in total leading to a total treatment time of 0.03 minutes. Therefore, the dose rate is too high, and the current or bunch length would need to be reduced. In either case, development of a pulse power gantry for conventional accelerators seems promising and should be pursued.

7.0.4 Alternative Proposals for Inexpensive Proton Therapy

The motivation to produce compact and inexpensive proton therapy systems is stimulating novel and creative designs that do not necessarily rely on laser accelerators. Since conventional cyclotrons are becoming smaller in size, some research groups are suggesting that the accelerator itself can be rotated around the patient. The Still-River Company proposed mounting a compact cyclotron to a rotating structural support, Figure 7.4 (A), and Varian is working on a rotatable and compact synchrocyclotron design, Figure 7.4 (B). Designs like these will still need to be housed in a large building, but the beam line and transport systems would be significantly reduced compared with present day proton therapy beam lines.

Some research shows that 100 MeV/m high gradient linear accelerators may be possible [100]. These accelerators are called Dielectric Wall Accelerators (DWA) and are alluring. To date, the high gradients have only been produced over short lengths, and how they can be scaled to longer acceleration lengths is at this point unknown. If this

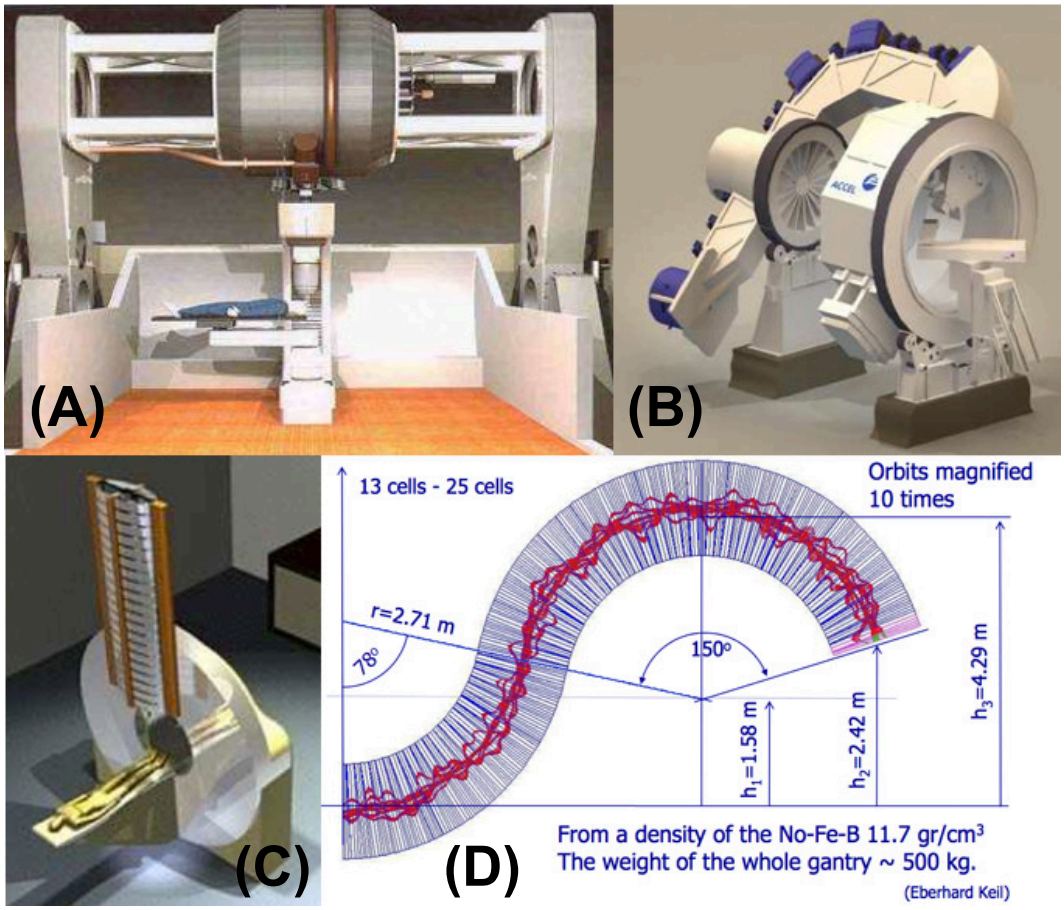

Figure 7.4: Alternative concept for compact and cost effective proton therapy. (A) rotating compact cyclotron, Still-River Company. (B) rotating compact synchrocyclotron, Varian. (C) Dielectric Wall Accelerator [100] and (D) Permanent magnet gantry [101].

technology becomes scalable, it is conceivable that a 2.5 m LINAC can be placed on a rotating support, Figure 7.4 (C), thus delivering high energy protons at any given angle for what is likely to be a very inexpensive cost.

Another novel design comes in the form of a compact permanent magnet gantry, Figure 7.4 (D). Although permanent magnets were shown to be extremely weak for capture and transport of laser accelerated protons, they have proved promising via simulation in an FFAG configuration [101]. The simulations indicate that ion energies between 68 and 400 MeV/n can be transported through the permanent magnet gantry.

As seen in Figure 7.4, the design is under 5 m in height which is still quite large, but the permanent magnet portion of the gantry only weighs 500 kg.

It should be noted that if the source can be rotated around the patient, then is seems reasonable to ask why the patient can not be rotated around the source. Although this seems like the least expensive solution, most anatomy would shift within the body as it is rotated.

Chapter 8

Appendix

8.1 Appendix: Ion Energy Loss in Matter

As described by the Bethe formula, a proton's energy is primarily lost through Coulomb interactions with outer shell electrons. Its energy loss follows [102],

$$-\frac{dE}{dx} = Kz^2\frac{Z_t}{A}\frac{1}{\beta^2}\left[\frac{1}{2}ln(\frac{2m_ec^2\beta^2\gamma^2T_{max}}{I^2}) - \beta^2 - \frac{\delta(\beta\gamma)}{2}\right] \tag{8.1}$$

where

$$T_{max} = \frac{2m_ec^2\beta^2\gamma^2}{1 + 2\gamma m_e/m_p + (m_e/m_p)^2} \tag{8.2}$$

is the maximum energy transferred to a free electron.

E = energy of the proton

x = distance in target travelled by the proton

γ = Lorentz factor

β = normalized velocity of the proton

T = proton energy

Z_t = atomic number of target material

ze=charge of incident particle

e = charge of electron

A = atomic mass of target material

r_e = classical electron radius

m_e = electron mass

m_p = proton mass

n = electron density of target

I = mean excitation potential

$K = 4\pi N_A r_e^2 m_e c^2$

N_A = Avogadro's number

ϵ_0 = vacuum permittivity

Reducing this equation to a more simpler form shows that $-dE/dx \propto Ln(\beta^2)/\beta^2$, i.e. the energy loss becomes greater as the particle slows.

8.2 Appendix: Ponderomotive Force

This Appendix section details the force acting on an electron in a linearly polarized plane wave,

$$\mathbf{E} = \mathbf{E}_0 sin(wt) \tag{8.3}$$

The force acting on the electron is,

$$\mathbf{F}_p = m_e \frac{d\mathbf{v}_p}{dt} = e\mathbf{E}_0 sin(wt) \tag{8.4}$$

where the velocity is periodic and given by,

$$\mathbf{v}_p = \frac{-e\mathbf{E}_0}{m_e w} cos(wt) \tag{8.5}$$

As discussed in Chapter 2, one expects an electron in this field to gain a drift velocity $\mathbf{v}_d << \mathbf{v}_p$. To find the drift force $\mathbf{F}_d$, one first rewrites $d\mathbf{v}/dt$ as,

$$\begin{aligned} \frac{d\mathbf{v}}{dt} &= \frac{\partial \mathbf{v}}{\partial t} + \bigtriangledown \mathbf{v} \cdot \frac{\partial \mathbf{r}}{\partial t} \\ &= \frac{\partial \mathbf{v}}{\partial t} + \mathbf{v} \cdot \bigtriangledown \mathbf{v} \ . \end{aligned} \tag{8.6}$$

Substituting $\mathbf{v} = \mathbf{v}_p + \mathbf{v}_d$ gives,

$$\frac{\partial \mathbf{v}_p}{\partial t} + \frac{\partial \mathbf{v}_d}{\partial t} + \mathbf{v}_p \cdot \bigtriangledown \mathbf{v}_p + \mathbf{v}_d \cdot \bigtriangledown \mathbf{v}_d + \mathbf{v}_p \cdot \bigtriangledown \mathbf{v}_d + \mathbf{v}_d \cdot \bigtriangledown \mathbf{v}_p = \frac{e\mathbf{E}_0}{m_e} sin(wt) \ . \tag{8.7}$$

This equation is reduced with $\mathbf{v}_p >> \mathbf{v}_d$ and when one takes the time average,

$$\langle \mathbf{v} \rangle = \frac{1}{T} \int_0^T \mathbf{v}(t) \cdot dt \ . \tag{8.8}$$

$$\cancel{\frac{\partial\langle \mathbf{v}_p\rangle}{\partial t}}+\frac{\partial\langle \mathbf{v}_d\rangle}{\partial t}+\langle \mathbf{v}_p\cdot\bigtriangledown \mathbf{v}_p\rangle+\cancel{\langle \mathbf{v}_d\cdot\bigtriangledown \mathbf{v}_d\rangle}+\cancel{\langle \mathbf{v}_p\cdot\bigtriangledown \mathbf{v}_d\rangle}+\cancel{\langle \mathbf{v}_d\cdot\bigtriangledown \mathbf{v}_p\rangle}=\frac{e\mathbf{E}_0}{m_e}\cancel{\langle sin(wt)\rangle} \quad (8.9)$$

$$\frac{\partial\langle \mathbf{v}_d\rangle}{\partial t}+\langle \mathbf{v}_p\cdot\bigtriangledown \mathbf{v}_p\rangle=0 \quad (8.10)$$

Inserting $\mathbf{v}_p$ from Equation 8.5 gives,

$$\frac{\partial\langle \mathbf{v}_d\rangle}{\partial t}=\frac{-e^2}{m^2w^2}\mathbf{E}_0\bigtriangledown \mathbf{E}_0\langle cos^2(wt)\rangle \quad (8.11)$$

Letting $\mathbf{E}_0\bigtriangledown \mathbf{E}_0=\frac{1}{2}\bigtriangledown \mathbf{E}_0^2$ and $\langle cos^2(wt)\rangle=\frac{1}{2}$ gives,

$$\mathbf{F}_d=m_e\frac{\partial\langle \mathbf{v}_d\rangle}{\partial t}=\frac{-e^2}{4mw^2}\bigtriangledown \mathbf{E}_0^2 \quad (8.12)$$

The drift force can be written in a more useful form using the equality $\mathbf{E}_0=\sqrt{\frac{2\mathbf{I}}{c\epsilon_0}}$ yielding,

$$\mathbf{F}_d=\frac{-e^2}{2mc\epsilon_0w^2}\bigtriangledown \mathbf{I}\ . \quad (8.13)$$

For a Gaussian spatial distribution, the intensity takes the form,

$$I=\frac{I_0}{w}e^{-r^2/w^2} \quad (8.14)$$

8.3 Appendix: Comparison of Long and Short Solenoids

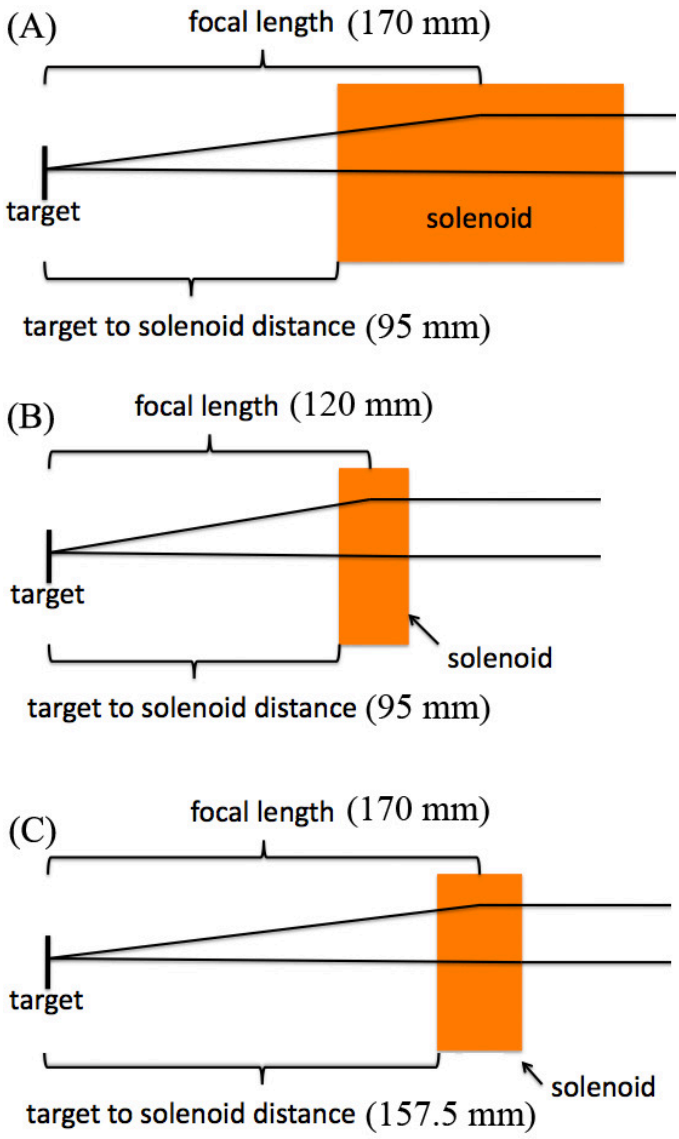

Figure 8.1: Set-up characteristics for the long and short solenoids.

In this appendix, we will review two solenoids (one long and one short) using General Particle Tracer. The long solenoid, labeled (A) throughout this section, is positioned with its first winding at 95 mm from the target foil, Figure 8.1. The short solenoid is positioned first at 95 mm from the target, labeled (B) here, and then an equivalent short solenoid is positionaned at 157.5 mm from the target, labeled (C). Each solenoid

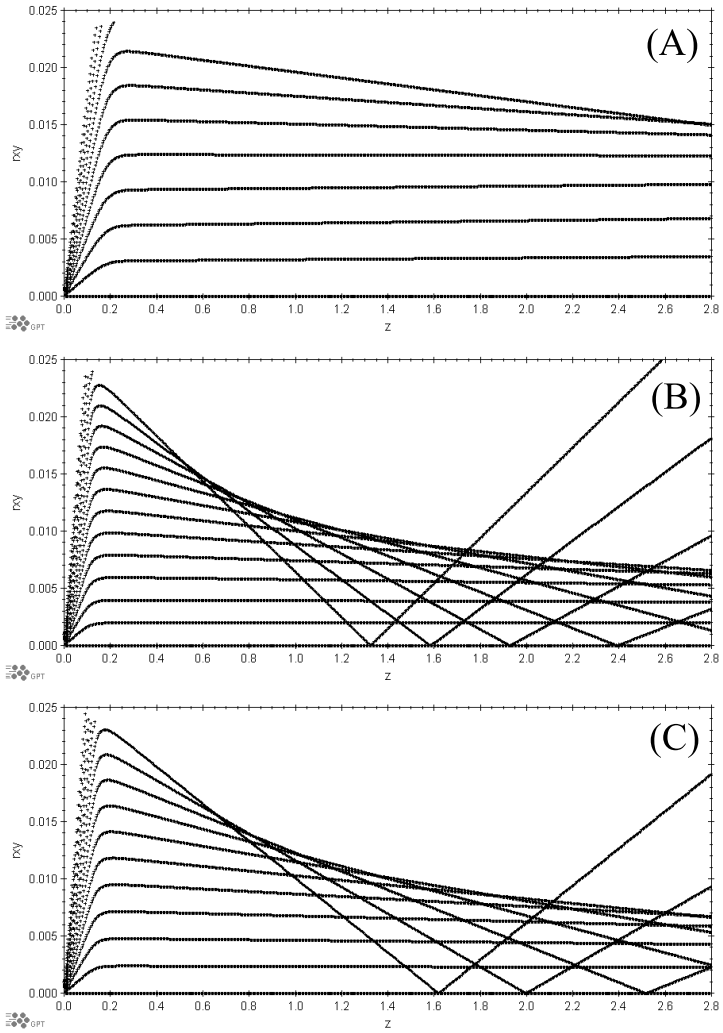

Figure 8.2: Three solenoids that all focus 11.0 MeV. (A) long solenoid, focal length f = 170 mm, target to solenoid distance is 95 mm; (B) short solenoid, focal length f = 120 mm, target to solenoid distance is 95 mm; (C) short solenoid, focal length f = 170 mm, target to solenoid distance is 157.5 mm. The protons possess divergence angles between 0 and 15 degrees in steps of 1 degree.

and set-up allow for a collimation of 11.0 MeV protons. Both (A) and (B) have the same target to winding distances, and both (A) and (C) have the same focal lengths. The characteristics of the solenoids are listed in Table 8.1.

The focal length of a solenoid follows the inverse of Equation 3.3 and is,

$$f = (\frac{2m_0\gamma\beta c}{q})^2 \frac{1}{\int_{-\infty}^{\infty} B_z^2 dz}. \tag{8.15}$$

	long (A)	short (B)	short (C)
number of layers	4	4	4
number of windings per layer	30	5	5
length	150 mm	25 mm	25 mm
target to solenoid distance	95 mm	95 mm	157.5 mm
collimated proton energy	11.0 MeV	11.0 MeV	11.0 MeV
focal length	170 mm	120 mm	170 mm
driving current	10.45 kA	60.3 kA	53.5 kA

Table 8.1: Characteristics of the long solenoid (A), short solenoid (B) and short solenoid (C).

Here, f is a measure from the target to the center of the solenoid and should not be confused with the target to winding distance. The larger focal lengths require smaller magnetic fields, but the increased distance from the target allows the protons to diverge farther off-axis, reducing the capture efficiency. This is seen in Figure 8.2 when we compare the 120 mm focal length of (B) with the 170 mm focal length of (C). As seen in Table 8.1, the current for (C) is 53.5 kA compared to (B) which is 60.0 kA, i.e. $\int_{-\infty}^{\infty} B_z^2 dz$ for (C) is less than that of (B). The proton traces in Figure 8.2 range from 0 degrees to 15 degrees in steps of 1 degree. By comparing the traces that emerge from the solenoid that are parallel to the longitudinal axis after the solenoid, we see (B) collimates protons within a 4 degree half angle while (C) collimates protons within a 3 degree half angle. This indicates that shorter focal lengths yield larger capture efficiencies, but require larger magnetic fields.

Figure 8.2 also illustrates how the chromaticity is affected by the target to solenoid distance, i.e. in (B), the chromatic spread is larger than in (C). Additionally, the traces in (B) and (C) are radially closer together than those in (A). This means that the protons are made parallel more quickly in the short solenoid. Figure 8.3, which compares the axial and radial magnetic fields for each solenoid, also suggests this. The field values are taken along z at r = 10 mm from the axis. The fields of the

short solenoid cover a smaller longitudinal range than the field of the long solenoid. For diverging protons, the radial distance that the protons travel off axis is related to the longitudinal distance they travel. Therefore, the fact that the short solenoid focuses over a shorter longitudinal distance than the long solenoid, the radial distance traveled is smaller for (B) and (C).

A final note, the increase in $\int_{-\infty}^{\infty} B_z^2 dz$ for the short solenoid increases the forces on the solenoid as discussed in Section 3.2.6.

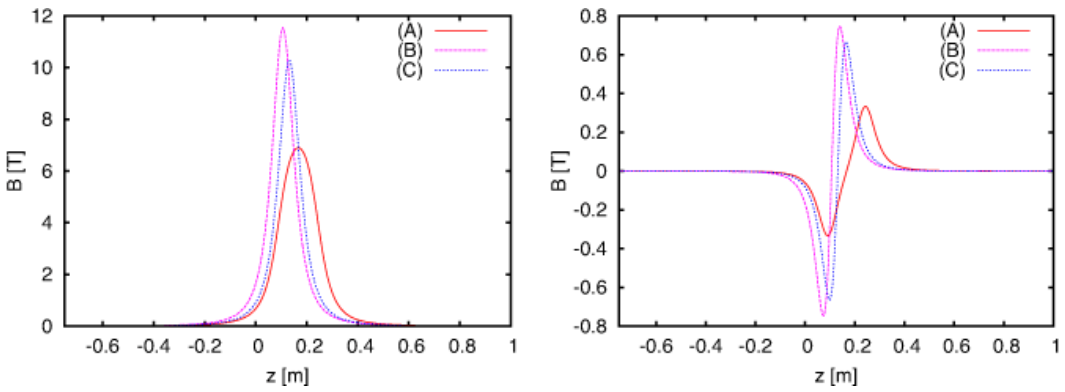

Figure 8.3: Comparison of the axial B_z and radial B_r magnetic fields (along z at a radial distance of 0.01 m off-axis) for the short and long solenoids. The solenoid and focal length characteristics for A, B, and C are given in Table 8.1

8.4 Appendix: AC Driven Fields: Magnetic Diffusion

Figure 8.4: Magnetic field diffusion into a conductor and the resulting induced current density as a function of skin depth. The magnetic field B is normalized to B_0, the field the surface boundary of the conductor, and the induced current density J is normalized to $J0$ which is the total induced current density found by integrating J from the surface to a depth $d = \infty$

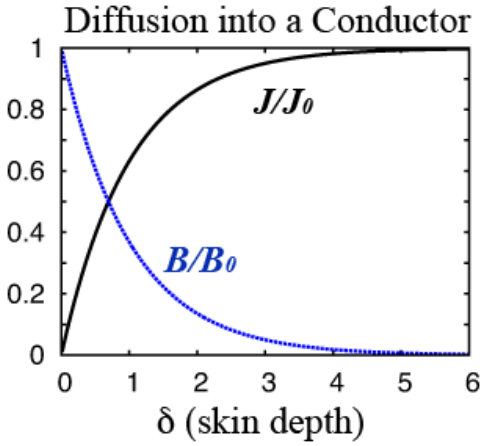

When interacting with a conductor, the changing magnetic field $\partial\mathbf{B}/\partial t = -\nabla \times \mathbf{E}$ induces an electromotive force (EMF) and eddy currents. The diffusion into the conductor is governed by the frequency ω of the field and the material's electrical conductivity σ and magnetic permeability μ. These induced currents oppose the driving magnetic field and, therefore, oppose the diffusion of the field into the conductor, Figure 8.4. The depth at which the field is reduced to $1/e = 1/2.718...$ of its value is termed the skin depth $\delta = \sqrt{1/\pi f_B \mu\sigma} = \sqrt{2/\mu\sigma\omega}$. The velocity of the diffusion into the conductor then follows $v_d = \delta\omega$. For copper, $\sigma = 5.96 \times 10^7$ [S/m], and with $\omega = 5000$ rad/s the skin depth $\delta = 2.3$ mm and the diffusion velocity $v_d = 11.6$ m/s.

If we consider alternating currents that propagate along a transmission line to a load, then we see that they do so initially as surface currents. Their velocities are relativistic and they incur multiple reflections in the transmission line while they diffuse inward. The total current $\mathbf{J}$ is the sum of the conduction current $\mathbf{J}_c = \sigma\mathbf{E}$ and the displacement current $\mathbf{J}_d = \varepsilon_r\varepsilon_0\partial\mathbf{E}/\partial t = i\omega\varepsilon_r\varepsilon_0\mathbf{E}$ (because of the sinusoidal driving current) where ε_r is the relative permittivity, $\varepsilon_0 = 8.85... \times 10^{-12}$ [F/m] is the

permittivity of vaccum and $i = \sqrt{-1}$. Then,

$$\nabla \times \mathbf{H} = (\sigma + i\omega\varepsilon_r\varepsilon_0)\mathbf{E} \tag{8.16}$$

where $\mathbf{H} = \mathbf{B}/\mu$. The displacement current is proportional to ω and, therefore, becomes larger as the frequency of the magnetic field increases. It can be seen that the displacement current will equal the conduction current for copper at the extremely large rate of $\omega = \sigma/\varepsilon_r\varepsilon_0 = 7 \times 10^{18}$ s^{-1}. For our purposes, the displacement currents become negligible and $\nabla \times \mathbf{H} = \sigma\mathbf{E}$, and the current remains localized to the surface. The electric field inside the conductor is then $\nabla \cdot \mathbf{E} = 0$.

To determine the diffusion equations,

$$\nabla \times \mathbf{H} = \mathbf{J} = \sigma\mathbf{E} \tag{8.17}$$

$$\nabla \cdot \mathbf{E} = 0 \tag{8.18}$$

$$\nabla \times \mathbf{E} = -\mu\frac{\partial \mathbf{H}}{\partial t} \tag{8.19}$$

$$\nabla \cdot \mathbf{H} = 0 \tag{8.20}$$

Substituting Equation **??** into the curl of Equation 8.17 yields,

$$\begin{aligned} \nabla \times \nabla \times \mathbf{H} &= \sigma(\nabla \times \mathbf{E}) \\ &= \mu\sigma\frac{\partial \mathbf{H}}{\partial t} \end{aligned} \tag{8.21}$$

and

$$\nabla \times \nabla \times \mathbf{B} = \mu\sigma\frac{\partial \mathbf{B}}{\partial t}$$

Similarly, substituting Equation 8.17 into the curl of Equation **??** yields,

$$\begin{aligned} \nabla \times \nabla \times \mathbf{E} &= -\mu \frac{\partial(\nabla \times \mathbf{H})}{\partial t} \\ &= -\mu\sigma \frac{\partial \mathbf{E}}{\partial t} \end{aligned} \tag{8.22}$$

and substituting $\mathbf{E} = \mathbf{J}/\sigma$ into this last equation gives

$$\nabla \times \nabla \times \mathbf{J} = -\mu\sigma \frac{\partial \mathbf{J}}{\partial t} \tag{8.23}$$

To get the magnetic diffusion equation, we can apply the vector identity,

$$\nabla \times \nabla \times \mathbf{A} = \nabla(\nabla \cdot \mathbf{A}) - \nabla^2 \mathbf{A} \tag{8.24}$$

and since $\nabla \cdot \mathbf{A} = 0$ for $\mathbf{A} = \mathbf{H}$, $\mathbf{B}$, $\mathbf{E}$ and $\mathbf{J}$, the diffusion equations become

$$\alpha \nabla^2 \mathbf{A} = \frac{\partial \mathbf{A}}{\partial t}$$

Here $\alpha = 1/\mu\sigma$ is the diffusivity which has the units of $[\mathrm{m}^2/\mathrm{s}]$. What this tells us is that the higher the diffusivity, the more rapidly a magnetic field will penetrate a conductor. Therefore, higher conductivities σ result in slower penetration speeds and shallower skin depths. This is because the higher conductivity allows for larger eddy currents to flow, which in turn oppose the penetrating magnetic field. As has been discussed in Section 3.2.5, induced currents can have a negative impact on the components used with a compact pulse power system, but induced currents in conducting eddy shields can also provide a shielding effect by matching the proper conductivity and material thickness to the frequency of the magnetic field.

8.5 Appendix: Von Mises Distribution

The von Mises distribution is also known as circular normal distribution, and it describes a continuous probability distribution on a circle. For an angle θ, the probability density function follows,

$$f(\theta|\mu,\kappa) = \frac{e^{\kappa \cdot cos(\theta-\mu)}}{2\pi I_0(\kappa)} \tag{8.25}$$

where

$$I(\kappa) = \sum_{m=0}^{\infty} \frac{1}{m!\Gamma(m+1)} \left(\frac{\kappa}{2}\right)^{2m} \tag{8.26}$$

is the modified Bessel function of order 0.

Since μ is the mean of the distribution, the distribution is centered around it with variance $1/\kappa$. Large values of κ increase the probability density near angle μ. For $\kappa = 0$ as is the case for generating the simulated proton beam in this work, $I_0(\kappa) = 1$ and the distribution is uniformly distributed throughout all angles θ.

Chapter 9

Publications and Presentations

LIST OF PUBLICATIONS

Submitted:

K. Zeil, M. Baumann, E. Beyreuther, **T. Burris-Mog**, T.E. Cowan, W. Enghardt, L. Karsch, S.D. Kraft, L. Laschinsky, J. Metzkes, D. Naumburger, M. Oppelt, C. Richter, R. Sauerbrey, M. Schrer, U. Schramm, J. Pawelk, Dose controlled irradiation of cancer cells with laser accelerated proton pulses Nature Physics (2012), submitted

Published in Refereed Journals:

L. Karscha, E. Beyreuther, **T. Burris-Mog**, S. Kraft, C. Richter, and K. Zeil, J. Pawelke, Dose rate dependence for different dosimeters and detectors: TLD, OSL, EBT films, and diamond detectors, Medical Physics 39 (5), (May 2012)

T. Kluge, S.A. Gaillard, K.A. Flippo, **T. Burris-Mog**, W. Enghardt, B. Gall, M. Geissel, A. Helm, S.D. Kraft, T. Lockard, J. Metzkes, D.T. Offermann, M. Schollmeier, U. Schramm, K. Zeil, M. Bussmann and T.E. Cowan, High proton ener-

gies from cone targets: electron acceleration mechanisms, New Journal of Physics 14 (2012) 023038

J.J. Melone, K.W.D. Ledingham, T. McCanny, **T. Burris-Mog**, U. Schramm, R. Grtzschel, S. Akhmadaliev, D. Hanf, K.M. Spohr, M. Bussmann, T. Cowan, S. M. Wiggins, M. R. Mitchell, In Situ Characterisation of Permanent Magnetic Quadrupoles for Focussing Proton Beams, Nucl. Instum. Meth. A 676, 126 (2011)

T. Burris-Mog, K. Harres, F. Nrnberg, S. Busold, M. Bussmann, O. Deppert, G. Hoffmeister, M. Joost, M. Sobiella, A. Tauschwitz, B. Zielbauer, V. Bagnoud, T. Herrmannsdoerfer, M. Roth, T.E. Cowan, Laser Accelerated Protons Captured and Transported by a Pulse Power Solenoid, Physical Review Special Topics - Accelerators and Beams, submitted (September 2011)

S. Buffechoux, J. Psikal, M. Nakatsutsumi, L. Romagnani, A. Andreev, K. Zeil, M. Amin, P. Antici, **T. Burris-Mog**, A. Compant-La-Fontaine, E. dHumieres, S. Fourmaux, S. Gaillard, F. Gobet, F. Hannachi, S. Kraft, A. Mancic, C. Plaisir, G. Sarri, M. Tarisien, T. Toncian, U. Schramm, M. Tampo, P. Audebert, O. Willi, T. E. Cowan, H. Ppin, V. Tikhonchuk, M. Borghesi, and J. Fuchs, Hot Electrons Transverse Refluxing in Ultraintense Laser-Solid Interactions, Physical Review Letters 105 015005 (2010)

Published in Non-Refereed Journals:

S. Busold, A. Almomani, V. Bagnoud, W. Barth, A. Blazevic, O. Boine-Frankenheim, C. Brabetz, **T. Burris-Mog**, T. Cowan, O. Deppert, M. Droba, P. Forck, A. Gopal, K. Harres, T. Herrmannsdoerfer, S. Herzer, G. Hoffmeister, I. Hoffmann, O. Jckel,

M. Joost, M. Kaluza, O. Kester, F. Nrnberg, A. Orzhekovskaya, U. Ratzinger, M. Roth, T. Sthlker, A. Tauschwitz, W. Vinzenz, S. Yaramishev, B. Zielbauer, Laser Proton Acceleration as a Compact Ion Source, Proceedings of 2011 Particle Accelerator Conference, New York (2011)

F. Nrnberg, D.P. Grote, K. Harres, **T. Burris-Mog**, S. Busold, O. Deppert, and M. Roth, Space-charge effects on laser-accelerated proton beams captured by a solenoidal magnetic field GSI Scientific Report (2010).

T. E. Cowan, U. Schramm, **T. Burris-Mog**, F. Fiedler, S. D. Kraft, K. Zeil, M. Baumann, M. Bussmann, W. Enghardt, K. Flippo, S. Gaillard, K. Harres, T. Herrmannsdoerfer, T. Kluge, F. Nrnberg, J. Pawelke, M. Roth, B. Schmidt, M. Sobiella, and R. Sauerbrey, Prospects For and Progress Towards Laser-Driven Particle Therapy Accelerators, American Institute of Physics Conference Series, volume 1299, pages 721726, (November 2010).

T. Kluge, S. A. Gaillard, M. Bussmann, K. A. Flippo, **T. Burris-Mog**, B. Gall, M. Geissel, S. D. Kraft, T. Lockard, J. Metzkes, D. T. Offermann, J. Rassuchine, M. Schollmeier, U. Schramm, Y. Sentoku, K. Zeil, and T. E. Cowan, Theoretical Understanding of Enhanced Proton Energies from Laser-Cone Interactions, AIP Conf. Proc. 1299, 715 (2010)

S. Buffechoux,M. Nakatsutsumi,A. Andreev,K. Zeil,**T. Burris-Mog**,G. Sarri,M. Amin,P. Antici,S. Fourmaux,S. Gaillard,A. Mancic,M. Tampo, H. Ppin,P. Audebert,O. Willi,T. Cowan,M. Borghesi,andJ. Fuchs, Enhanced laser-driven proton-acceleration from limited mass targets by high temporal contrast ultra-intense lasers, AIP Conf. Proc. Volume1228, pp. 279-286 (April 16, 2010)

LIST OF PRESENTATIONS

Updates on the HZDR Pulse Power Project, Laser Ion Generation, Handling and Transport Workshop, GSI Darmstadt, Germany (July 2011)

Simulations of Pulsed Ion Optics and Beam Transport at FZD, Test Stand to Capture and Transport Laser-Accelerated Proton Beams Workshop, GSI Darmstadt, Germany (August 2010)

Capture and Collimation of Laser Accelerated Protons using a Scalable Pulse-Powered Solenoid, 4th ExtreMe Matter Institute (EMMI) workshop on Plasma Physics with Intense Heavy Ion and Laser Beams, Darmstadt, Germany (May 2011)

Results from the Pulsed-Solenoid Proton-Collimation Experiment at GSI, FZD Radiation Physics Work in Progress Seminar, Dresden, Germany, (January 2010)

Laser Accelerated Protons and Their Possible Future in Oncology, Hadron Therapy Workshop, Erice, Italy (April 2009)

Progress of Laser-Driven-Proton Beam Transport for DRACO Cell Irradiation Experiments,FZD Radiation Physics Work in Progress Seminar, Dresden, Germany, (March 2009)

Bibliography

[1] T. Burris-Mog, K. Harres, F. Nürnberg, S. Busold, M. Bussmann, O. Deppert, G. Hoffmeister, M. Joost, M. Sobiella, A. Tauschwitz, B. Zielbauer, V. Bagnoud, T. Herrmannsdoerfer, M. Roth, and T. E. Cowan. Laser accelerated protons captured and transported by a pulse power solenoid. *Phys. Rev. ST Accel. Beams*, 14:121301, Dec 2011.

[2] S.V Bulanov, T.Zh Esirkepov, V.S Khoroshkov, A.V Kuznetsov, and F Pegoraro. Oncological hadrontherapy with laser ion accelerators. *Physics Letters A*, 299(2-3):240 – 247, 2002.

[3] KWD Ledingham, W. Galster, and R. Sauerbrey. Laser-driven proton oncology a unique new cancer therapy? *British Journal of Radiology*, 80(959):855, 2007.

[4] M. Borghesi, T. Toncian, J. Fuchs, C. A. Cecchetti, L. Romagnani, S. Kar, K. Quinn, B. Ramakrishna, P. A. Wilson, P. Antici, P. Audebert, E. Brambrink, A. Pipahl, R. Jung, M. Amin, O. Willi, R. J. Clarke, M. Notley, P. Mora, T. Grismayer, E. D'Humières, and Y. Sentoku. Laser-driven proton acceleration and applications: Recent results. *European Physical Journal Special Topics*, 175:105–110, August 2009.

[5] T. E. Cowan, U. Schramm, T. Burris-Mog, F. Fiedler, S. D. Kraft, K. Zeil,

M. Baumann, M. Bussmann, W. Enghardt, K. Flippo, S. Gaillard, K. Harres, T. Herrmannsdoerfer, T. Kluge, F. Nürnberg, J. Pawelke, M. Roth, B. Schmidt, M. Sobiella, and R. Sauerbrey. Prospects For and Progress Towards Laser-Driven Particle Therapy Accelerators. In S. H. Gold & G. S. Nusinovich, editor, *American Institute of Physics Conference Series*, volume 1299 of *American Institute of Physics Conference Series*, pages 721–726, November 2010.

[6] Ingo Hofmann, Jürgen Meyer-ter Vehn, Xueqing Yan, Anna Orzhekhovskaya, and Stepan Yaramyshev. Collection and focusing of laser accelerated ion beams for therapy applications. *Phys. Rev. ST Accel. Beams*, 14:031304, Mar 2011.

[7] M. Nishiuchi, I. Daito, M. Ikegami, H. Daido, M. Mori, S. Orimo, K. Ogura, A. Sagisaka, A. Yogo, A. S. Pirozhkov, H. Sugiyama, H. Kiriyama, H. Okada, S. Kanazawa, S. Kondo, T. Shimomura, M. Tanoue, Y. Nakai, H. Sasao, D. Wakai, H. Sakaki, P. Bolton, I. W. Choi, J. H. Sung, J. Lee, Y. Oishi, T. Fujii, K. Nemoto, H. Souda, A. Noda, Y. Iseki, and T. Yoshiyuki. Focusing and spectral enhancement of a repetition-rated, laser-driven, divergent multi-mev proton beam using permanent quadrupole magnets. *Applied Physics Letters*, 94(6):061107, 2009.

[8] M. Nishiuchi, H. Sakaki, T. Hori, P. R. Bolton, K. Ogura, A. Sagisaka, A. Yogo, M. Mori, S. Orimo, A. S. Pirozhkov, I. Daito, H. Kiriyama, H. Okada, S. Kanazawa, S. Kondo, T. Shimomura, M. Tanoue, Y. Nakai, H. Sasao, D. Wakai, H. Daido, K. Kondo, H. Souda, H. Tongu, A. Noda, Y. Iseki, T. Nagafuchi, K. Maeda, K. Hanawa, T. Yoshiyuki, and T. Shirai. Measured and simulated transport of 1.9 mev laser-accelerated proton bunches through an integrated test beam line at 1 hz. *Phys. Rev. ST Accel. Beams*, 13(7):071304, Jul

2010.

[9] E. Fourkal, B. Shahine, M. Ding, JS Li, T. Tajima, and C.M. Ma. Particle in cell simulation of laser-accelerated proton beams for radiation therapy. *Medical physics*, 29:2788, 2002.

[10] C. Ma, I. Veltchev, E. Fourkal, J. Li, W. Luo, J. Fan, T. Lin, and A. Pollack. Development of a laser-driven proton accelerator for cancer therapy. *Laser Physics*, 16:639–646, 2006. 10.1134/S1054660X06040165.

[11] The Royal College of Radiologists (2003), BFCO(03)3, Equipment, Workload and Staffing for Radiotherapy in the UK 19972002).

[12] Pioneer in x-ray therapy. *Science*, 125(3236):pp. 18–19, 1957.

[13] M. Goitein and M. Jermann. The relative costs of proton and x-ray radiation therapy. *Clinical Oncology*, 15(1):S37 – S50, 2003.

[14] D. Clery. The Next Big Beam? *Science*, 327:142–143, January 2010.

[15] V. Bagnoud, B. Aurand, A. Blazevic, S. Borneis, C. Bruske, B. Ecker, U. Eisenbarth, J. Fils, A. Frank, E. Gaul, et al. Commissioning and early experiments of the phelix facility. *Applied Physics B: Lasers and Optics*, pages 1–14, 2010.

[16] R. A. Snavely, M. H. Key, S. P. Hatchett, T. E. Cowan, M. Roth, T. W. Phillips, M. A. Stoyer, E. A. Henry, T. C. Sangster, M. S. Singh, S. C. Wilks, A. MacKinnon, A. Offenberger, D. M. Pennington, K. Yasuike, A. B. Langdon, B. F. Lasinski, J. Johnson, M. D. Perry, and E. M. Campbell. Intense high-energy proton beams from petawatt-laser irradiation of solids. *Phys. Rev. Lett.*, 85:2945, 2000.

[17] M. Passoni, L. Bertagna, and A. Zani. Target normal sheath acceleration: theory, comparison with experiments and future perspectives. *New Journal of Physics*, 12, April 2010.

[18] T.E. Cowan, J. Fuchs, H. Ruhl, A. Kemp, P. Audebert, M. Roth, R. Stephens, I. Barton, A. Blazevic, E. Brambrink, J. Cobble, J. Fernandez, J.-C. Gauthier, M. Geissel, M. Hegelich, J. Kaae, S. Karsch, G.P. Le Sage, S. Letzring, M. Manclossi, S. Meyroneinc, A. Newkirk, H. Pepin, and N. Renard-LeGalloudec. Ultralow emittance, multi-mev proton beams from a laser virtual-cathode plasma accelerator. *Physical Review Letters*, 92(20):204801–1, 2004.

[19] Y. Sentoku, T.E. Cowan, A. Kemp, and H Ruhl. High energy proton acceleration in interaction of short laser pulse with dense plasma target. *Physics of Plasmas*, 10:pp. 2009–2015, 2003.

[20] M. Roth, T. E. Cowan, M. H. Key, S. P. Hatchett, C. Brown, W. Fountain, J. Johnson, D. M. Pennington, R. A. Snavely, S. C. Wilks, K. Yasuike, H. Ruhl, F. Pegoraro, S. V. Bulanov, E. M. Campbell, M. D. Perry, and H. Powell. Fast ignition by intense laser-accelerated proton beams. *Phys. Rev. Lett.*, 86:436–439, Jan 2001.

[21] P. Antici, M. Fazi, A. Lombardi, M. Migliorati, L. Palumbo, P. Audebert, and J. Fuchs. Numerical study of a linear accelerator using laser-generated proton beams as a source. *Journal of Applied Physics*, 104(12):124901, December 2008.

[22] E. Brambrink, J. Schreiber, T. Schlegel, P. Audebert, J. Cobble, J. Fuchs, M. Hegelich, and M. Roth. Transverse characteristics of short-pulse laser-produced ion beams: A study of the acceleration dynamics. *Phys. Rev. Lett.*, 96:154801, Apr 2006.

[23] K. W. D. Ledingham, P. McKenna, and R. P. Singhal. Applications for Nuclear Phenomena Generated by Ultra-Intense Lasers. *Science*, 300:1107–1111, May 2003.

[24] PK Patel, AJ Mackinnon, MH Key, TE Cowan, ME Foord, M. Allen, DF Price, H. Ruhl, PT Springer, and R. Stephens. Isochoric heating of solid-density matter with an ultrafast proton beam. *Physical Review Letters*, 91(12):125004, 2003.

[25] M. Roth, T. E. Cowan, M. H. Key, S. P. Hatchett, C. Brown, W. Fountain, J. Johnson, D. M. Pennington, R. A. Snavely, S. C. Wilks, K. Yasuike, H. Ruhl, F. Pegoraro, S. V. Bulanov, E. M. Campbell, M. D. Perry, and H. Powell. Fast ignition by intense laser-accelerated proton beams. *Phys. Rev. Lett.*, 86:436–439, Jan 2001.

[26] J. Denavit. Absorption of high-intensity subpicosecond lasers on solid density targets. *Physical Review Letters*, 69:3052–3055, November 1992.

[27] A. Zhidkov, M. Uesaka, A. Sasaki, and H. Daido. Ion Acceleration in a Solitary Wave by an Intense Picosecond Laser Pulse. *Physical Review Letters*, 89(21):215002–+, November 2002.

[28] A. Pukhov and J. Meyer-Ter-Vehn. Laser Hole Boring into Overdense Plasma and Relativistic Electron Currents for Fast Ignition of ICF Targets. *Physical Review Letters*, 79:2686–2689, October 1997.

[29] A. Macchi, F. Cattani, T. V. Liseykina, and F. Cornolti. Laser Acceleration of Ion Bunches at the Front Surface of Overdense Plasmas. *Physical Review Letters*, 94(16):165003–+, April 2005.

[30] A. P. L. Robinson, P. Gibbon, M. Zepf, S. Kar, R. G. Evans, and C. Bellei. Relativistically correct hole-boring and ion acceleration by circularly polarized laser pulses. *Plasma Physics and Controlled Fusion*, 51(2):024004–+, February 2009.

[31] G. Marx. Interstellar Vehicle Propelled By Terrestrial Laser Beam. *Nature*, 211:22–23, July 1966.

[32] T. Esirkepov, M. Borghesi, S. V. Bulanov, G. Mourou, and T. Tajima. Highly efficient relativistic-ion generation in the laser-piston regime. *Phys. Rev. Lett.*, 92:175003, Apr 2004.

[33] A. P. L. Robinson, M. Zepf, S. Kar, R. G. Evans, and C. Bellei. Radiation pressure acceleration of thin foils with circularly polarized laser pulses. *New Journal of Physics*, 10(1):013021–+, January 2008.

[34] A. Henig, S. Steinke, M. Schnürer, T. Sokollik, R. Hörlein, D. Kiefer, D. Jung, J. Schreiber, B. M. Hegelich, X. Q. Yan, J. Meyer-ter Vehn, T. Tajima, P. V. Nickles, W. Sandner, and D. Habs. Radiation-pressure acceleration of ion beams driven by circularly polarized laser pulses. *Phys. Rev. Lett.*, 103:245003, Dec 2009.

[35] B. M. Hegelich, B. J. Albright, J. Cobble, K. Flippo, S. Letzring, M. Paffett, H. Ruhl, J. Schreiber, R. K. Schulze, and J. C. Fernández. Laser acceleration of quasi-monoenergetic MeV ion beams. *Nature*, 439:441–444, January 2006.

[36] L. Yin, B. J. Albright, B. M. Hegelich, K. J. Bowers, K. A. Flippo, T. J. T. Kwan, and J. C. Fernández. Monoenergetic and GeV ion acceleration from the laser breakout afterburner using ultrathin targets. *Physics of Plasmas*,

14(5):056706–+, May 2007.

[37] L. Yin, B. J. Albright, K. J. Bowers, D. Jung, J. C. Fernández, and B. M. Hegelich. Three-dimensional dynamics of breakout afterburner ion acceleration using high-contrast short-pulse laser and nanoscale targets. *Phys. Rev. Lett.*, 107:045003, Jul 2011.

[38] S. A. Gaillard, T. Kluge, K. A. Flippo, M. Bussmann, B. Gall, T. Lockard, M. Geissel, D. T. Offermann, M. Schollmeier, Y. Sentoku, and T. E. Cowan. Increased laser-accelerated proton energies via direct laser-light-pressure acceleration of electrons in microcone targets. *Physics of Plasmas*, 18(5):056710–+, May 2011.

[39] S. A. Gaillard, K. A. Flippo, M. E. Lowenstern, J. E. Mucino, J. M. Rassuchine, D. C. Gautier, J. Workman, and T. E. Cowan. Proton acceleration from ultrahigh-intensity short-pulse laser-matter interactions with Cu microcone targets at an intrinsic ˜10^{-8} contrast. *Journal of Physics Conference Series*, 244(2):022034–+, August 2010.

[40] N. B. Baranova, H. R. Reiss, and B. Y. Zel'dovich. Multiphoton and tunnel ionization by an optical field with polar asymmetry. *Physical Review A*, 48:1497–1505, August 1993.

[41] Gibbon, P. Short pulse laser interactions with matter: an introduction, Imperial College Press (2005).

[42] J. Denavit. Collisionless plasma expansion into a vacuum. *Physics of Fluids*, 22, 1979.

[43] E. L. Clark, K. Krushelnick, M. Zepf, F. N. Beg, M. Tatarakis, A. Machacek,

M. I. K. Santala, I. Watts, P. A. Norreys, and A. E. Dangor. Energetic heavy-ion and proton generation from ultraintense laser-plasma interactions with solids. *Phys. Rev. Lett.*, 85:1654–1657, Aug 2000.

[44] S. C. Wilks, A. B. Langdon, T. E. Cowan, M. Roth, M. Singh, S. Hatchett, M. H. Key, D. Pennington, A. MacKinnon, and R. A. Snavely. Energetic proton generation in ultra-intense laser-solid interactions. *Physics of Plasmas*, 8:542–549, February 2001.

[45] L. Robson, P.T. Simpson, R. J. Clarke, K.W.D. Ledingham, F. Lindau, Lundh O., T. McCanny, P. Mora, D. Neely, C.-G. Wahlström, M. Zepf, and P. McKenna. Scaling of proton acceleration driven by petawatt-laser-plasma interactions. *Nature Physics*, 3:58, 2006.

[46] S. C. Wilks, W. L. Kruer, M. Tabak, and A. B. Langdon. Absorption of ultra-intense laser pulses. *Physical Review Letters*, 69:1383–1386, August 1992.

[47] P. Mora. Plasma expansion into a vacuum. *Phys. Rev. Lett.*, 90(18):185002, 2003.

[48] F. Nürnberg, M. Schollmeier, E. Brambrink, A. Blazevic, DC Carroll, K. Flippo, DC Gautier, M. Geißel, K. Harres, BM Hegelich, et al. Radiochromic film imaging spectroscopy of laser-accelerated proton beams. *Review of scientific instruments*, 80:033301, 2009.

[49] J. Fuchs, T.E. Cowan, P. Audebert, H. Ruhl, L. Gremillet, A. Kemp, M. Allen, A. Blazevic, J.C. Gauthier, M. Geissel, M. Hegelich, S. Karsch, P. Parks, M. Roth, Y. Sentoku, R. Stephens, and E.M. Campbell. Spatial uniformity of laser-accelerated ultrahigh-current mev electron propagation in metals and

insulators. *Physical Review Letters*, 91(25):255002–1, 2003.

[50] Work in Progress, M. Roth, O. Deppert (GSI Helmholtz-Zentrum für Schwerionenforschung GmbH).

[51] S. N. Chen, E. d'Humières, E. Lefebvre, L. Romagnani, T. Toncian, P. Antici, P. Audebert, E. Brambrink, C. A. Cecchetti, T. Kudyakov, A. Pipahl, Y. Sentoku, M. Borghesi, O. Willi, and J. Fuchs. Focusing dynamics of high-energy density, laser-driven ion beams. *Phys. Rev. Lett.*, 108:055001, Jan 2012.

[52] Work in Progress, T.E. Cowan (Helmholtz-Zentrum Dresden-Rossendorf), V. Bagnoud, C. Brabetz (GSI Helmholtz-Zentrum für Schwerionenforschung GmbH).

[53] T. Toncian, M. Borghesi, J. Fuchs, E. d'Humières, P. Antici, P. Audebert, E. Brambrink, C. A. Cecchetti, A. Pipahl, L. Romagnani, and O. Willi. Ultrafast Laser-Driven Microlens to Focus and Energy-Select Mega-Electron Volt Protons. *Science*, 312:410–413, April 2006.

[54] P. Antici, M. Fazi, A. Lombardi, M. Migliorati, L. Palumbo, P. Audebert, and J. Fuchs. Postacceleration of laser-generated high-energy protons through conventional accelerator linacs. *Plasma Science, IEEE Transactions on*, 36(4):1843 –1846, aug. 2008.

[55] M. Schollmeier, S. Becker, M. Geiel, K.A. Flippo, A. Blazevic, S.A. Gaillard, D.C. Gautier, F. Gruner, K. Harres, M. Kimmel, F. Nurnberg, P. Rambo, U. Schramm, J. Schreiber, J. Schutrumpf, J. Schwarz, N.A. Tahir, B. Atherton, D. Habs, B.M. Hegelich, and M. Roth. Controlled transport and focusing of laser-accelerated protons with miniature magnetic devices. *Physical Review*

Letters, 101:055004–1, 2008.

[56] H. Sakaki, M. Nishiuchi, T. Hori, P.R. Bolton, M. Tampo, A. Yogo, K. Kondo, S. Kawanishi, H. Iwase, and K. Niita. Simulation of laser-accelerated proton focusing and diagnosis with a permanent magnet quadrupole triplet. *Plasma and Fusion Research*, 5(0):9–9, 2010.

[57] M. Roth, I. Alber, V. Bagnoud, CRD Brown, R. Clarke, H. Daido, J. Fernandez, K. Flippo, S. Gaillard, C. Gauthier, et al. Proton acceleration experiments and warm dense matter research using high power lasers. *Plasma Physics and Controlled Fusion*, 51:124039, 2009.

[58] K. Harres, I. Alber, A. Tauschwitz, V. Bagnoud, H. Daido, M. Günther, F. Nürnberg, A. Otten, M. Schollmeier, J. Schütrumpf, Tampo M., and Roth M. Beam collimation and transport of quasineutral laser-accelerated protons by a solenoid field. *Physics of Plasmas*, 17:023107, 2010.

[59] D. Neely, P. Foster, A. Robinson, F. Lindau, O. Lundh, A. Persson, C.-G. Wahlström, and P. McKenna. Enhanced proton beams from ultrathin targets driven by high contrast laser pulses. *Applied Physics Letters*, 89(2):021502–+, July 2006.

[60] T. Ceccotti, A. Lévy, H. Popescu, F. Réau, P. D'Oliveira, P. Monot, J. P. Geindre, E. Lefebvre, and Ph. Martin. Proton acceleration with high-intensity ultrahigh-contrast laser pulses. *Phys. Rev. Lett.*, 99:185002, Oct 2007.

[61] A. Henig, D. Kiefer, K. Markey, D. C. Gautier, K. A. Flippo, S. Letzring, R. P. Johnson, T. Shimada, L. Yin, B. J. Albright, K. J. Bowers, J. C. Fernández, S. G. Rykovanov, H.-C. Wu, M. Zepf, D. Jung, V. Kh. Liechtenstein,

J. Schreiber, D. Habs, and B. M. Hegelich. Enhanced laser-driven ion acceleration in the relativistic transparency regime. *Phys. Rev. Lett.*, 103:045002, Jul 2009.

[62] T. Kluge, M. Bussmann, S.A. Gaillard, K.A. Flippo, D.C. Gautier, B. Gall, T. Lockard, M.E. Lowenstern, J.E. Mucino, Y. Sentoku, Low-Divergent, Energetic Electron Beams from Ultra-Thin Foils. AIP Conference Proceedings 1209 (2010) p. 51.

[63] O. Ishihara, A. Hirose, and A. B. Langdon. Nonlinear saturation of the Buneman instability. *Physical Review Letters*, 44:1404–1407, May 1980.

[64] Helmut Wiedemann. *Particle Accelerator Physics I and II.* Springer-Verlag Berlin and Heidelberg GmbH & Co. K, 2nd ed edition, 1999.

[65] Press release published by Helmholtz-Zentrum Dresden-Rossendorf on June 28, 2011, www.hzdr.de.

[66] Mag lab report, volume 18, issue 3, magnetic lab pulsed field facility, los alamos national laborator, www.magnet.fsu.edu.

[67] C. H. Mielke and B. M. Novac. Experimental and Numerical Studies of Megagauss Magnetic-Field Generation at LANL-NHMFL. *IEEE Transactions on Plasma Science*, 38:1739–1749, August 2010.

[68] Intimate discussions with Thomas Kluge.

[69] R.L. Daiglish and J.C. Kelly. The Application of Busch's Theorem to magnetic lenses for beam focusing. *Physical Letters*, 53(3), 1975.

[70] Pulsar Physics, Burghstraat 47, 5614 BC Eindhoven, The Netherlands

(www.pulsar.nl).

[71] COMSOL Multiphysics Finite Element Analysis Software (formerly FEMLAB), http://www.comsol.com/.

[72] A. Bayramian, P. Armstrong, E. Ault, R. Beach, C. Bibeau, J. Caird, R. Campbell, B. Chai, J. Dawson, C. Ebbers, A. Erlandson, Y. Fei, B. Freitas, R. Kent, Z. Liao, T. Ladran, J. Menapace, B. Molander, S. Payne, N. Peterson, M. Randles, K. Schaffers, S. Sutton, J. Tassano, S. Telford, and E. Utterback, The Mercury Project: A high average power, gas-cooled laser for inertial fusion energy development. Fusion Science and Technology, Vol. 52, (2007).

[73] U. Schramm, K. Zeil, C. Richter, E. Beyreuther, M. Bussmann, T. E. Cowan, W. Enghardt, L. Karsch, T. Kluge, S. Kraft, L. Laschinsky, J. Metzkes, D. Naumburger, J. Pawelke, and R. Sauerbrey. Ultrashort Pulse Laser Accelerated Proton Beams for First Radiobiological Applications. In *American Institute of Physics Conference Series*, volume 1299 of *American Institute of Physics Conference Series*, pages 731–736, November 2010.

[74] F. Herlach. Pulsed magnets. *Reports on Progress in Physics*, 62:859–920, June 1999.

[75] Nicholas M. Jordan, Y. Y. Lau, David M. French, R. M. Gilgenbach, and P. Pengvanich. Electric field and electron orbits near a triple point. *Journal of Applied Physics*, 102(3):033301 –033301–10, aug 2007.

[76] L. Cranberg. The Initiation of Electrical Breakdown in Vacuum. *Journal of Applied Physics*, 23:518–522, April 1952.

[77] A. Boulloud and C. Texier. On the observation of microparticles flying through

an electrically stressed vacuum gap. *Journal of Physics D Applied Physics*, 11:L37–L38, February 1978.

[78] H.C. Miller. Flashover of insulators in vacuum: review of the phenomena and techniques to improved holdoff voltage . *IEEE Transactions on Electrical Insulation*, 28:512–527, August 1993.

[79] S. Coulombe and J.-L. Meunier. A comparison of electron-emission equations used in arc - cathode interaction calculations. *Journal of Physics D Applied Physics*, 30:2905–2910, October 1997.

[80] J. G. Trump and R. J. van de Graaff. The Insulation of High Voltages in Vacuum. *Journal of Applied Physics*, 18:327–332, March 1947.

[81] R. Hackam and L. Altcheh. ac (50 Hz) and dc electrical breakdown of vacuum gaps and with variation of air pressure in the range 10-9-10-2 Torr using OFHC copper, nickel, aluminum, and niobium parallel planar electrodes. *Journal of Applied Physics*, 46:627–636, February 1975.

[82] R. Hackam and G. R. G. Raju. Electrical breakdown of a point-plane gap in high vacuum and with variation of pressure in the range 10-7-10-2 Torr of air, nitrogen, helium, sulphur hexafluoride, and argon. *Journal of Applied Physics*, 45:4784–4794, November 1974.

[83] G.T. Alisoy, H.Z. Alisoy, and M. Koseoglu. Calculation of electrical field of spherical and cylindrical gas voids in dielectrics by taking surface conductivity into consideration. *COMPEL: Int J for Computation and Maths. in Electrical and Electronic Eng.*, 24(4):1152–1163, 2005.

[84] Proceedings of the Conference on Computer Codes and the Linear Accelerator

Community Los Alamos National Laboratory, January 22-25, 1990.

[85] Numerical Recipes In C: The Art of Scientific Computing (ISBN 0-521-43108-5), Cambridge University Press.

[86] General Particle Tracer Manual, Section 1.7 - Equations of Motion, Pulsar Physics, Burghstraat 47, 5614 BC Eindhoven, The Netherlands (www.pulsar.nl).

[87] M. Abramowitz and I. A. Stegun. *Handbook of Mathematical Functions*. National Bureau of Standards, 1964. 0-486-61272-4.

[88] Laser-Accelerated Proton Beams as a New Particle Source, Ph.D. Thesis by Frank Nürnberg, Technische UniversitÄt Darmstadt, November 2010.

[89] W. Joho, Representation of Beam Ellipses for Transport Calculations, Swiss Institute for Nuclear Research, SIN Report TM-11-14, August 5 (1980).

[90] Energy Loss In RadioChromic Film Matlab Script, written by M. Schollmeier, F. Nürnberg, K.A. Flippo.

[91] M. Nishiuchi, H. Sakaki, T. Hori, P.R. Bolton, K. Ogura, A. Sagisaka, A. Yogo, M. Mori, S. Orimo, A.S. Pirozhkov, I. Daito, H. Kiriyama, H. Okada, S. Kanazawa, S. Kondo, T. Shimomura, M. Tanoue, Y. Nakai, H. Sasao, D. Wakai, H. Daido, K. Kondo, H. Souda, H. Tongu, A. Noda, Kyoto, Y. Iseki, T. Nagafuchi, K. Maeda, K. Hanawa, T. Yoshiyuki, T. Shirai, Laser-driven proton acceleration for medical application, Proceedings of IPAC10, Kyoto, Japan (2010).

[92] Software: The Stopping and Range of Ions in Matter (2011 version), J. F. Ziegler, M.D. Ziegler, J.P. Biersack, www.srim.org.

[93] Space-charge effects on laser-accelerated proton beams captured by a solenoidal magnetic field F. Nürnberg, D.P. Grote, K. Harres, T. Burris, S. Busold, O. Deppert, and M. Roth, GSI Scientific Report (2010).

[94] F. Nürnberg, A. Friedman, DP Grote, K. Harres, BG Logan, M. Schollmeier, and M. Roth. Warp simulations for capture and control of laser-accelerated proton beams. In *Journal of Physics: Conference Series*, volume 244, page 022052. IOP Publishing, 2010.

[95] Laser Ion Generation, Handling and Transport (LIGHT), GSI Scientific Report (2010).

[96] M. Pavlovic, E. Griesmayer, and T. Schreiner. A study of dispersion effects in transport of ion–therapy beams. *Journal of ELECTRICAL ENGINEERING*, 58(1):33–38, 2007.

[97] Y. Jongen, S. Laycock, M. Abs, J.-C. Amelia, W. Beeckman, W. Kleeven, M. Ladeuze, G. Lannoye, D. Leyman, V. Poreye, D. Vandeplassche, S. Zaremba, T. Hurn, L. Nissley, E. Hubbard, M. Heiberger, M. Tabor, C. Silke, T. Tachikawa, and et al. The proton therapy system for the NPTC: Equipment description and progress report. *Nuclear Instruments and Methods in Physics Research B*, 113:522–525, June 1996.

[98] S. G. Peggs, T. Satogata, and J. Flanz. A Survey of Hadron Therapy Accelerator Technologies. In *22nd Particle Accelerator Conference (PAC 07)*, page 115, 2007.

[99] Y. Yonemura and et al. Development of FFAG Accelerator at KEK. In *21st Particle Accelerator Conference (PAC 05)*, page 1943, 2005.

[100] Y.-J. Chen and A. C. Paul. Compact proton accelerator for cancer therapy. In *22nd Particle Accelerator Conference (PAC 07)*, page 1787, 2007.

[101] D. Trbojevic, R. Gupta, B. Parker, E. Keil, A.M. Sessler, A Dramatically Reduced Size in the Gantry Design for the Proton-Carbon Therapy, Proceedings of EPAC 2006, Edinburgh, Scotland.

[102] W-M Yao et al 2006 J. Phys. G: Nucl. Part. Phys. 33, 1.